Deuteron Photodisintegration at Intermediate Energies

Peter Anthony Wallace

Presented as a Thesis for the Degree of Doctor of Philosophy

Department of Physics and Astronomy,

University of Glasgow.

March 1989.

I guess I'm just an old mad scientist at bottom. Give me an underground laboratory, half a dozen atomsmashers, and a beautiful girl in a diaphanous veil waiting to be turned into a chimpanzee, and I care not who writes the nation's laws.

S.J.Perelman

Abstract

This thesis describes an experiment whose aim was to measure the angular differential cross-section $d^2\sigma/d\Omega_p dE_\gamma$ for the two-body photodisintegration of the deuteron $D(\gamma,p)n$ at photon energies in the region of 140 MeV . The experiment was performed using the Glasgow tagged photon spectrometer which was installed at the Mainz Institut für Kernphysik to take advantage of the high quality d.c. electron beam provided by the racetrack microtron MAMI-A. The experimental work and subsequent data analysis took place in the period from March 1986 to December 1988.

The motivation for the project was provided by the recent renewal of theoretical interest in the deuteron photodisintegration reaction which has lead to a call for new and more reliable data on the process. The significance of the reaction lies in its use as a test case for the application of modern models of the $N-N$ interaction. Such models seek to describe the nuclear force in terms of the underlying hadronic dynamics of the nucleon-meson system as opposed to the essentially phenomenological parameterisations which have been used previously. Photons, both real and virtual, provide the ideal tool for such studies since the electromagnetic interaction is the best understood of all the elementary processes.

The experiment was performed with a 0.45 g cm^{-2} liquid deuterium target cell placed in a tagged photon beam with a total intensity of $10^7 s^{-1}$ in the range $E_\gamma = 133 - 158$MeV . Protons were detected in a large solid angle (0.9 steradian) position sensitive plastic scintillator telescope which had an energy resolution of 5% and an angular resolution of 3°. Measurement of the proton energy and angle together with knowledge of photon energy overdefined

the reaction kinematics thus facilitating a very clean rejection of background events. Reliable normalisation was assisted by the tagging technique which determined the photon flux to $\pm$ 1%.

A complete Monte Carlo simulation of the experiment was developed in order to evaluate the systematic corrections to the data. Included in the simulation are effects due to the beam-target geometry, energy losses of the protons in the target, energy deposition in the detector, light production non-linearities and nuclear interactions of the protons in the CH scintillator medium, and also variations in the light collection efficiency throughout the scintillator blocks. The monte carlo simulation produces an efficiency correction factor specific to each data point, as well as providing global normalisation factors to account for the tagging efficiency and the combination of beam and target geometries.

The data is presented in the form of two angular distributions corresponding to mean photon energies of 140 and 150 MeV . The total systematic error is estimated to be not greater than 6 %. The results are found to be in good general agreement with other recent experiments but it is observed that none of the available theoretical calculations can give a fully satisfactory account of the data.

Declaration

The data presented in this thesis was obtained by the Nuclear Structure group of the University of Glasgow in collaboration with collegues from the Universities of Edinburgh and Mainz. I participated fully in all aspects of the preparation and execution of the experiment. The analysis and interpretation of this data is entirely my own work. This thesis was composed by myself.

Peter A. Wallace

Acknowledgements

First of all I wish to thank my supervisor, Professor Bob Owens, whose deep knowledge of all aspects of the subject has been an invaluable assistance during my studies at Kelvin Laboratory. Special mention is due also to Dr. Cameron McGeorge whose experience and enthusiasm have contributed in large measure to the success of the project.

Experimental work on this scale is of necessity a collaborative activity and I am indebted to everyone who participated in the development of the experimental system or who was involved in taking the data. Particular thanks are due to Drs. Jim Kellie and Sam Hall who constructed the liquid deuterium target and operated it thoughout the sometimes fraught data taking periods. I am grateful also for the efforts of Drs. John Annand, Ian Anthony, Ian Crawford, Steve Dancer and Douglas MacGregor without which the experiment could not have taken place. The interested participation of Dr. Derek Branford of Edinburgh University was also much appreciated.

I am grateful to Professors Ehrenberg and Schoch for making available to me the facilities of the Mainz Institut für Kernphysik. In particular I have benefited from many interesting conversations with Professor Schoch. I am similarly grateful to the members of his group at Mainz for their enthusiastic assistance during the experiment.

Back at Kelvin Lab I must thank our computer manager Mr Andy Sibbald for maintaining a reliable and 'user friendly' system which has greatly facilitated the analysis of the data and indeed the preparation of this thesis. The finished document also owes much to the steady hand of Mrs Eileen

Taylor who helped to prepare many of the diagrams. I must also mention the sterling work of the electronics and mechanical technicians without whose practical skills many ingenious ideas would have remained ideas.

I wish to thank Professors Laing and Hughes who as successive heads of the Glasgow University Physics and Astronomy department have provided me with funds to attend several conferences. I also gratefully acknowledge the support of the SERC in the form of a Research Studentship and further conference funding.

The great pleasure of life at Kelvin Laboratory has been the good natured atmosphere which pervades all aspects of scientific and social activity. This is a consequence of the friendly and helpful attitudes of all the members of scientific, technical and support staff without exception. However I must make special mention of my fellow students, both past and present, for their unique, highly individual contributions to life at the Krazy-K.

Finally, but most importantly, I wish to express my sincere gratitude to my parents for their unfailing support and encouragement during my student years. Not only did they 'put me up' during my research work but they succeeded in putting up with me !

Contents

Chapter 1

Photonuclear Reactions and the Deuteron

1.1 Introduction

1.1.1 Electromagnetic Interactions and the Nucleus

The electromagnetic interaction has proved to be a versatile tool for the study of nuclear physics. It is the best understood of the elementary forces and it possesses a number of features which can be employed advantageously to investigate various aspects of nuclear structure and dynamics. In relation to the strong nuclear force electromagnetism represents only a weak disturbance of the nuclear system under study. The photon may therefore penetrate the whole volume of the nucleus. This is in contrast to the behaviour of strongly interacting probes which suffer absorption at the nuclear surface and are therefore less sensitive to the interior of the nuclear wave function. Furthermore the relative weakness of the electromagnetic force implies that calculations based upon perturbation expansions may be performed reliably. The second advantage is that information can be obtained from electromagnetic nuclear reaction data in a way which is largely independent of nuclear physics input. What is measured is essentially a map of the electromagnetic charge and current densities in the system. This can subsequently be interpreted in terms of the motion of the nuclear constituents. If a hadronic probe were used it would be necessary to assume a particular model of the hadron-nucleus interaction in order to extract information on the structure of the nuclear target.

The absorption of real photons by nuclei yields information on various aspects of nuclear physics depending on the photon energy. At energies well below the pion threshhold the photoreaction cross-section is dominated by the giant dipole resonance. This is a collective mode of excitation of the nu-

cleus which contains much of the observed total photoabsorption strength in complex nuclei. The concept of a finite, predictable total energy integrated photoabsorption strength has been of great value in the development of photonuclear physics [3] [4] [5]. Sum rules, based only on very general considerations of quantum mechanics can provide predictions of the total integrated cross section to all final states while requiring only the relatively well known ground state wave function as input. One example is the Thomas-Reich-Kuhn sum rule for the total integrated electric dipole cross-section for a system of total charge Z.

$$\int_0^\infty \sigma_{E1}(E_\gamma)dE_\gamma = \frac{2\pi^2 e^2}{M}\frac{NZ}{A}(1+\kappa) = 60\frac{NZ}{A}(1+\kappa) \quad [\text{MeV mb}] \qquad (1.1)$$

In a system whose potential V contains only central terms the so-called enhancement factor $\kappa = 0$. In this case, i.e. non-interacting nucleons in a central potential, the sum rule obtains its classical value $60\frac{NZ}{A}$. In the presence of exchange terms or momentum dependent terms in the potential the enhancement factor κ has the form,

$$\kappa = \frac{AM}{NZe^2}\langle i|\left[[D_z, V], D_z\right]|i\rangle \qquad (1.2)$$

where D_z is the electric dipole operator and χ_i is the ground state of the system. Thus there exists a definite value for the strength of the total dipole response of a system of A nucleons and a calculable expression for the excess strength due to the presence of charged mesons etc. whose existence is implied by the use of a 'realistic' potential.

Above the giant resonance region collective excitation gives way to one-body and two-body absorption mechanisms. These yield structural information on few particle excitations and dynamical information on two-body

correlations via 'quasideuteron' mechanisms. At still higher energies pion photoproduction experiments shed light on pion and Δ-resonance propagation in nuclear matter. In such experiments the penetrative nature of the photon is especially valuable. The exotic particle is created on or near mass shell in the interior of the nuclear volume without the strong surface absorption effects seen in complementary pion scattering experiments. In this sense the nucleus acts as a laboratory for the study of subnuclear phenomena.

Electron scattering from the nucleus may be described to a high degree of accuracy by the one-photon exchange approximation in which the Mott cross-section [6] for a point nucleus is multiplied by a form factor which describes the spatial extension of the charge and current distribution represented by the nucleus. The valuable feature of virtual photons is that the energy transferred by the photon, ω, and the momentum transferred, q, can be adjusted independently. By varying the momentum transfer for elastic scattering it is possible to map out the charge form-factor of the nucleus and thus its ground state charge density. Inelastic scattering at low excitation provides information on analogous transition densities for bound state excitations. At higher energies the information on continuum transitions is complementary to that obtained with high energy real photons with the added advantage that q and ω may be varied independently to map out a surface of nuclear electromagnetic response. The $q = \omega$ relation of real photons does not in fact represent a limitation upon their usefulness, since the large momentum mismatch involved in the absorption of a real photon by a single nucleon results in the enhancement of the relative importance of two-body mechanisms, wherein lies much of the current interest in the study of nuclear dynamics.

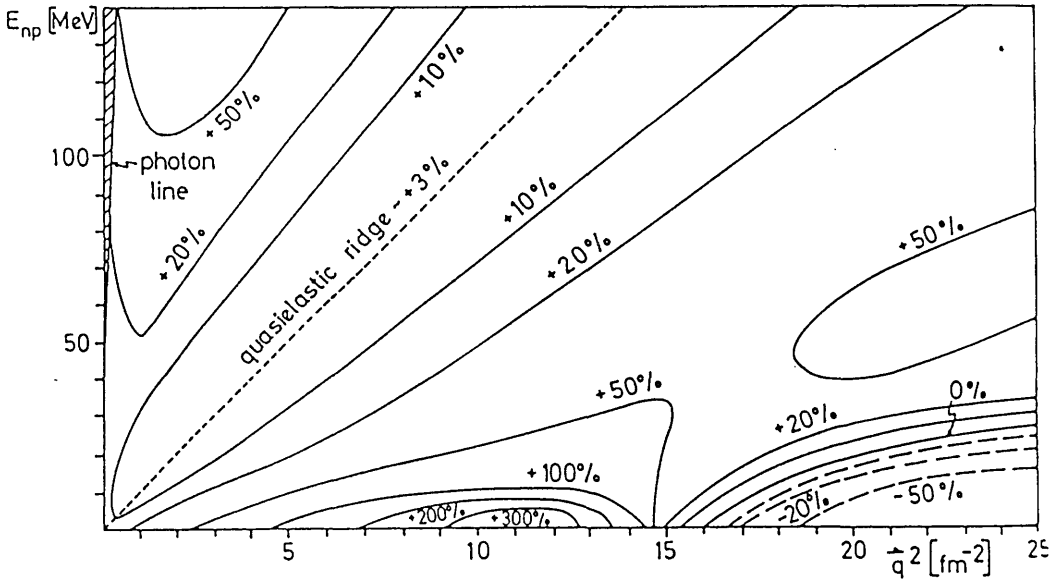

Figure 1.1: *relative contribution of exchange effects in the transverse inelastic form factor for $D(e,e')$ plotted as a function of q^2 (momentum transfer squared) and E_{np} (relative energy of n-p system) [7].*

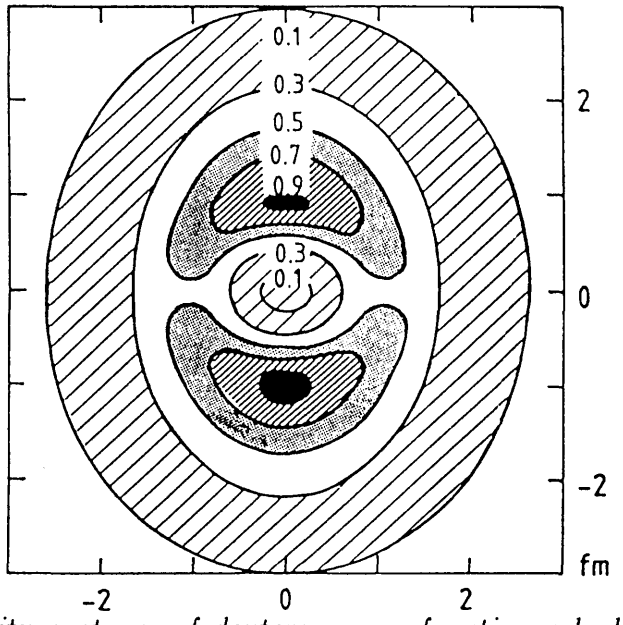

Figure 1.2: *Density contours of deuteron wave function calculated from the Paris potential (shown aligned along spin axis)*

An example [7] of how various aspects of the nuclear response may be emphasised by suitable choice of kinematics is shown in figure 1.1 . The relative contribution of exchange effects in the transverse inelastic form factor for $D(e,e')$ is plotted as a function of q^2 (momentum transfer squared) and E_{np} (relative energy of the np system). Large corrections are seen in the threshhold region ($E_{np} \approx 0$) while in the quasielastic region ($\omega \simeq \frac{q^2}{2M_{nucleon}}$) the form-factor is due almost entirely to the one-body absorption process. Going toward the real photon line at higher E_{np} exchange effects again enhance the form factor considerably, leading eventually to real Δ excitation.

1.1.2 The Place of the Deuteron in Nuclear Physics

The significance of the deuteron in nuclear physics approaches that of the hydrogen atom in atomic physics and it has been studied both theoretically and experimentally since the earliest days of the subject [1] [2]. Unlike the hydrogen atom, however, the deuteron has no discrete excited states and the interest lies not in spectroscopy but in the ground state properties. From the study of such static properties of the deuteron as the binding energy, magnetic dipole moment and electric quadrupole moment emerges a picture of a system bound by a complex spin, isospin and momentum dependent interaction. A calculation [11] of the deuteron probability density using a wave function derived from the Paris potential is shown in figure 1.2.

Radiative processes, particularly two body photodisintegration and it's inverse, n-p capture, are the simplest reactions involving the deuteron. In these processes the interaction of the two-nucleon system and the well understood electromagnetic force is observed cleanly, uninfluenced by complex

nuclear structure effects. The interpretation of such experiments is relatively unambiguous since it is free from the approximations required in a many-body system.

In a nucleons-only picture the deuteron is a two body system for which exact wave functions are obtained by solving the Schrödinger equation for a realistic N-N potential. Such potentials are derived from N-N scattering data and so reactions involving the deuteron test the consistency of the interaction model for bound and free nucleons. In such a model the most significant exchange current effects are included implicitly. In a model where meson exchange and the formation of nucleon resonances are included explicitly then the few-body nature of the deuteron system lends itself to a treatment where the amplitude is expanded in the leading order terms of the S-matrix expansion.

1.1.3 Deuteron Photodisintegration

The structure of the deuteron lends itself to the investigation of particular aspects of the nuclear force. Electron scattering measurements [9] have shown that the r.m.s. charge radius of the deuteron is 2.095(6)fm That is to say, its mean density is significantly less than that of other light nuclei for example ^{4}He whose charge radius is 1.674(12)fm or ^{12}C at 2.446(10)fm [10] This rather extended spatial structure taken together with the small binding energy (2.2 MeV) implies that the momentum space wave function must fall off rapidly with increasing nucleon momentum. However the absorption of a real photon by a nucleon involves a large mismatch between the momentum of the initial and final states and therefore requires the nucleon to have a large initial mo-

mentum in order to balance the reaction kinematics. For example, a $D(\gamma,p)n$ reaction induced by a 100MeV photon resulting in the emission of a proton at 90 °requires an initial momentum of 330 MeV/c. This is very much greater than the typical momenta available in the deuteron. Figure 1.3 shows the nucleon momentum distribution calculated using the Reid soft core potential [8]. The distribution falls to 20 % of its maximum value at 50 MeV/c, 2% at 100 MeV/c and 0.01 % at 300 MeV/c nucleon momentum. This lack of high momentum components in the wave function results in the suppression of one-body photoabsorption mechanisms relative to exchange mechanisms where both nucleons participate in the reaction and combine to provide the required momentum. Thus the deuteron is a particularly suitable system for the study of exchange effects. An illustration of the importance of exchange mechanisms is provided by figure 1.4 which shows a calculation of the total cross-section for deuteron photodisintegration as a function of energy. [12]. It is seen that the one-body (impulse approximation) calculation very significantly underestimates the trend of the data at higher energies and the exchange contribution gains in importance with increasing energy. In addition to the non-resonant meson exchange terms (MEC) there is also a contribution from Δ excitation followed by decay to an np final state. The decay occurs by means of pion emission and reabsorption and so provides a mechanism for the sharing of the initial momentum between the two nucleons. This may also occur in the final state. The strength of the rescattering term around 300 MeV indicates that the virtual Δ excitation is an important final state interaction.

Explicit energy-integration of such theoretical cross-sections indicate an enhancement of the classical dipole sum rule value of approximately 0.5 .

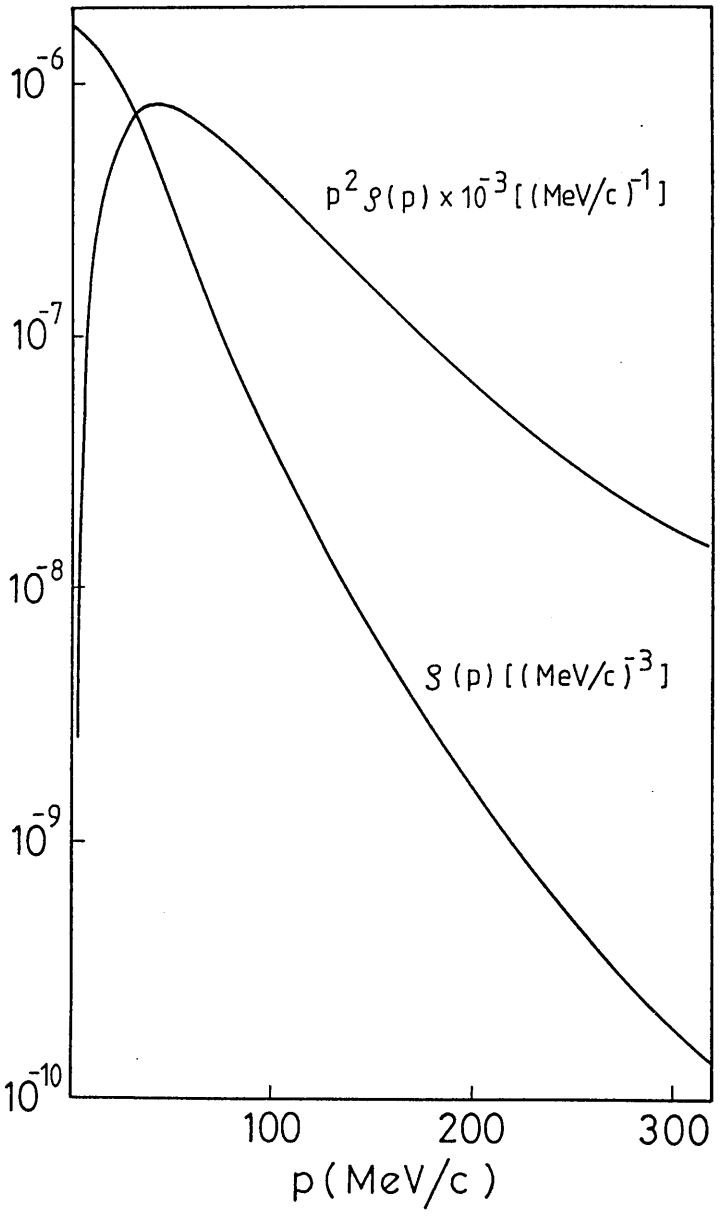

Figure 1.3: *Deuteron momentum distribution for the Reid soft core potential. [8]*

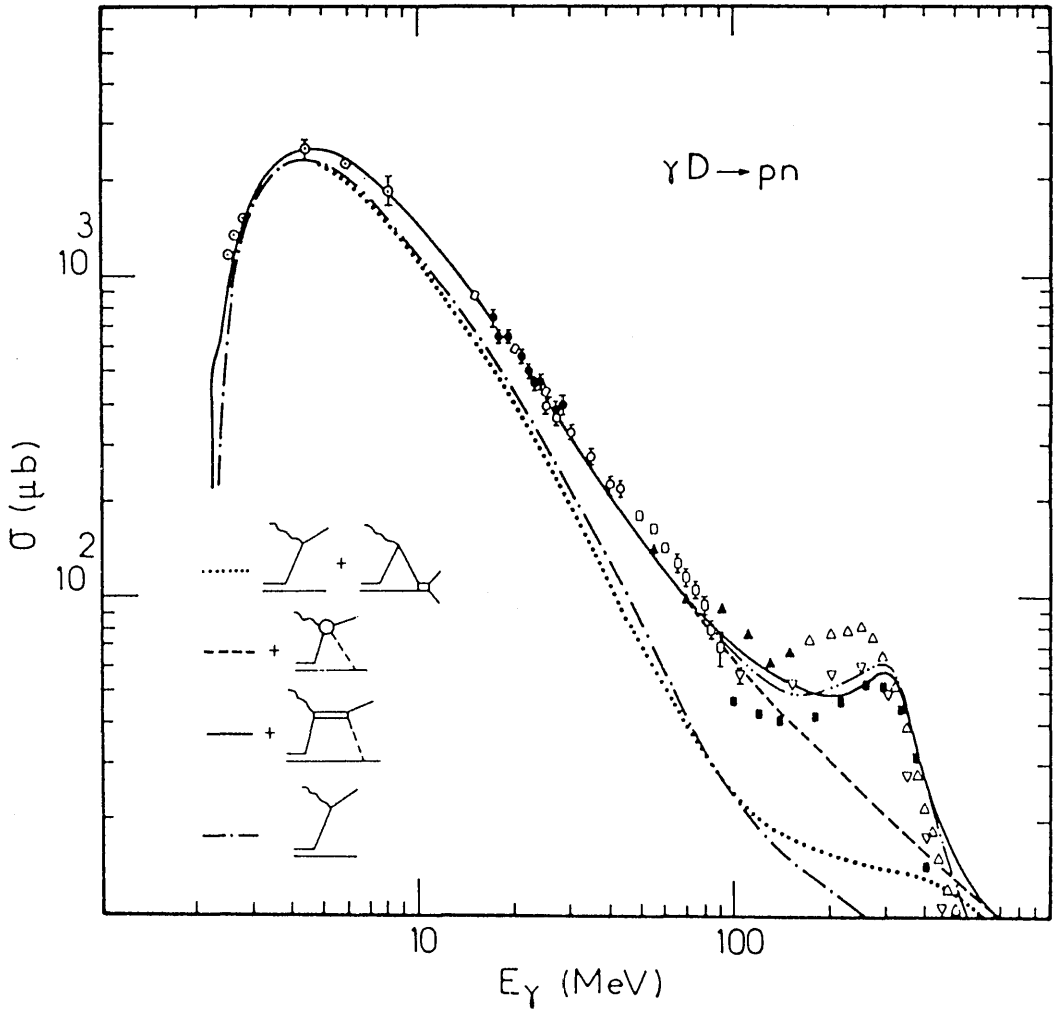

Figure 1.4: *Total cross-section for deuteron photodisintegration [12].*
dash dot line: Impulse approximation (IA)
dotted line : IA + Rescattering (RS)
dashed line : IA + RS + Meson exchange currents (MEC)
solid line : IA + RS + MEC + Nucleon isobar current (IC)
data references as given in [12]

This is in fair agreement with the enhancement factor obtained from the sum rule using a realistic potential and with the measured value of the energy integrated cross-section [13].

The deuteron also provides an ideal laboratory in which to study the very poorly known N-Δ interaction. Although Δ formation effects in deuteron photodisintegration are most significant in the region of the resonance (E_γ = 200-300 MeV) there are thought to be non-negligible effects below the pion threshold due to formation and decay of a virtual Δ in the intermediate state.

A great deal of theoretical effort has recently been expended on the study of the $D(\gamma,p)$ process at 0°, that is, for emission of the proton in the forward direction. In the simplest model of the reaction, i.e. a pure S-state deuteron and only E1 transitions, this process is forbidden by angular momentum conservation. The existence of a finite forward cross-section is due partially to spin flip M1 transitions from the $^3S_1$ state to the $^1S_0$ but also to $^3D_1 \longrightarrow ^3P$ transitions from the D-state component in the deuteron wave function which arises from the tensor part of the N-N interaction. As a result of the D-state admixture the deuteron possesses an electric quadrupole moment Q_D. However non-relativistic potential models [14] [15] [16] [17] which correctly predict Q_D yield too high a forward $D(\gamma,p)$ cross-section. In recent work [18] [19] the agreement has been improved by the inclusion in the charge density of spin dependent corrections of relativistic order which interfere with the D-state transition amplitude. In addition to these corrections to the normal non-relativistic one body charge density the effect of two body charge density operators arising from pair excitation processes have been considered by some authors [20]. The inclusion of these terms appears to improve the agreement

for pseudovector πN coupling but has the opposite effect for pseudoscalar coupling. Such effects have now been introduced into calculations [21] [22] of the angular distribution resulting in modification of both the shape and magnitude of the cross-section.

In conclusion, a great deal of valuable information about the nuclear force may be obtained from the study of the cross-section for deuteron photodisintegration. However, as well as explicit differences in the nuclear physics input of the different theoretical treatments there are discrepencies due to the use of varying approximations and calculational techniques. Such questions are of general interest in the field of strong interaction dynamics and since the deuteron is the simplest nucleus it is an ideal system for the study of both the problems of the physics of the N-N force and also those of a more 'technical' nature. Both of these effects give rise to 10-20 % differences in the prediction of the differential cross-section and so in order to be useful new data should have a total uncertainty of not more than 5-10 %.

1.2 The Nuclear Electromagnetic Current

The purpose of this section is to discuss the theoretical techniques used to describe the interaction of photons with the nucleus. The photon interacts with all the charged constituents of the nuclear system including the mesons which are exchanged between the nucleons. Furthermore the full nuclear wave function contains not only neutrons and protons but also nucleon resonances. The total system of charges and currents seen by the photon therefore includes the contributions of mesons, nucleons and nucleon resonances. The nuclear wave function is of course constrained by the requirement that electric charge

be conserved.

There are two approaches to the construction of the interaction matrix element. The wave function may be projected onto the space of nucleons only in which case the meson exchange effects must be included in the nucleonic current. This allows the use of conventional nuclear wave functions but presents problems in the choice of the two-body current terms. Alternatively the mesons may be included explicitly in the interaction, usually in a Feynmann diagram type calculation, but this leaves the problem of how to produce a consistent wave function. The problem of the description of the total nuclear current is central to the understanding of nuclear photoreactions and the very light nuclei, especially the deuteron, provide the ideal testing ground for theoretical ideas.

The interaction of the electromagnetic field with a structureless, charged particle of mass M, charge e and magnetic moment μ is well understood. However, the picture is modified considerably if the particles possess internal structure. This is demonstrated in high energy *e-p* scattering where the finite size of the proton is measurable and in hadron photo-and electroproduction experiments on the nucleon where the electromagnetic probe interacts explicitly with the meson field. The meson field mediates the strong force between nucleons and its interaction with the electromagnetic field results in the existence of photoabsorption mechanisms involving more than one nucleon.

In the deuteron the photon interacts with both the internal degrees of the bound system (meson exchange currents etc.) and the internal degrees of freedom of the nucleons themselves (eg. Δ-resonance formation). These effects are strongly interelated through $N\pi \rightleftharpoons \Delta$ processes in the nucleus and

in a QCD based quark-gluon picture may become totally blurred.

The power of the electromagnetic interaction as a probe of nuclear dynamics lies in the extent to which information can be extracted from experimental data in a way which is independent of nuclear models. This is exemplified in the existence of photoabsorption sum rules and current conservation rules which allow the calculation of observables in a way which implicitly includes the effects of the internal dynamics of the system.

1.2.1 The Interaction Hamiltonian

The most versatile link between theoretical variables and experimental observables in nuclear physics is contained in the formalism for scattering reactions. The Scattering matrix (S-matrix) is defined as

$$S_{fi} \equiv \langle f|\hat{S}|i\rangle \equiv \delta_{fi} - i(2\pi)^4\delta^4(p_f - p_i)T_{fi} \tag{1.3}$$

i.e. the matrix element of $\hat{S}$ the scattering operator between the initial and final states of the system. Transition probabilities are given by $|T_{fi}|^2$ where T_{fi} is the reaction matrix. T_{fi} includes the amplitudes for all processes by which the interaction part of the Hamiltonian, H_{int}, couples the initial state of the system to a particular final state. The S-matrix can be expanded in a series of terms of increasing order in H_{int}, the details of which are given in many texts eg. [26] . However, for photoabsorption processes described by a purely electromagnetic interaction Hamiltonian then only the lowest order term need be considered. The transition matrix element for electromagnetic interactions takes the form

$$T_{fi} = \langle f|H_{int}|i\rangle \equiv \langle f|\int A^{\mu}(\vec{x})J_{\mu}(\vec{x})d^3x|i\rangle \tag{1.4}$$

where J_μ is the nuclear current density operator and A_μ is the photon operator.

$$\begin{aligned} J_\mu(\vec{x}) &= (\rho(\vec{x}), \vec{J}(\vec{x})) \\ A_\mu(\vec{x}) &= (\Phi(\vec{x}), \vec{A}(\vec{x})) = \sqrt{\frac{2\pi}{\omega_\gamma}} \varepsilon_\mu e^{-i\vec{k}\cdot\vec{x}} \end{aligned} \tag{1.5}$$

In the case of real photons where there are no source charges nearby the gauge invariance principle (appendix B) allows one to choose $\Phi = 0$ in which case the transition matrix element becomes

$$T_{fi} = \langle f | - \int \vec{A}(\vec{x}) \cdot \vec{J}(\vec{x}) d^3x | i \rangle \tag{1.6}$$

Thus H_{int} factorises into a plane wave representing the photon and a current J_μ which contains the nuclear physics input to the problem. Although it has been conventional in nuclear physics to use the Schrödinger equation as a starting point for calculations there are advantages in the use of the Dirac equation for the development of the electromagnetic interaction Hamiltonian. The Dirac equation described the motion of a spin-$\frac{1}{2}$ particle and therefore the magnetic terms in the Hamiltonian arise naturally and do not have to be added 'by hand' as is the case with the nonrelativistic formalism. In addition to this, several modern calculations have shown that there exist relativistic effects which significantly modify the photodisintegration cross-section. These terms also appear naturally in the nonrelativistic reduction of the Dirac Hamiltonian.

The Dirac equation for a particle of charge e and mass M can be written

$$i\frac{\partial \psi(x)}{\partial t} = H_D \psi(x) \tag{1.7}$$

where the Dirac Hamiltionian H_D has the form

$$H_D = \vec{\alpha} \cdot \vec{p} + \beta M \tag{1.8}$$

and $\psi(x)$ are plane wave solutions defined in appendix A. In the presence of electromagnetic interactions H_D is modified as follows.

$$i\hbar\frac{\partial}{\partial t} \longrightarrow i\hbar\frac{\partial}{\partial t} - e\Phi(x), \qquad -i\hbar\nabla \longrightarrow -i\hbar\nabla - \frac{e}{c}\vec{A}(x) \tag{1.9}$$

where $\vec{A}$ and Φ are the vector and scalar e.m. potentials. This is the form for an ideal Dirac particle with a gyromagnetic ratio of 2. To accommodate nucleons, whose magnetic moments are altered by strong interaction effects the total magnetic moment $\hat{\mu}$ is defined as

$$\hat{\mu} \equiv e[1+\kappa] \equiv \frac{e}{2}[\mu_s + \mu_v\tau_3] \tag{1.10}$$

where $\hat{\kappa} \equiv e\kappa$ is the anomalous magnetic moment, ($\kappa_p = 1.79$; $\kappa_n = -1.91$) μ_s and μ_v are defined as the isoscalar and isovector magnetic moments ($\mu_s = 0.88$; $\mu_v = 4.71$) and τ_3 is the 3rd component of the isospin operator. similarly the nucleonic charge is defined as

$$\hat{e} = \frac{e}{2}[1+\tau_3] \tag{1.11}$$

The full Hamiltionian for 'Dirac' nucleons in a electromagnetic field includes additional terms due to the existence of the anomalous magnetic moments.

$$H_D = \beta M + \vec{\alpha}\cdot(\vec{p} - \hat{e}\vec{A}) + \hat{e}\Phi - \frac{\hat{\kappa}}{2M}\beta\vec{\sigma}\cdot\vec{B} + \frac{i\hat{\kappa}}{2M}\beta\vec{\alpha}\cdot\vec{E} \tag{1.12}$$

where $\vec{E}$ and $\vec{B}$ are the electric and magnetic fields corresponding to $\vec{A}$ and Φ. It is convenient to work with a non-relativistic reduction of this Hamiltonian, which allows the (positive energy) nucleon wave functions to be represented by two-component (Pauli) spinors. This is achieved by means of the Foldy-Wouthuysen transformation (Appendix A). The non-relativistic Hamiltonian has the form

$$H_{NR} = H_0 + H_{int} \tag{1.13}$$

where

$$H_0 = M + \frac{\vec{p}^2}{2M} \tag{1.14}$$

and

$$H_{int} = \hat{e}\Phi - \hat{e}\frac{\vec{p}\cdot\vec{A}}{M} - \frac{\hat{\mu}}{2M}\vec{\sigma}\cdot\vec{B} - \frac{2\hat{\mu}-\hat{e}}{4M^2}\vec{\sigma}\cdot\vec{E}\times\vec{p} - \frac{2\hat{\mu}-\hat{e}}{8M^2}\nabla\cdot\vec{E} \tag{1.15}$$

These terms represent an electric monopole interaction, an electric dipole interaction, a spin-magnetic dipole term, a spin-orbit interaction and lastly the Darwin-Foldy term which gives rise to the so-called *Zitterbewegung* motion of a Dirac particle. This is an oscillatory motion with a frequency of $\frac{2Mc^2}{\hbar}$ which is superimposed on the average motion. Its origin lies in the interference of the positive and negative energy components in the particle's wave function.

1.2.2 The Nucleonic EM Current

The nucleonic EM current operator may be defined as

$$\hat{J}_\mu(\vec{x}) \equiv \left.\frac{\partial H_{int}}{\partial A^\mu}\right|_{A^\mu=0} \tag{1.16}$$

Applying this to H_{NR} defined above yields the following results

$$\rho(\vec{x}) = \hat{e}\delta^3(\vec{x}-\vec{r}) + \frac{2\hat{\mu}-\hat{e}}{8M^2}\nabla^2\delta^3(\vec{x}-\vec{r}) + \frac{2\hat{\mu}-\hat{e}}{4M^2}\nabla\delta^3(\vec{x}-\vec{r})\cdot\vec{\sigma}\times\vec{p} \tag{1.17}$$

and

$$\vec{J}(\vec{x}) = \hat{e}\frac{\vec{p}}{M}\delta^3(\vec{x}-\vec{r}) + \frac{\hat{\mu}}{2M}\nabla\times\vec{\sigma}\,\delta^3(\vec{x}-\vec{r}) \tag{1.18}$$

where $\delta^3(\vec{x}-\vec{r})$ is the position projection operator onto the nucleon position vector $\vec{r}$. The corresponding momentum space operators are the fourier transforms of the configuration space expressions.

$$J_\mu(\vec{k}) = \int d^3x\, e^{-i\vec{k}\cdot\vec{x}} J_\mu(\vec{x}) \tag{1.19}$$

therefore

$$\rho(\vec{k}) = \hat{e}\, e^{-i\vec{k}\cdot\vec{r}} - \frac{2\hat{\mu} - \hat{e}}{8M^2}\vec{k}^2 e^{-i\vec{k}\cdot\vec{r}} + \frac{2\hat{\mu} - \hat{e}}{4M^2}\vec{k}\cdot\vec{\sigma}\times\vec{p}\, e^{-i\vec{k}\cdot\vec{r}} \tag{1.20}$$

and

$$\vec{J}(\vec{k}) = \hat{e}\frac{\vec{p}}{M}e^{-i\vec{k}\cdot\vec{r}} - \frac{i\hat{\mu}}{2M}\vec{k}\times\vec{\sigma}\, e^{-i\vec{k}\cdot\vec{r}} \tag{1.21}$$

1.2.3 Siegert's Theorem

The current derived above describes the interaction of the electromagnetic field with a single charged particle. However, as has been noted, the most important photoabsorption mechanisms above a few tens of MeV involve two body currents. these present a very much more complex theoretical problem. The use of explicit exchange currents greatly increases the theoretical uncertainties in the calculation of the matrix elements as there is at present no unambiguous prescription for their specification. It is possible, however, to calculate at least the electric transitions in a fashion which implicitly takes into account the presence of meson exchange currents. The principle is to express the nuclear current density in terms of the rather better known nuclear charge density by means of the charge-current continuity equation. The charge density is easier to calculate because the charged mesons whose motion contributes significantly to the current density have zero net charge on average and so do not directly affect the charge density. Nonetheless their presence is indirectly felt because the distribution of the protons' charge is governed by motion in a potential which is constructed from a meson exchange theory. These ideas are embodied in Siegert's theorem which states that the electric multipole transitions in the long wave limit including exchange current effects are determined by the one body charge density.

The nuclear current density operator satisfies the following continuity equation,

$$\nabla \cdot \vec{J} + i\,[H, \rho] = 0 \tag{1.22}$$

which guarantees the gauge invariance of the theory. In the general case the charge and current densities may be written as follows,

$$\vec{J} = \vec{J}_{(1)} + \vec{J}_{(2)} + \cdots \tag{1.23}$$

$$\rho = \rho_{(1)} + \rho_{(2)} + \cdots \tag{1.24}$$

where $\vec{J}_{(1)}$ and $\rho_{(1)}$ represent the current and charge density operators for non-interacting particles and $\vec{J}_{(n)}$,$\rho_{(n)}$ are the modifications to those currents introduced by n-particle interaction effects. These modifications are due to the exchange of charged virtual mesons between the nucleons. In the non-relativistic 'static' limit where the meson masses are neglected the charge density fluctuations introduced by charged meson exchange must cancel even on very short time scales and then the n-body charge densities $\rho_{(n)}$ may be set = 0 . If this approximation is accepted, the continuity equation separates as follows:

$$\nabla \cdot \vec{J}_{(1)} + i\left[T, \rho_{(1)}\right] = 0 \tag{1.25}$$

$$\nabla \cdot \vec{J}_{(2)} + i\left[V, \rho_{(1)}\right] = 0 \tag{1.26}$$

since current continuity must be satisfied independently *up to and inclusive of* each order (n).

The commutator in equation 1.26 does not vanish for exchange or momentum dependent terms in the potential. If V is written as $V = V_{o.b.} + V_{exc}$ (o.b.: one body) where $[V_{o.b.}, \rho_1] = 0$ but $[V_{exc}, \rho_1] \neq 0$ then equation 1.26 becomes

$$\nabla \cdot \vec{J}_{(2)} + i\left[V_{exc}, \rho_{(1)}\right] = 0 \tag{1.27}$$

Thus, the matrix elements of the exchange current operators whose existence is implied by the use of a 'realistic' potential containing V_{exc} can be expressed in terms of the charge operator in a form which *implicitly* includes their effects without the need for any knowledge of their explicit form. This result is presented formally in Appendix B which follows the treatment of Arenhövel [23]. A simpler illustration is given below, in the 'long wave limit' where $k_\gamma x \ll 1$ over nuclear dimensions. In this approximation all multipoles other than $E1$ may be neglected.

In the long wave limit the exchange current $\vec{J}_{(2)}$ takes a simple form,

$$\vec{J}_{(2)} = -i\left[V_{exc}, \vec{D}\right] \tag{1.28}$$

where $\vec{D} = \sum_{\alpha=1}^{A} e_\alpha \vec{x}_\alpha \delta^3(\vec{x} - \vec{x}_\alpha)$. The interaction Hamiltonian is now,

$$H_{int} = -\int \vec{A}(\vec{x}) \cdot \left(\vec{J}_{(1)}(\vec{x}) + \vec{J}_{(2)}(\vec{x})\right) d^3x \equiv H_{o.b.} + H_{exc} \tag{1.29}$$

In the long wave limit the two parts of the Hamiltonian have the form:

$$H_{o.b.} = \sqrt{\frac{2\pi}{\omega_\gamma}} \sum_{\alpha=1}^{A} \frac{e_\alpha}{M} \vec{\varepsilon}_\lambda \cdot \vec{p} = i\sqrt{\frac{2\pi}{\omega_\gamma}} \left[T, \vec{\varepsilon}_\lambda \cdot \vec{D}\right] \tag{1.30}$$

$$H_{exc} = i\sqrt{\frac{2\pi}{\omega_\gamma}} \left[V, \vec{\varepsilon}_\lambda \cdot \vec{D}\right] \tag{1.31}$$

Taking these together, H_{int} has the form:

$$H_{int} = i\sqrt{\frac{2\pi}{\omega_\gamma}} \left[H, \vec{\varepsilon}_\lambda \cdot \vec{D}\right] \tag{1.32}$$

This is known as the Siegert Dipole operator.

1.2.4 The Multipole Expansion of the Transition Operator

The use of Siegert's theorem outlined above can be developed more formally in the conventional approach to photodisintegration calculations which use

an expansion of the transition operator in electric and magnetic multipoles. The leading terms of the electric multipole operators can be expressed as Siegert operators. This section follows the work of Arenhövel [23] who has been largely responsible for the development of the formalism.

The general form of the matrix element for a photonuclear reaction is, from equation 1.6,

$$\langle f| - \int \vec{A} \cdot \vec{J} d^3x |i\rangle \equiv \sqrt{\frac{2\pi}{\omega_\gamma}} \langle f|T(\vec{k}_\gamma, \vec{J}, \lambda)|i\rangle \tag{1.33}$$

Where $T(\vec{k}_\gamma, \vec{J}, \lambda)$ is a transition operator which may be expanded into electric and magnetic multipole terms as follows.

$$T(k_\gamma, \vec{J}, \lambda) = -\sqrt{2\pi} \sum_L i^L \sqrt{2L+1} \left[T_{el}^{[L]}(k_\gamma, \vec{J}, \lambda) + \lambda T_{mag}^{[L]}(k_\gamma, \vec{J}, \lambda) \right] \tag{1.34}$$

The explicit expressions for the T operators defined in this section are given in appendix B. The electric multipole operator $T_{el}^{[L]}$ may be split into two parts.

$$T_{el}^{[L]}(k_\gamma, \vec{J}, \lambda) = T_a^{[L]}(k_\gamma, \vec{J}, \lambda) + T_b^{[L]}(k_\gamma, \vec{J}, \lambda) \tag{1.35}$$

where $T_b^{[L]}$ is one order higher in $(k_\gamma x)$ than $T_a^{[L]}$. Thus in the long wave approximation ,i.e. $k_\gamma x \ll 1$ over nuclear dimensions, T_a gives the dominant contribution to the electric transitions. The term $T_a^{[L]}$ may be transformed by partial integration and the use of the current conservation equation 1.22 as follows (appendix B).

$$T_a^{[L]}(k_\gamma, \vec{J}, \lambda) \rightarrow T_a'^{[L]}(k_\gamma, \rho, \lambda) \tag{1.36}$$

This expression is the exact statement of Siegert's theorem expressing the transverse electric multipole moments in terms of the longitudinal charge moments. In the assumption that interaction effects do not introduce many-body

charge density operators $\rho(\vec{x})$ may be set equal to $\rho_{(1)}(\vec{x})$. This is Siegert's hypothesis, discussed previously.

There now exists a choice of operators with which to perform calculations of electric multipole transitions. Since such calculations normally involve the use of an approximate exchange current consisting of a realistic potential plus a π-exchange current it is instructive to separate the operator into a *normal* part, $T^{[L]}_{nor}$, not requiring any explicit knowledge of the exchange current $\vec{J}_{(2)}$ and an *exchange* part, $T^{[L]}_{exc}$, dependent on $\vec{J}_{(2)}$. In terms of the transformation performed above these operators have the following form in the two cases, with (I) and without (II) the use of Siegert's theorem.

I With Siegert theorem:

- $$T^{[L]}_{nor[1]} = T'^{[L]}_{a}(k_\gamma, \rho_{(1)}, \lambda) + T^{[L]}_{b}(k_\gamma, \vec{J}_{(1)}, \lambda) \tag{1.37}$$

- $$T^{[L]}_{exc[1]} = T^{[L]}_{b}(k_\gamma, \vec{J}_{(2)}, \lambda) \tag{1.38}$$

II Without Siegert theorem:

- $$T^{[L]}_{nor[2]} = T^{[L]}_{el}(k_\gamma, \vec{J}_{(1)}, \lambda) \tag{1.39}$$

- $$T^{[L]}_{exc[2]} = T^{[L]}_{el}(k_\gamma, \vec{J}_{(2)}, \lambda) \tag{1.40}$$

For the sum of normal and exchange contributions the two approaches are equivalent provided the exchange current $\vec{J}_{(2)}$ is consistent with the two body interaction V_{exc}, that is provided equation 1.26 is satisfied. However where

an approximate exchange current is used then the first approach (invoking Siegert) is preferable because the dominant part is consistent and $T^{[L]}_{exc[1]}$ is less sensitive to short range inconsistencies in $\vec{J}_{(2)}$ since it is of higher order in $(k_\gamma x)$.

Figure 1.5 shows the result of such a calculation using both approaches [23]. The Reid soft core potential was used and multipoles up to $L = 4$ were included. It is seen that the Siegert operator $T^{[L]}_{nor[1]}$ accounts for nearly all of the exchange contribution, namely 98 % at 10 MeV and 87 % at 100 Me V . The small inconsistency in the total cross-section calculated by the two methods is due to the use of an approximate exchange current.

It has now become standard practice to include relativistic corrections to the charge density used in Siegert type calculations. The inclusion of the spin-orbit and Darwin-Foldy terms in the one-body charge density as shown in equation 1.24 was pioneered by the Florence group [19]. Other effects resulting from a non-vanishing two-body charge density have also been studied [20].

It is important to recall that it is still necessary to use explicit meson exchange and Δ excitation currents in the magnetic transition operators. The $M1$ transitions in particular rapidly gain in importance at energies approaching the Δ resonance.

1.2.5 Explicit Meson Exchange Effects

It is possible explicitly to include mesonic degrees of freedom in the interaction Hamiltonian in such a way that the coupling of the photon to exchanged

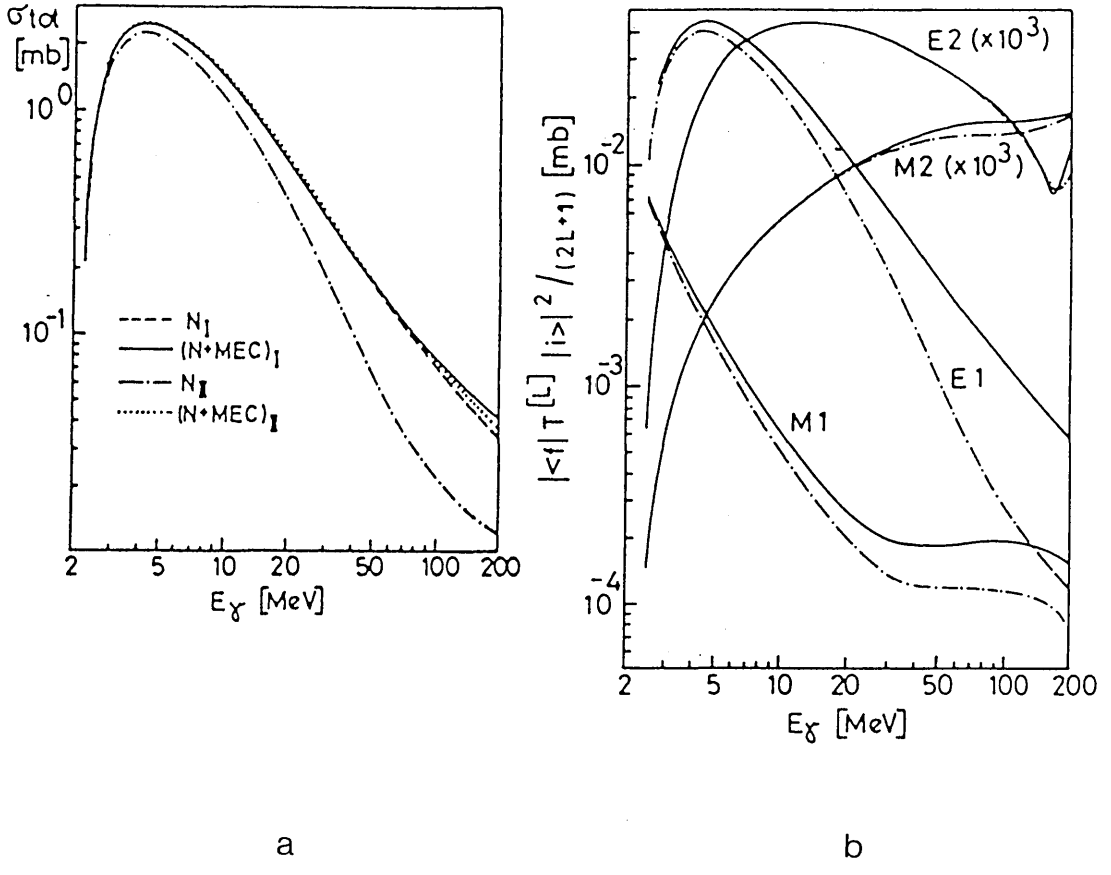

Figure 1.5: *Results of [23] for $D(\gamma,p)n$ calculated with and without the use of Siegert's operator theorem.*
(a) Total cross section for photodisintegration.
dashed line: with Siegert operators, solid line: Siegert operators + MEC, dot-dash line: non-Siegert one body operators, dotted line: non-Siegert operators + MEC
(b) Multipole decomposition of the photodisintegration cross-section.
solid line: Siegert operators, dot-dash line: non-Siegert one body operators.

mesons can be treated directly. The full Hamiltonian may be written as:

$$H = H_N + H_\gamma + H_\pi + H_{N\pi} + H_{N\gamma} + H_{\pi\gamma} + H_{N\pi\gamma} \qquad (1.41)$$

where $H_N + H_\gamma \equiv H_0$ and $H_{N\gamma} \equiv H_{int}$ in the notation previously used. It is now necessary to expand the S-matrix to extract explicitly all the processes involving the absorption of one photon by the nuclear system. These processes, which may involve the interaction of several mesons and nucleons are conveniently represented by momentum space graphs which have a one-to-one correspondence with the terms in the S-matrix expansion. This is described in many texts e.g. [25] [26]. The Feynmann diagrams representing the one and two-body photodisintegration processes are shown in figure 1.6 which is taken from [12] where such a calculation is described. In this calculation the pion photoproduction amplitudes (diagrams **III** in figure 1.6) are modified to describe the emission of virtual pions which are subsequently absorbed on the second nucleon. The pion reabsorption amplitudes (figure 1.6 **II**) also include the excitation of virtual intermediate state Δ resonances. The rescattering amplitude is calculated by iteration of the one pion exchange process. The deuteron current (**I.a**) is a correction term which is necessary to restore gauge invariance to the total amplitude (appendix B). This gauge violation is related to the 'double counting' of diagrams **IV.a** and **b** which are included implicitly in the initial and final state wave functions. The wave functions used in the calculation of [12] were derived from the Reid soft core potential. The more recent work [68] uses the Paris potential.

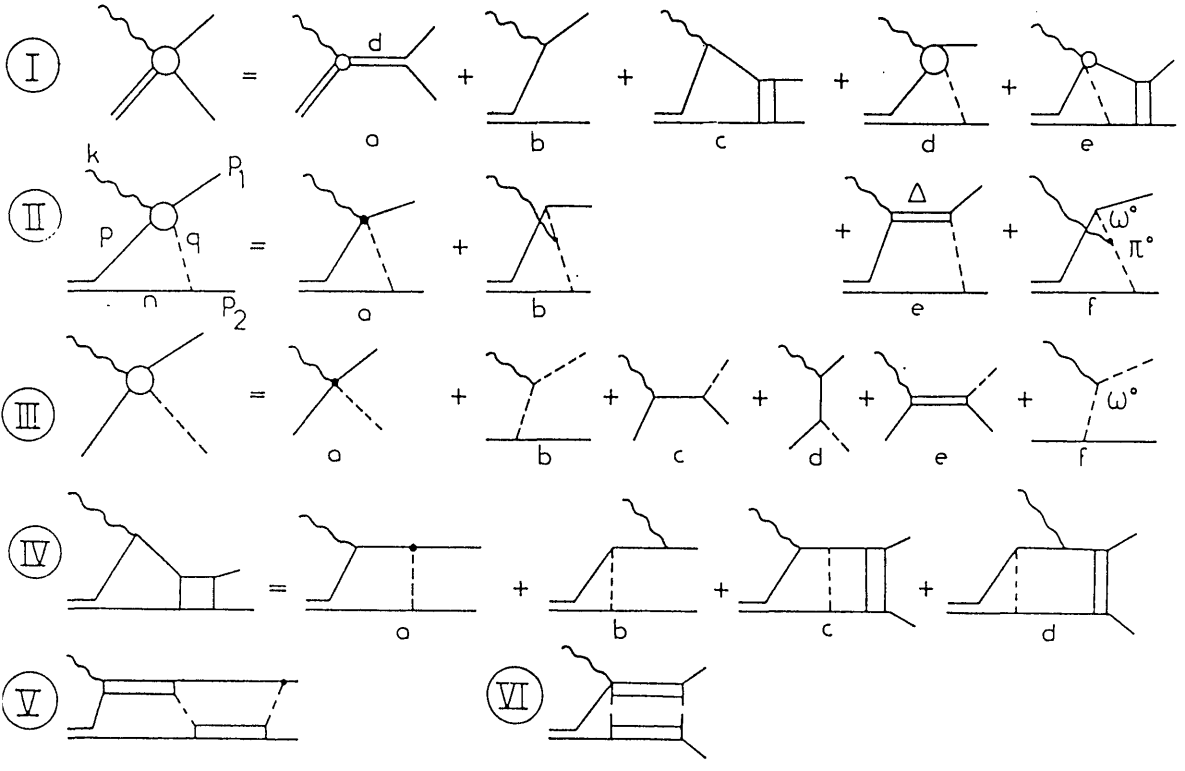

Figure 1.6: *Amplitudes considered in the calculation of [12]*
I: *Structure of the photodisintegration amplitude. (a) effective deuteron current (b) nucleon current (c) final state interactions (rescattering amplitude) (d) pion reabsorption amplitude (e) pion reabsorption and f.s.i.*
II *Composition of pion reabsorption amplitude.*
III *Pion photoproduction amplitudes which are used to form* **II.**
IV *Rescattering amplitude (iteration of meson exchange terms)*
V,VI *Two-loop $N - \Delta$ rescattering*

Chapter 2

Photonuclear Experiments

2.1 Introduction

The production of intense beams of photons has always presented a technical challenge to photonuclear experimentalists. The ideal photon beam for most experiments would be monoenergetic and would be intense enough to measure very small electromagnetic cross-sections in a reasonable length of time. In addition, the photon flux would be known accurately either by direct measurement or by inference from the method of photon production. Unfortunately, it has proved difficult to produce a beam which simultaneously possesses even two of these three virtues and the ideal of an intense, monoenergetic, flux-normalised high energy photon source remains an unobtained goal. Nonetheless a variety of different techniques have been evolved to produce beams for particular types of experiment.

The three most widely used methods for producing a high energy photon beam are shown schematically in figure 2.1 together with a diagrammatic representation of the microscopic process involved.

The processes are:

- *bremsstrahlung*: $e^- \longrightarrow e^- + \gamma$ fig 2.1 (a): High energy electrons incident on a thin target scatter in the coulomb field of the target nuclei and produce a spectrum of photons peaked sharply in the forward direction.
- *Positron Annihilation in Flight*: $e^+ + e^- \longrightarrow \gamma + \gamma$ fig 2.1 (b): A beam of high energy positrons incident on a thin target produce not only a bremsstrahlung spectrum similar to that produced by electrons but also a spectrum of annihilation photons, again sharply forward peaked.

- *Inverse Compton Scattering*: $e^- + \gamma \longrightarrow e^- + \gamma'$ fig 2.1 (c): An intense monochromatic beam of soft photons produced by a laser may be hardened by backscattering from a high energy electron beam.

Thus all three processes involve an electron-photon scattering process and the spectrum of photons thus produced is continuous in energy. In the cases of positron annihilation and inverse Compton scattering the kinematics of two body scattering allow one to select a limited range of photon energies by collimating the outgoing photon flux. However, in the case of bremsstrahlung, which has been the method most often used in the past, this is not so because it is not possible to select the initial (virtual) photon energy. In fact, the bremsstrahlung photon spectrum has an approximate $1/E$ distribution extending up to the energy of the incident electron. Thus for a given end point energy E_0 the observed reaction yield has the form,

$$Y(E_0) = \int_0^{E_0} \sigma(k_\gamma)\phi(k_\gamma, E_0)dk_\gamma \tag{2.1}$$

This technique is unsuitable for the purposes of many photonuclear experiments since the energy of the photon inducing a particular reaction cannot be identified. However for a reaction leading to an exclusive two body final state such as $D(\gamma, p)n$ the photon energy can be calculated if the proton angle and energy are known. Unfortunately one cannot reject background protons using this method. If the measurement is extended too far below the photon end point then protons produced by higher energy photons via more complex reactions will mimic the signal yield. This is especially troublesome if the end point energy is somewhat higher than the pion production threshold in which case photoproduction recoil protons from the deuterium target itself will contribute to the background as well as the complex nuclei in the material

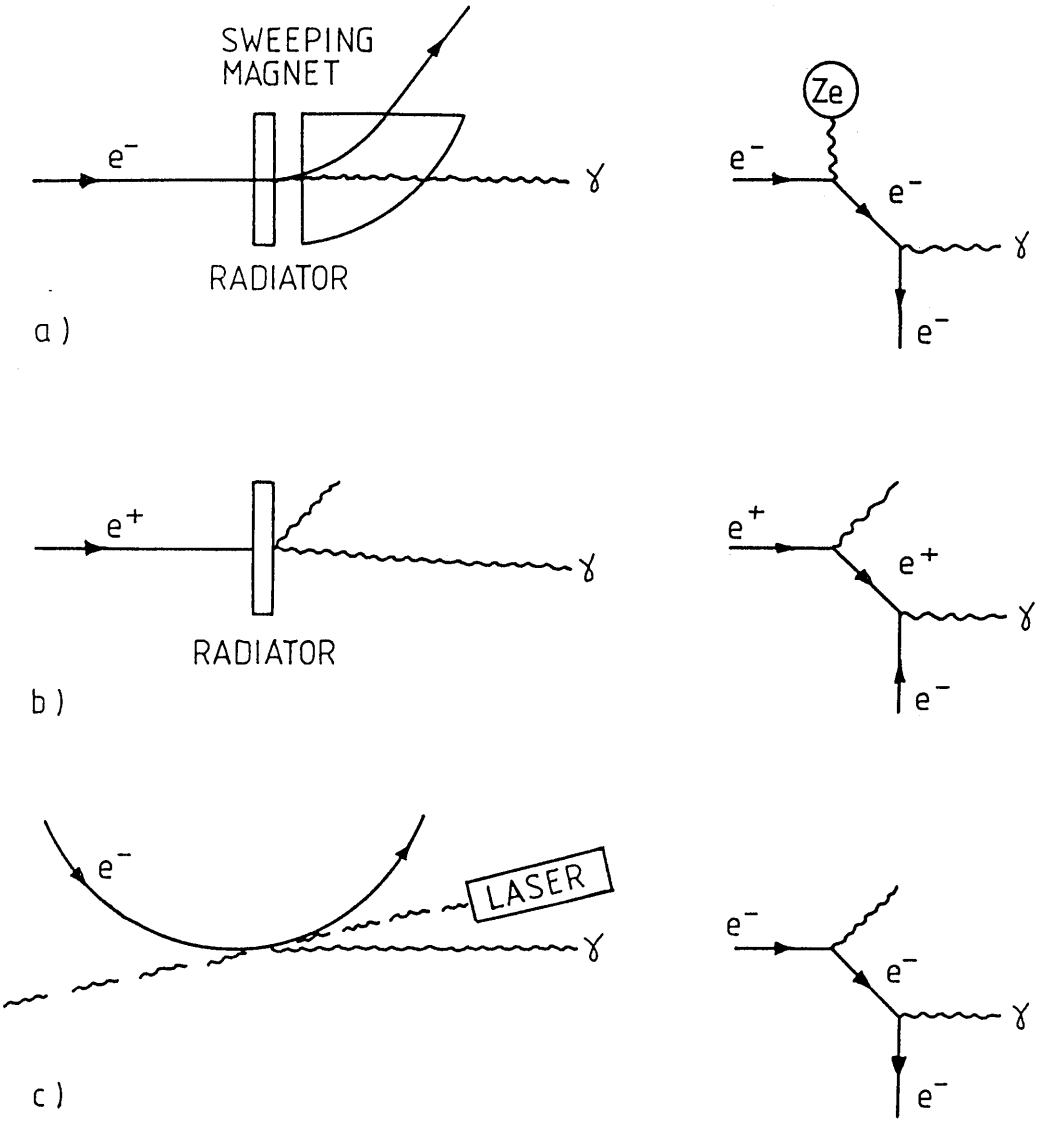

Figure 2.1: *Processes used to produce high energy photon beams:* (b) *Bremsstrahlung,* (b) *Positron Annihilation,* (c) *Compton Scattering.*

surrounding it.

Another potentially serious problem lies in the determination of the photon flux in order to produce normalised cross-sections. With a bremsstrahlung beam one must not only measure the absolute photon intensity but also assume a form for the the energy distribution of the photon spectrum in order to calculate the number of photons in the energy region of interest. The difficulties of determining the efficiencies of photon beam monitors together with theoretical uncertainties in the bremsstrahlung distribution have led to large discrepencies throughout the existing body of photonuclear cross-section data. This is particularly evident in the case of deuteron photodisintegration data (figure 2.3). where the absolute magnitude of the cross-section is of particular importance because detailed theoretical calculations are available for comparison.

2.2 Production of Monoenergetic High Energy Photon Beams

This section describes the means which have been used to produce beams of either quasimonochromatic or identifiable high energy photons. In the first instance, one attempts to produce a beam of photons with an intrinsically narrow energy distribution which then defines the photon energy resolution of the experiment. In the second instance are 'tagging' techniques which rely on the identification of the energy of the individual photons in a continuous distribution on an event by event basis. This latter class of systems has the advantage of automatically producing a beam of known intensity since the flux is determined by the number of photons identified by a tagging coincidence.

2.2.1 Positron annihilation in Flight

The annihilation in flight of a beam of high energy positrons produces a forward peaked cone of energetic photons. The positron flux can be created in the shower produced in a thick, high Z radiator by an electron beam. The positrons may be further accelerated, energy analysed, and directed to a low Z target which produces a high ratio of annihilation photons to bremsstrahlung photons. (Since the cross-sections for the two processes are proportional to Z and Z^2). There is a correspondence between the energy of the photons and their emission angle, and so the annihilation component of the beam may be monochromated by restricting the flux with a small off-axis collimator. The beam energy depends on the mean angle of the collimator and the energy resolution on its size. Two methods have been employed to subtract off the yield from the bremsstrahlung flux which accompanies the annihilation photons.

Firstly, the measurement may be repeated with an electron beam incident upon the annihilation target. The cancellation is not exact because the bremsstrahlung end point shapes are different for positrons and electrons due to differences in the screening corrections. This method has the additional disadvantage that the beam handling system must be changed between measurements to accommodate particles of opposite charge. An alternative method is to make two measurements with radiators of different Z, for example LiH and Cu. The photon spectrum from the Higher Z radiator has a smaller *relative* annihilation component and so it may be subtracted from the low Z spectrum (with appropriate normalisation) to produce a residual annihilation peak. Such a system has been installed at the Saclay linac [31] and up to 10^7 photons per second have been obtained at 50 MeV with 12% resolution. This

has been achieved at a small mean collimator angle (1°) at the expense of a large bremsstrahlung subtraction. The configuration normally used employs a collimator at 4°which reduces the subtraction but limits the available flux to $5 \times 10^3 s^{-1}$.

2.2.2 Inverse Compton Scattering

High energy photons may be obtained from the 180°collision of a high energy electron beam with optical photons from a powerful laser. Tight collimation of the scattered gamma rays produces a beam of well defined energy. A system such as this exists at the ADONE storage ring [32] [33] at Frascati where a CW Argon laser (λ = 488 nm) collides with the 1.5 GeV electron beam producing a $10^7 s^{-1}$ photon beam of energies from 21 to 83 MeV with 9% resolution at 80 MeV .

A significant advantage of this method is that the polarisation of the incident optical photons is preserved in the scattering process and a gamma ray beam of 95% polarisation can be produced.

2.2.3 Bremsstrahlung Photon Tagging

A beam of electrons of energy E_0 passing through a thin foil produces a beam of bremsstrahlung radiation in the forward direction. The beam contains photons of all energies up to the original electron energy. If the residual energy, E_e is measured then the photon energy E_γ is determined through the relation $E_0 = E_\gamma + E_e$. The photon energy may be reconstructed on an event-by-event basis provided that the scattered electron is detected in coincidence with the products of the photon induced reaction. Thus photon tagging provides not

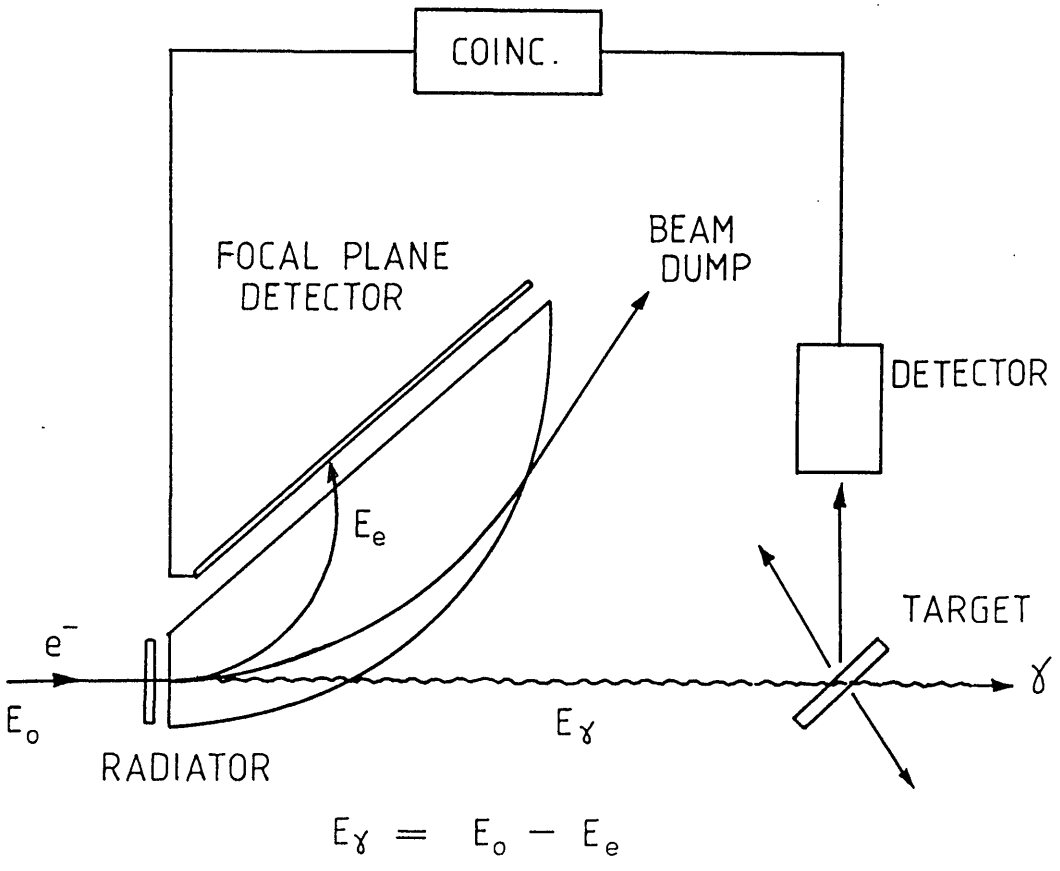

Figure 2.2: *The principle of bremsstrahlung tagging*

a monoenergetic beam but a source of *identifiable* photons. The necessary equipment is shown systematically in figure 2.2. A large momentum acceptance magnetic spectrometer is used to analyse the scattered electrons and to sweep the undeviated main electron beam clear of the photon beam. The scattered electrons are detected in a segmented position sensitive focal plane detector and any coincidence with the detection of a reaction in the photonuclear target is registered.

Knowledge of the photon energy is valuable although not essential for the present measurement $D(\gamma, p)n$. For this purpose the most significant advantage of the tagging technique is the automatic photon flux measurement

accomplished by the electron detection process. The effective photon beam consists only of those photons for which a corresponding tagging electron has been identified in the focal plane array and therefore the absolute flux of the effective photon beam is given by the triggering rate of the focal plane detector. There are however two effects whose correction can introduce uncertainties into the absolute flux determination. The bremsstrahlung beam must be collimated to produce a beam spot of acceptable size at the target. The fact that some photons are eliminated from the beam means that some tagging electrons in the focal plane array no longer correspond to a photon capable of producing a reaction in the target. Other background processes may also produce electron hits in the tagging array for which no photon exists. The measure of these effects is known as the *tagging efficiency*, ϵ_T defined as the ratio of the tagged photon rate to the tagging detector rate. The other important correction is due to the occurrence of accidental coincidences between tagging electrons and events induced by untagged photons. The accidental coincidence rate must be measured during the experiment and a correction made in later analysis. The accidental coincidence rate is dependent on the instantaneous electron rate and so the duty factor of the electron beam is important.

The tagging technique was first proposed by Weil and McDaniel in 1953 [34] and first exploited in the early sixties by workers at the University of Illinois [35] in conjunction with a 25 MeV betatron. Resonance fluorescence measurements were made using three tagging detectors detecting electrons corresponding to 15 MeV photons with a resolution of 100 KeV. The 2 % duty factor of the betatron limited the useful flux to $\sim 2 \times 10^4 s^{-1}$. In 1973 the system was transfered to a microtron with 50 % duty factor, thus increasing

by a factor of 25 the flux available for acceptable real to random coincidence ratio.

In the early seventies tagged photons were utilised in high energy particle physics. An example of this is the system constructed for use with the 5 GeV, 10 % duty factor NINA accelerator at Daresbury . Photoproduction cross-sections on hydrogen were measured over the region 200 MeV to 4 GeV with 10 MeV resolution using a tagged flux of $\sim 2 \times 10^4 s^{-1}$ [36].

An alternative to transporting the beam from the accelerator to a separate tagging spectrometer is to place a very thin bremsstrahlug radiator inside the accelerator and use the accelerator magnet system to analyse the bremsstrahlung scattered electrons. This allows the tagged photon beam to exist parasitically with the main electron beam. The use of a thin wire rather than a foil as the radiator prevents unacceptable disturbance of the beam since it intercepts only a very small fraction of the electrons. Such a scheme was implemented at the Bonn 500 MeV synchrotron [37]. A 20 μm diameter tungsten wire was used as the radiator and an array of 20 plastic scintillators detected the electrons corresponding to 179-347 MeV photons (assuming an incident electron energy of 400 MeV) with a resolution of 1 MeV . A flux of $\sim 10^6 s^{-1}$ with 90% tagging efficiency was obtainable with a real to random coincidence ratio of 10%. This limitation was due to the 5% duty factor of the Bonn synchrotron.

2.2.4 Other Tagging Systems

A similar tagging procedure may be applied to positron annihilation beams [31]. The technique involves the detection of the 'soft' wide angle photon cor-

responding to a 'hard' photon emitted close to the forward direction. The coincidence requirement discriminates between annihilation photons and bremsstrahlung photons. Similar background suppression is possible with inverse Compton scattering sources if the recoil electron is detected. In these two cases the untagged beam is already quite highly monoenergetic, however the flux determination inherent in the tagging process is valuable for many experiments.

2.2.5 Bremsstrahlung Difference Techniques

The bremsstrahlung difference procedure involves measuring two yield curves with bremsstrahlung beams of slightly different energies and then subtracting the yield of the lower energy experiment from that obtained at the higher energy. The difference between the two measurements is due to the photons in the end point region of the higher energy beam whose effects are not cancelled by the subtraction. These photons constitute a nearly monochromatic equivalent photon spectrum. Due to the shape of the bremsstrahlung spectrum the difference spectrum possesses a tail on the low energy side. It is, however, possible to optimise the cancellation of the low energy tail of the spectrum by choosing a suitable relative normalisation constant.

The difference technique may be improved by exploiting the Z dependence of the shape of the bremsstrahlung spectrum near the end point in order to produce a narrower less assymetric photon distribution.[30]. Away from the end point, corresponding to high scattered electron energies, the Z dependence is weak, dependent only on screening and coulomb corrections. In the case of light targets the end point region the spectrum has a stronger Z dependence

due to straggling effects. For high Z targets the energy losses are small but the Z dependence of the bremsstrahlung cross-section itself becomes important. The procedure is to use two radiators of different Z but equivalent thicknesses in radiation lengths and subtract the yield of the higher Z from that of the lower. beryllium and aluminium have been found to be a suitable pair of materials for this purpose.

The reliability of the difference method depends sensitively on assumptions concerning the shape of the bremsstrahlung spectrum in the end point region where the thoeretical uncertainties are largest. Significant effects are known to arise from atomic screening, electron-electron bremsstrahlung and electron straggling in the real, finite thickness radiator. In addition, the method is suited to only a small range of experiments. It cannot easily be applied to multi-arm coincidence measurements and the subtracted excitation spectrum may suffer from large statistical uncertainties at energies below the end point.

However, although its successful use is critically dependent on the reliability of theoretical photon spectra and experimental photon flux measurement techniques, bremsstrahlung has the advantage of being the most intense source of high energy photons available. For example, a 50 MeV , 10 μA beam incident on a high Z radiator of thickness 0.01 radiation lengths will produce $\sim 10^9$ photons per second in the energy region 49-50 MeV .

2.3 A Review of Previous Experiments

A number of previous measurements have explored the energy range of the present experiment. The currently existing data is shown in figures 2.3 and 2.4. The experimental techniques employed are summarised in table 2.1. In

the main these have consisted of (γ, p) experiments performed with bremsstrahlung beams. There are also a small number of recent experiments performed with either monoenergetic photons [46], or equivalently monoenergetic neutrons in the case of the $p(n, D)\gamma$ inverse reaction [47]. Two experiments outwith the energy range of the present measurement have been included in figures 2.3 and 2.4. These are the Mainz 0 °measurement [43] and the Bonn 180 °measurement [44]. The 0 °data extends up to 120 MeV and the 180 °data starts at 180 MeV . The cross-section at these extreme angles is not a strong function of energy and so it is possible to reliably extrapolate the data to the $\sim$ 150MeV region.

2.3.1 Measurements with Bremsstrahlung Beams

The principle of such an experiment is to detect protons emitted from the target at an angle ϑ_p and measure their energies E_p. Assuming that the proton was produced by a deuteron breakup reaction it is possible to calculate the incident photon energy E_γ corresponding to ϑ_p and E_p. This permits the construction of photoproton angular distributions at constant E_γ. In order to transform these measurements into absolute angular differential cross-sections it is necessary to know the total incident photon flux at energy E_γ. The procedure usually adopted has been to measure the total incident flux integrated over all energies in the beam and then to assume that it is distributed according to some theoretical form for the collimated bremsstrahlung spectrum.

The difficulty of performing an experiment of this type is reflected in the inconsistency of the results obtained (see figure 2.3). The most serious problems usually lie in the areas of absolute cross-section normalisation and background

suppression. The absolute photon flux is generally determined by means of a calibrated D.C. beam monitor, usually an ion chamber. This may be a 'thin' transmission device with a low interaction efficiency [40] or alternatively a 'thick walled' chamber with a pair converter several radiation lengths thick on the incoming side [38] [39] [44] [41] [42] [45]. In the former case the electromagnetic shower produced by the photon does not develop beyond the initial pair production process and so the the ionization produced in the chamber is the same for all photons of energies above a few MeV . The chamber is therefore sensitive to the total *number* of photons in the beam, and in the instance of a bremsstrahlung beam its response is dominated by the very numerous low energy photons. (since $\sigma_{brem}(E_\gamma) \sim E_\gamma^{-1}$). A thick walled chamber produces a signal more in proportion to the gamma ray energy, since the convertor thickness may be chosen such that electromagnetic shower develops to the point where the the number of pairs produced reflects the photon energy. The D.C. signal from a thick walled chamber is thus sensitive to the total intensity in the beam (i.e. $E_\gamma \cdot \sigma_{brem}(E_\gamma)$) rather than the total photon flux. This has the advantage of making the signal more dependent on the higher energy photons in the beam.

Given an accurate determination of the beam intensity, it is necessary to assume a model photon spectrum in order to unfold the absolute cross-section differential in energy. The most commonly used formula has been the Schiff form [27] of the Bethe-Heitler Born approximation calculation for thin target bremsstrahlung in the extreme relativistic limit.[28] All the experiments considered have employed a collimated beam, and so the angular differential bremsstrahlung cross-section requires to be integrated over a finite range of photon angles. Since the angular distribution is energy dependent this trun-

cation of the photon distribution may introduce some systematic error into the effective spectrum. The Schiff calculation utilises an exponential atomic potential to simulate screening effects, this is known to be inadequate, especially towards the end point of the spectrum. (i.e. where the energy of the recoil electron is very small) More sophisticated calculations are available, however the theoretical uncertainties remain a serious source of systematic error in a $D(\gamma, p)$ experiment, especially where photons within 10-15 MeV of the bremsstrahlung end point have been used.

In a single-arm (γ, p) bremstrahlung experiment it is not possible to distinguish protons produced by deuteron breakup from those emanating from photodisintegration processes in the target cell walls or the air or vacuum chamber windows surrounding the target. It is possible to correct for this effect by repeating the experiment with an empty target cell, however the background subtraction reduces the statistical accuracy of the experiment. The problem will be especially severe where a D_2O or CD_2 target has been used, since the greater part of the proton yield will be due to oxygen or carbon background which must be separately measured to permit a correction to be made. The foregoing considerations apply equally to a measurement made with a monochromatic beam, however in this case the kinematic constraints result in the signal photoprotons forming a peak in the energy spectrum (for a given ϑ_p) which greatly improves the signal-to-background ratio.

These backgrounds are all caused by interactions in materials other than the actual deuteron target. The experimentalist must design his apparatus in such a way as to minimise such effects, and then perform a 'target empty' measurement to evaluate the corrections. 'Target full' background presents

Reference	experiment	energy [MeV]	quoted errors
[38] Urbana'56	$D(\gamma,p)n$	$60-230$	10% stat.; 10-25% total
[39] Caltech'56	$D(\gamma,p)n$	$105-400$	8% sys.; 5% stat.
[40] Lebedev'58	$D(\gamma,p)n$	$54-148$	15% sys.; 10% stat.
[41] Bonn'67	$D(\gamma,pn)$	$100-420$	5-10% sys.; 3% stat.
[42] Orsay'68	$D(\gamma,p)n$	$100-400$	4% sys.; 2.5% stat.
[43] Mainz'76	0° $D(\gamma,p)n$	$20-120$	3% sys.; 6% stat.
[44] Bonn'83	180° $D(\gamma,p)n$	$180-730$	6% sys.; 6% stat.
[45] Lund'77	$D(\gamma,p)n$	$74-241$	10% sys.; 8% stat.
[46] INFN'86	$D(\gamma,p)n$	$100-255$	5% sys.; 3% stat.
[47] TRIUMF'86	$p(n,D)\gamma$	$E_\gamma \equiv 92,137$	5% sys.;5% stat

	γ beam	target	beam monitor	proton detector
[38]	165-300 MeV Brem	D_2 liquid	quantameter	nucl. emulsion
[39]	300-500 MeV Brem	D_2 gas	quantameter	Al/plastic tel
[40]	265 MeV Brem	D_2O liquid	thin ion.ch.	Al/Argon tel
[41]	450 MeV Brem	D_2 liquid	quantameter	Cu/plastic tel
[42]	Brem (various)	D_2 liquid	quantameter	spectrometer
[43]	110-160 MeV Brem	CD_2	compton spect.	spectrometer
[44]	330-850 MeV Brem	D_2 liquid	quantameter	spectrometer
[45]	Brem (various)	D_2 liquid	quantameter	Al/plastic tel
[46]	e^+ annihilation	D_2 liquid	pair spect.	NaI/plastic tel
[47]	–	H_2 liquid	$p(n,p)n$	plastic tel/TOF

Table 2.1: *Previous Measurements of Deuteron Photodisintegration*

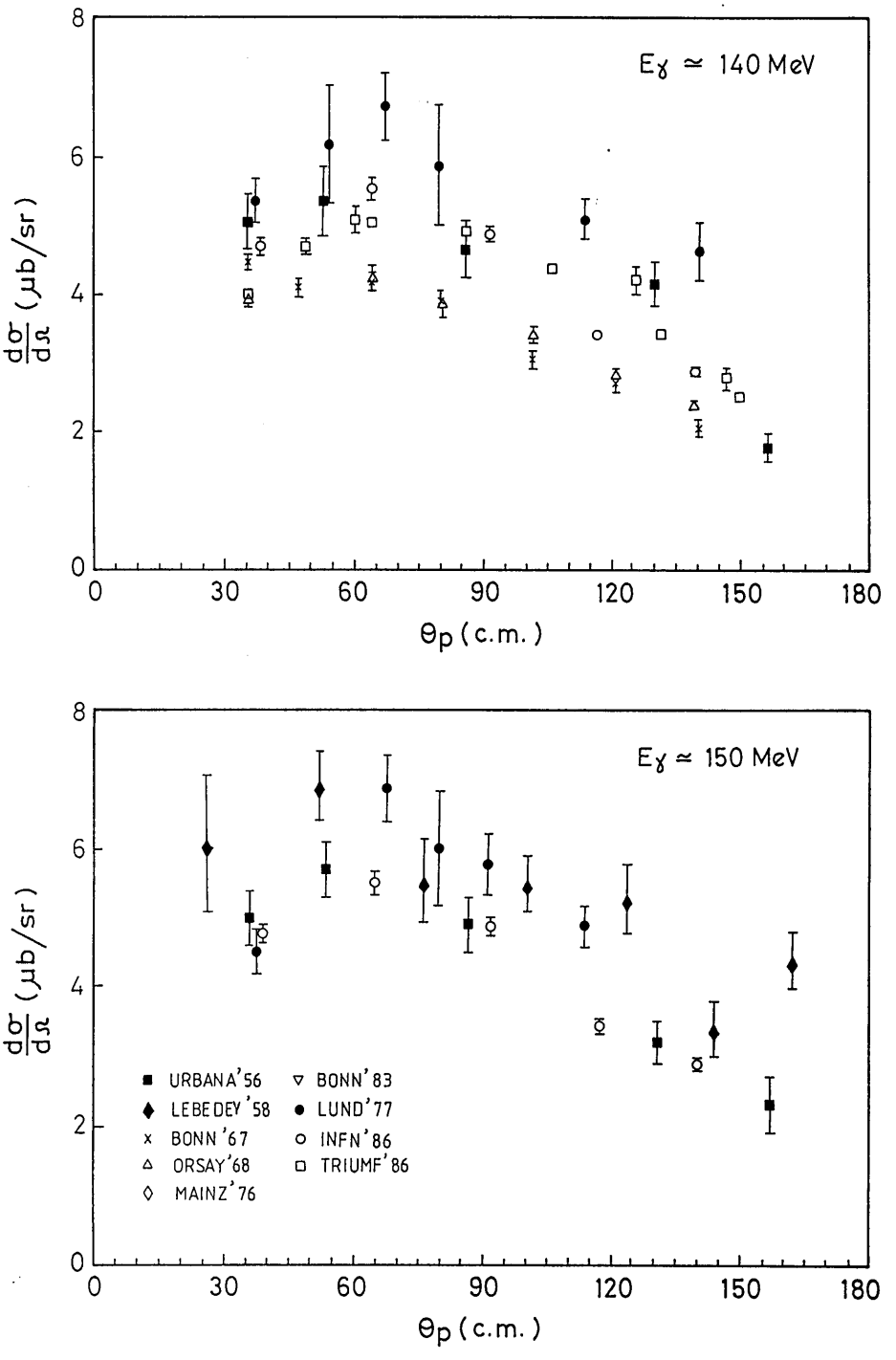

Figure 2.3: *Previously measured angular differential cross-sections for deuteron photodisintegration: data referenced in table 2.1*

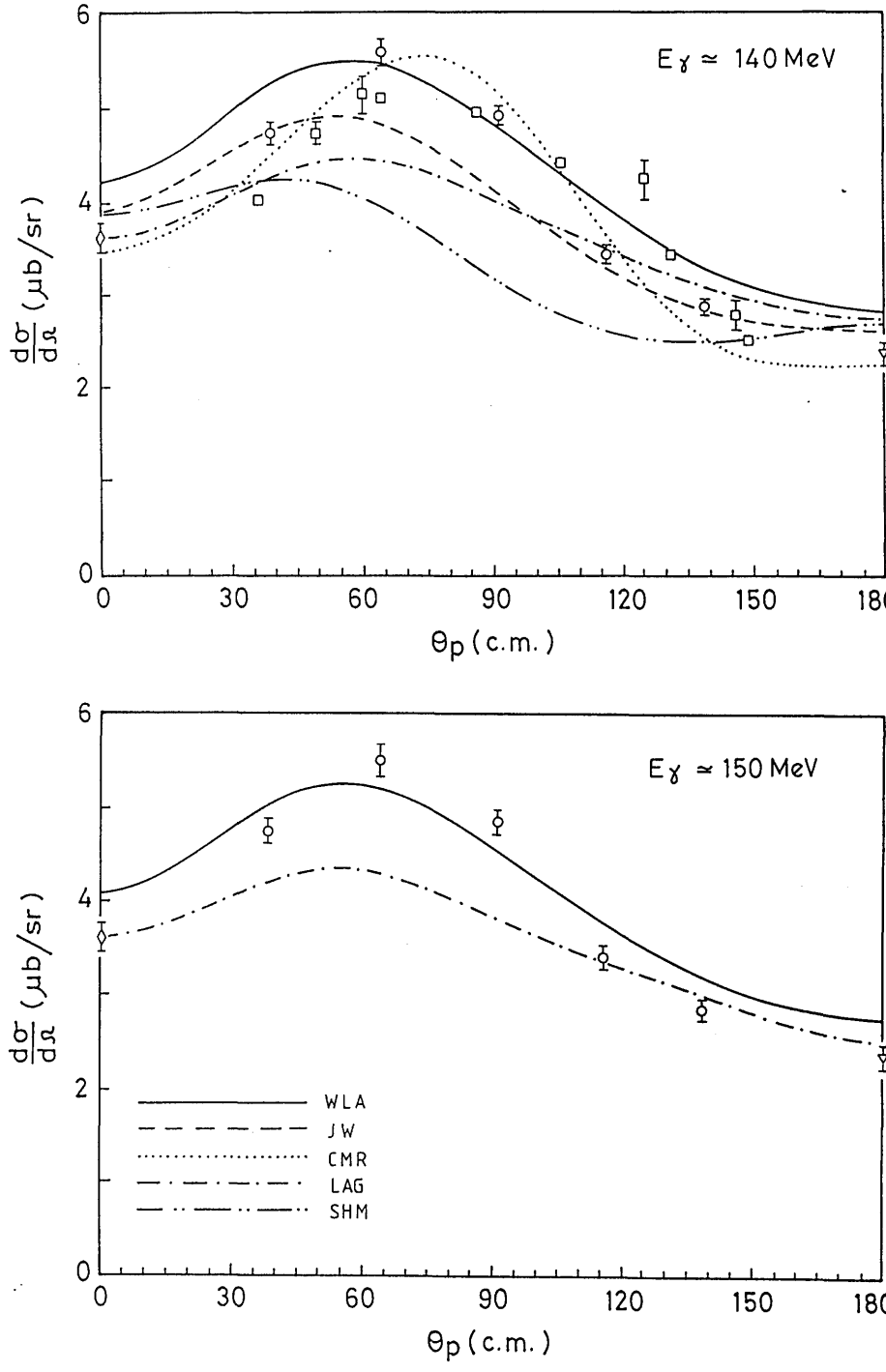

Figure 2.4: *Selected angular differential cross-section data on deuteron photodisintegration: data referenced in table 2.1*
Theory references: WLA [70]; JW [21]; CMR [69]; LAG [68]; SHM [71]

a more complicated problem. Electrons from the target can be identified, usually by differential energy loss, and vetoed. In experiments where the end point energy is sufficiently high there will also be a proton background from pion photoproduction processes. For example, photons of several hundred MeV will produce recoil protons from $D(\gamma,p)n\pi^0$ and $D(\gamma,p)p\pi^-$ reactions which are similar in energy to those produced by photons of $\sim$ 100 MeV via $D(\gamma,p)n$ reactions. Such effects are exacerbated in the energy range of the current experiment by the large pion production cross-section in the region of the Δ-resonance. However for a given end point energy and fixed proton angle and energy there exists a limiting photon energy above which two-body photodisintegration is the only possible process. The contribution from photoproduction recoils can therefore be eliminated by adjusting the the end point energy to correspond with the angle and energy acceptance of the proton detector. There remains, however, the possibility of secondary proton production by pions in the detectors and the collimators. An alternative method of suppressing competing reactions is to detect the outgoing proton and neutron in coincidence. This is the approach adopted in reference [41]. It has the disadvantages of requiring an accurate knowledge of the neutron detector efficiency and, of course, of reducing the counting rate.

The design of the target is also influenced by the need for accurate normalisation and efficient background suppression. Most of the experiments considered here have used either deuterium liquid or gas cells as targets. Liquid targets usually provide higher densities, and therefore higher counting rates, but are prone to boiling, which may reduce the mean density of the liquid by an amount which is significant but hard to quantify. The density of a gas target is easier to determine and low temperatures and high pressures

have been used to maximise the target thickness, e.g. reference [39] where the cell was operated at 2000 p.s.i. and 77.4°K. Nevertheless, the ratio of target thickness to window thickness is generally poorer for a gas target as compared to a liquid target. The countermeasure adopted in [39] was to employ a very long gas cell and collimate the proton detector in such a way that only protons originating from a restricted region in the middle of the cell can be detected. This eliminates background from the cell walls at the expense of a rather complicated acceptance calculation.

A variety of proton detection techniques have been used in the experiments under review. These have included magnetic spectrometers [42] [43], nuclear emulsions [38], NaI scintillators and telescopes consisting of alternate absorbers and scintillators or proportional counters [40] [45] [41] [39].

If the detected proton energy is used to reconstruct the incident photon energy then the selected proton energy range determines the effective photon energy range. Any uncertainty in the proton detector response function results directly in a corresponding photon flux uncertainty. The experiments which used magnetic spectrometers have more than adequate energy resolution, though this may not be the case for those using absorber telescopes. These rely critically on range-energy data to define the lower and upper limits of an accepted energy interval in which protons are sufficiently energetic to pass through the first absorber and trigger a transmission detector but have insufficient energy to pass through a further absorber, thus failing to trigger an anticoincidence detector. The exact energy interval depends on the relative stopping power of the absorber and detector material, on straggling effects and on the detector thresholds.

The spread of results observed in figure 2.3 places in doubt the reliability of all of the previous bremsstrahlung measurements. The results of individual experiments may also have been affected by other factors. For example the technical limitations of the Lund synchrotron forced the authors of [45] to use rather high end point energies (> 375 MeV) and therefore this experiment, whose results are systematically the highest in the sample, may have been more prone to contamination by recoil protons from photoproduction reactions. On the other hand the Bonn measurement [41], whose cross-section data is the lowest in the sample, involved detecting neutrons and protons in coincidence and may have suffered from an ill determined neutron detector efficiency calibration.

2.3.2 Measurements with Monoenergetic Photons

The conclusion drawn from the experience with bremsstrahlung measurements is that any significant increase in the accuracy of the experimental results would require major improvements in the techniques employed. Specific requirements are more accurate overall normalisation and a monoenergetic beam to allow background rejection by means of the reaction kinematics. The recent experimental work in which attempts have been made to remedy these deficiencies is shown in figure 2.4 . Also shown for comparison in figure 2.4 are a selection of recent theoretical predictions of the photodisintegration cross-section.

A recent experiment at INFN Frascati [46] used a quasimonochromatic e^+ annihilation beam. Rather than subtract off the positron bremsstrahlung contribution they chose to analyse it in the conventional manner. Therefore

the photon spectum was 'high energy enhanced' rather than monoenergetic. The advantage of this method, however, was that it allowed comparisons to be made between bremsstrahlung tail measurements made at one positron energy and annihilation peak data taken at another. The beam power was measured with a quantameter as before, but the combined annihilation plus bremsstrahlung photon spectrum was simultaneously measured by means of a pair spectrometer. The spectrum was checked by means of a Monte Carlo calculation, as was the response of the NaI/plastic proton telescope. The possibility of accurate numerical simulations on modern computers represents another advance upon the technology available to the earlier workers.

The use of a monoenergetic particle beam to study the $p\ n$ capture reaction is equivalent to the use of a monochromatic photon beam in a photodisintegration experiment in the assumption that the $\gamma D \rightarrow pn$ reaction is related to the time reversed reaction $pn \rightarrow D\gamma$ through the principle of detailed balance. The procedure adopted in measurements at TRIUMF [47] has been to use a neutron beam and a liquid hydrogen target and to detect the recoil deuterons in a plastic scintillator telescope. Normalisation is achieved by simultaneously measuring the elastic $p(n,p)n$ reaction for which the cross-section is well established.

The error bars shown on figure 2.4 are due to the statistical uncertainties only. The additional systematic uncertainty quoted for both of the above experiments is 5 %. The observed scatter of the data points in figure 2.4 suggests that the errors may be underestimated.

2.4 The Design of a D(γ,p)n Measurement with Tagged Photons

This section is a commentary on the design of the present experiment in the light of the physics objectives and the resources and facilities available.

The experimental work was conducted using the Glasgow tagged photon spectrometer [48] at the Institut für Kernphysik, Johannes Gutenberg Universität, Mainz using the 180 MeV DC electron beam produced by the racetrack Microtron MAMI-A [49] [50]. The present experiment is one of a series of (γ, p) and (γ, pn) measurements which have been performed on light nuclei using a large solid-angle plastic scintillator charged particle telescope and a complementary array of time-of-flight neutron spectrometers.

The physics interest in the deuteron photodisintegration process has been discussed in chapter 1. A significant amount of theoretical effort has been recently expended in the understanding of this process in the energy range around the pion threshold. There remain, however, significant discrepencies between the calculations of different groups.Furthermore the available modern data in the region $E_\gamma \sim 150$ MeV , although qualitatively supporting the general trend of the theory, is rather scattered in its angular distribution.

The energy region chosen for the present measurement was limited by the 2:1 momentum acceptance of the tagging spectrometer. The normal electron beam energy supplied by MAMI-A is 183 MeV . Therefore a chosen recoil electron momentum range of $25 - 50$ MeV/c corresponds to a tagged photon range $E_\gamma = 133 - 158$ MeV .

In order to contribute significantly to the resolution of the uncertainty in

the $D(\gamma,p)n$ cross-section a total uncertainty of $\sim$ 5 %, including both statistical and systematic effects is required. The measured angular distribution must cover as wide an angular range as possible, with enough data points to map the angular variation in detail. The possibility of reliable extrapolation to 0° would be valuable to complement previous theoretical effort on the forward cross-section. A wide angular range is also necessary if the data is to be parameterised in terms of orthogonal functions [51] for more quantitative comparison with calculations and other data, since such a parameterisation is only unique if the fit is weighted evenly over 0°- 180°. The eventual choice was 30°to 150°in the centre-of-mass system, the access to the extreme forward and backward angles being limited by detector geometry and the sharply rising electromagnetic background at small angles.

Having chosen an angle-energy range which is both feasible and desirable the next question is the required size of angle-energy increment. The present experiment involves the simultaneous measurement of a wide, continuous range of angles and energies which may be subdivided according to choice in the later analysis. However it is necessary to specify the eventual size of angle-energy bin in order to estimate the luminosity necessary for the experiment. Taking into account the rapidity of variation of the cross-section and the available beam-flux and detection solid angle it was decided to standardize on a nominal 10°, 10 MeV angle-energy bin.

In order to achieve the desired overall accuracy it was estimated that an uncertainty of not more than 3 % after subtractions for each angle-energy bin would be required. Given the available beam flux, this necessitates the use of a thick target with a high forground to background ratio. For this

reason a liquid deuterium target with thin kapton windows was used. This is in contrast to targets of the high pressure gas type which have been used with untagged bremsstrahlung beams (refs) where very much higher photon fluxes are available. (10^{13} s^{-1} vs. 10^{7} s^{-1}). The small signal yield from such a target make it unsuitable for use with a tagged photon beam.

In order to determine the kinematics of the reaction it is necessary to measure only the proton energy E_p and emission angle ϑ_p. However, if the photon energy E_γ is also known, as is the case in a tagged photon measurement, then the kinematic conditions of the reaction are overdefined and it is possible to compare the proton energy *calculated* from E_γ and θ_p with the assumption of deuteron kinematics and the measured energy signal. This procedure (see chapter 5) produces a locus in phase space for the deuteron events, separate from the bulk of the background produced by target cell windows, untagged random coincidences etc. The only inputs required are the relatively well known tagged photon energy and proton emission angle.

The problem of normalisation separates into two parts. In the first place, there is the question of run-to-run normalisation between measurements at different angles and energies in order to construct a consistent angular distribution and excitation function. Secondly, there is the problem of the global, absolute normalisation of the total data set in order to turn the data into a double differential cross-section $\frac{d^2\sigma}{dE_\gamma d\Omega_p}$.

With regard to the relative normalisation the design of the present experiment possesses the considerable advantage that a wide range of angles and energies are measured simultaneously, eliminating the effects of beam flux or target density variation with time. The proton telescope covers an angular

range of $\sim$ 70 °and so must be moved twice to measure the total angular distribution, however there are large angular overlaps between the different detector configurations used for each part of the angular distribution providing a consistency check between measurements taken at different times.

Reliable absolute normalisation is of particular importance in this experiment since several theoretical treatments of the cross-section differ principally in magnitude, having similar angular variations, at least at angles other than those at the extreme forward and backward directions. The lack of consistency in normalisation is the major flaw of the previously existing data.

The advantage of photon tagging over other methods of producing monochromatic photon beams lies in the area of absolute beam flux determination. The recoil electrons corresponding to the tagged photons are counted on free-running scalers and this count rate *defines* the useful photon flux. There are of course corrections to be made for random coincidences of a tagging electron and an event trigger produced by an untagged photon, and also, as the beam rate increases, other corrections due to multi-electron coincidences with 'real' events. Prescriptions have been developed for the application of these corrections but it is important that the corrections are reasonably small so that uncertainties in their treatment do not greatly affect the final results. In the case of the present experiment this puts a limitation on the maximum usable beam flux of about $10^7 s^{-1}$.

Chapter 3

The Experimental System

3.1 The Mainz Microtron MAMI

The schematic layout of a microtron is shown in figure 3.1. It consists of a dipole magnet between whose poles is situated an electron source and a radio-frequency accelerating cavity. The electrons circulate in the magnetic field in circular orbits with a common tangent passing through the r.f. cavity. The radius of the orbit increases uniformly with each pass through the accelerating structure. A modification of this accelerating system is shown in figure 3.2. In this system a high duty cycle linear accelerating section is placed between two separate dipole magnets. Because of the shape of the electron trajectories such a device is known as a racetrack microtron. This design presents several advantages in the area of beam handling and control. The return paths opposite the accelerating section are well separated and may be individually steered by means of transverse deflection coils. A separate deflection magnet may be used to facilitate beam extraction as shown in figure 3.2.

The MAMI project [49] [50] at the Mainz Institut für Kernphysik has the eventual objective of producing a 100 μA, 100 % duty factor electron beam at 840 MeV . The type of machine chosen is a racetrack microtron (RTM) with a continuous wave (C.W.), room temperature r.f. accelerating structure. This design has several advantageous properties. The C.W. accelerating structure provides 100 % duty factor with no transient beam loading problems, and the technology required for the construction and operation of a room temperature system is cheaper and better understood than for a superconducting accelerator.

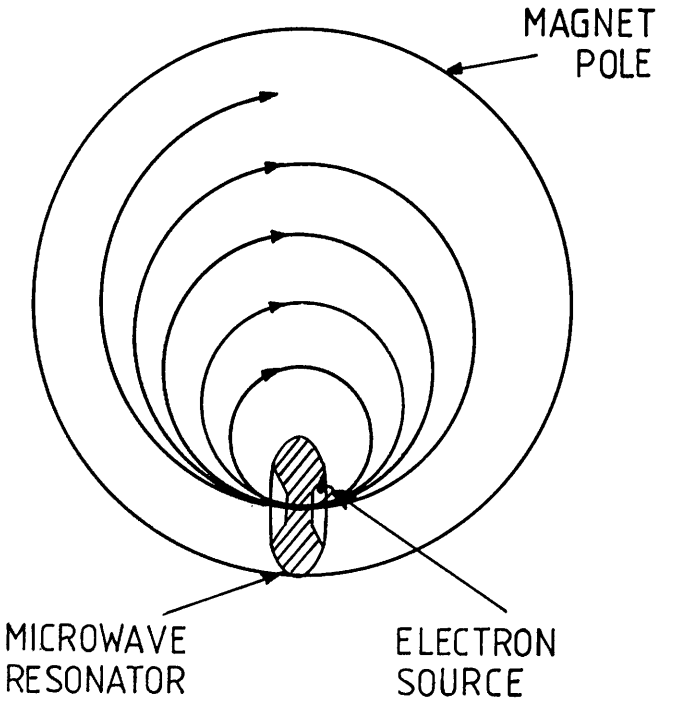

Figure 3.1: *Schematic design of a microtron*

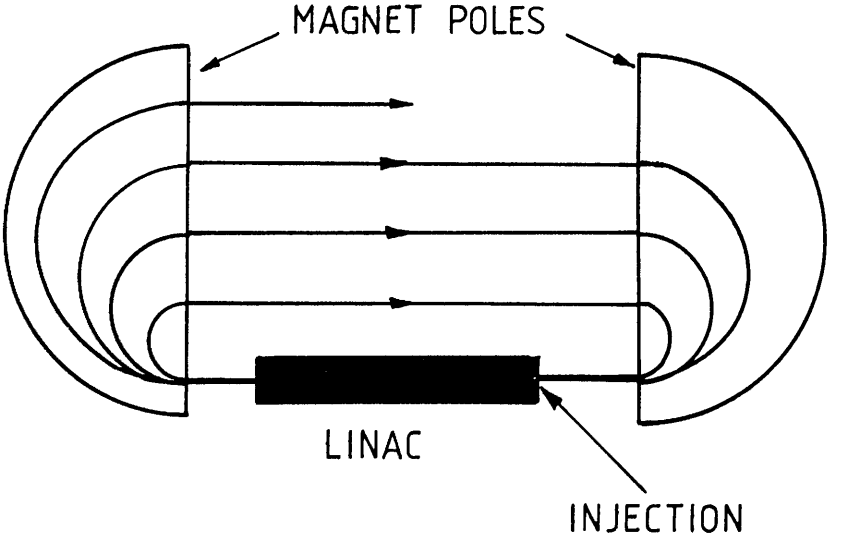

Figure 3.2: *Schematic design of a racetrack microtron*

The basic design of an RTM is constrained by the following expression,

$$2.096\Delta T = \nu\lambda B \tag{3.1}$$

where:

ΔT = energy gain in linac

λ = vacuum r.f. wavelength

B = magnetic field strength in tesla

ν = number of wavelengths by which orbit circumference increases in one orbit.

A small ΔT is required for the sake of r.f. power economy. However $\nu\lambda$ is fixed by the relation $\nu\lambda = d\pi$ where d, the return path spacing, should be of the order of $\sim$ 4 cm in order that the individual return paths may be steered independently by separate coils. Furthermore B cannot be made arbitrarily small since the necessary pole face area would become uneconomically large.

It has been found that the energy increase practicably obtainable in an RTM is limited to factor $\sim$ 10. Thus an 840 MeV machine requires at least 3 stages in cascade. Below $\sim$ 2 MeV RTM operation is impractical due to variation in the electron velocity with increasing energy. Therefore preacceleration to 2-3 MeV is necessary. The eventual solution chosen for the MAMI microtron is detailed in table 3.1. The system will eventually operate with a 3.5 MeV Linac as injector. At present only the first two stages of the system have been installed, providing a beam of 180 MeV energy, and the preacceleration is performed using a 2.1 MeV Van de Graaffaccelerator. Otherwise the machine parameters are as presented in the table. Figure 3.3 shows the present layout of the accelerator system.

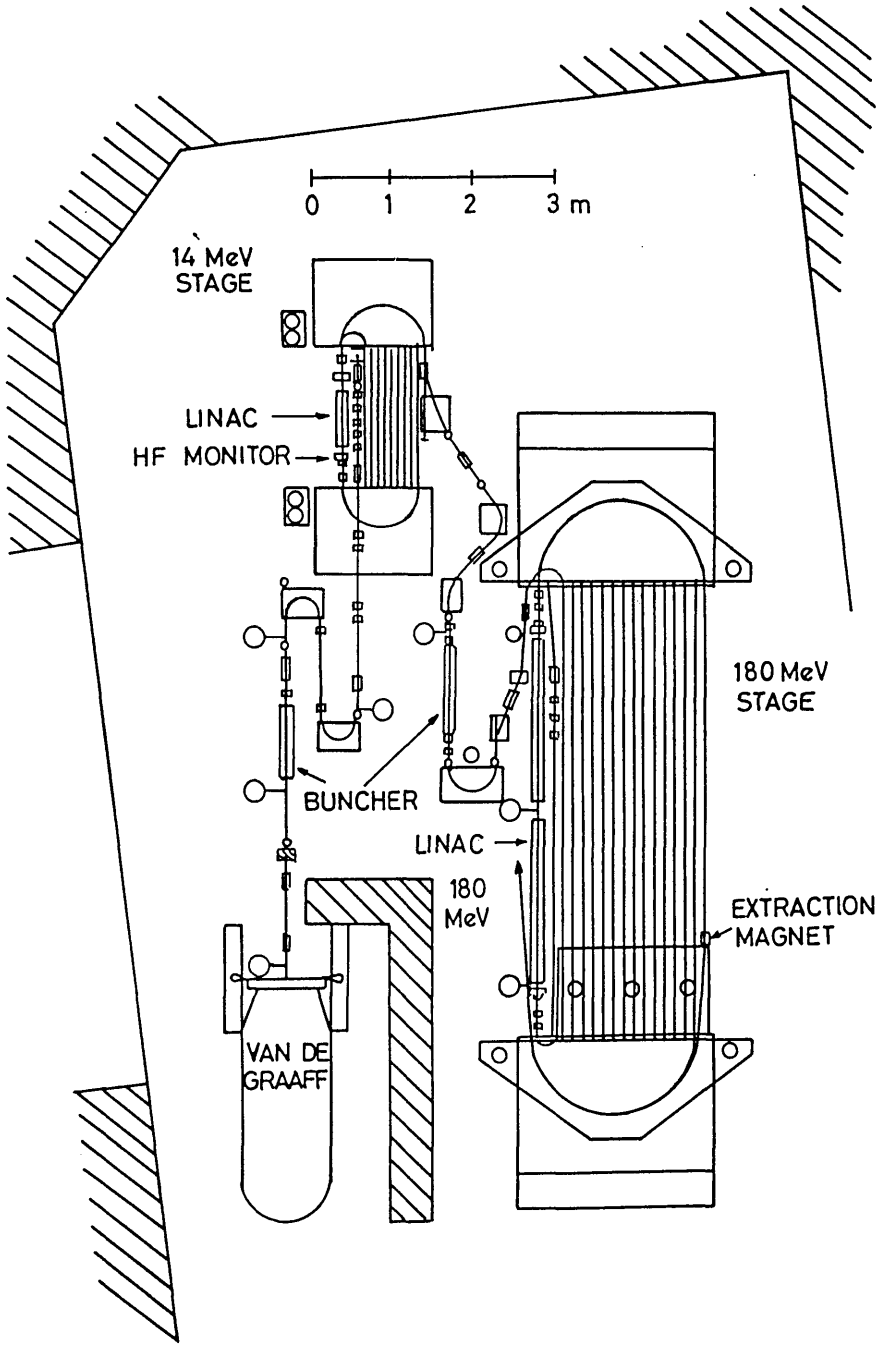

Figure 3.3: *The Mainz microtron MAMI-A*

		Stage 1	Stage 2	Stage 3
Basic Parameters				
Overall length	[m]	3.8	9.5	20.2
Injection Energy	[MeV]	3.5	14	180
Extraction Energy	[MeV]	14	180	840
Number of Orbits		20	51	88
Magnet System				
Field Strength	[Tesla]	0.10	0.56	1.28
Pole Face Diameter	[m]	1.5	2.5	5.0
Weight	[t]	1	43	450

Table 3.1: *Parameters of MAMI*

Operation and performance

The microtron is controlled via a dedicated HP1000 computer. The task of optimising the beam trajectory through the microtron system is achieved by means of an automatic iterative process using passive r.f. monitors and steering coils on the individual beam return paths. During beam setup the injector is operated in a pulsed mode and 12 ns long beam pulses are tracked through the accelerator system at a frequency of 10 kHz.

The final beam has a measured resolution of 30 KeV at 183 MeV with emittance 0.09 π mm mrad horizontally and 0.04 π mm mrad vertically. In comparison with the best performance of a LINAC of similar energy this

represents an improvement in energy resolution of a factor of 10 and a factor of 50-100 improvement in emittance. The duty cycle of the machine is of course 100 %. This again compares very favourably with the best figure achievable with a conventional LINAC which is of the order of 1-2 %.

3.2 The Tagged Photon Spectrometer

This section describes the tagging spectrometer installed by the Glasgow-Edinburgh-Mainz collaboration in the beam of the microtron MAMI-A at the Mainz Institut für Kernphysik [48]

The system is designed with the possibility of parasitic operation in mind. In a parasitic configuration a thin wire, intercepting only a small fraction of the electron beam, is used as a radiator. The almost entirely undisturbed electron beam is then transported downstream to another user. Thus the magnetic elements of the spectrometer through which the main beam passes must be treated as an integral part of the beamline. Under normal operating conditions the electron beam is less than 3 mm in diameter at the radiator and remains less than 9 mm at all points along the beamline. Even when not operated in parasitic mode this has the advantage that the beam may be transported away from the experimental area in a controlled manner and dumped sufficiently far away to avoid creating extra background.

3.2.1 The Magnet System

The magnet system divides functionally into two parts. One task is to collect and analyse the bremsstrahlung scattered electrons. The other function is to transport the undeviated beam away from the experimental area. In the

present design this functional separation is reflected in the physical arrangement of the magnetic elements. The overall design specification of the magnet system was as follows.

- The Spectrometer
  - Large momentum acceptance ($p_{max} : p_{min} = 2{:}1$)
  - Large angular acceptance for electrons within the momentum range analysed.
  - Energy resolution $(\frac{\Delta p}{p}) \lesssim 10^{-3}$
  - The system should be sufficiently compact so that the target is not so far from the radiator that the beam spot is too large. (The beam spot size may be reduced by tighter collimation but only at the expense of a poorer tagging efficiency.)
- The Beam Handling System
  - Large angular acceptance for electrons elastically scattered in the radiator.
  - Fixed output geometry independent of the magnet settings in the spectrometer.

The plan of the tagging system is shown in figure 3.4. The spectrometer system consists of 3 elements in a QDD configuration, labelled QS1,DS1 and DS2 in the figure. The magnetic fields in DS1 and DS2 are arranged so that the incident electrons of energy E_0 pass through only DS1. DS2 analyses the scattered electrons in a 2:1 momentum range. Changing the spectrometer field settings alters the output trajectory of the main beam from DS1. The

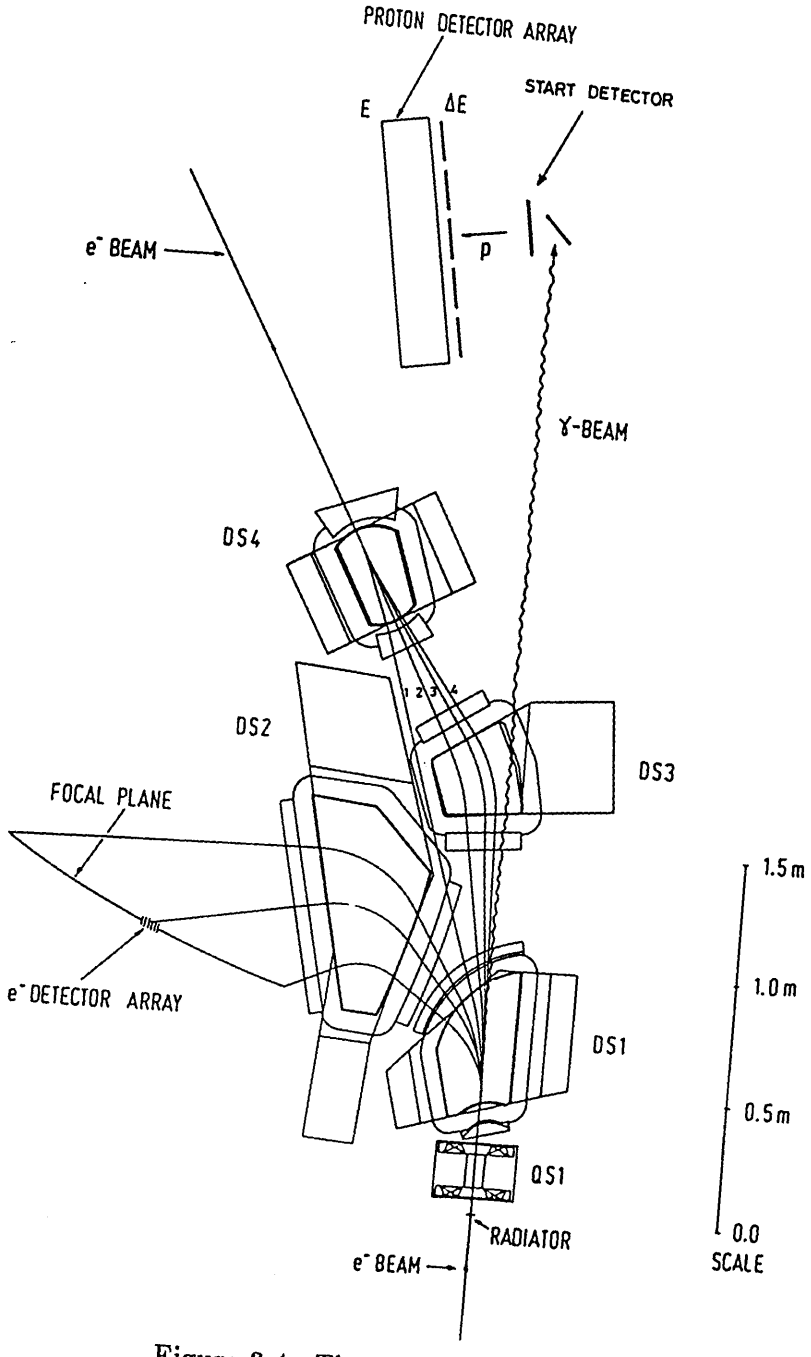

Figure 3.4: *The tagged photon spectrometer*

four standard range settings correspond to different main beam trajectories which vary by 18°on exit from DS1. A common output trajectory for the beam is produced by the combined effect of DS3 and DS4. The standard range settings for a 180 MeV beam are shown in table 3.2.

Trajectory	E_{max}	E_{min}	$k_{\gamma\ min}$	$k_{\gamma\ max}$
1	100	50	80	130
2	50	25	130	150
3	25	12.5	155	167.5
4	12.5	6.25	167.5	173.75

Table 3.2: *Tagging spectrometer energy ranges for an incident electron beam energy of 180* MeV . *All energies are in* MeV .

3.2.2 The Focal Plane Detector Array

In order to observe the tagging electron-photon coincidence, a position sensitive detector is required in the focal plane of the spectrometer which provides energy and timing information with a resolution comparable to that of the experimental apparatus with which it is to be used.

The requirements are:

- $>$ 99 % efficiency for electrons passing through the focal plane to complement the high acceptance for electrons traversing the spectrometer.
- Timing resolution of $\sim$ 1 ns.

- Spatial resolution corresponding to $\Delta E \lesssim 1$ MeV .
- Background rejection via a coincidence requirement.
- Reliable operation and long lifetime at high counting rates. (The tagging electron rate is $\gtrsim 10^7 s^{-1}$)

The system chosen is an array of plastic scintillators shown schematically in figure 3.5. The focal plane is slightly curved, 1.33 m long, and the electrons pass through it at angles of between 35° and 41° with respect to the local normal direction. Figure 3.6 shows the arrangement of the scintillators. There are 92 detectors, each $60 \times 17 \times 2$ mm^3. Each strip overlaps the next by 0.5 mm more than half width. A coincidence requirement between adjacent channels identifies an ionising particle and reduces the sensitivity of the system to γ and neutron background. The thickness of the scintillators is a compromise between light output on one hand and scattering effects and background sensitivity on the other. The 2 mm thickness corresponds to a 1° mean angular divergence due to multiple scattering and a mean energy deposition of 300 KeV for minimum ionising electrons, which is equivalent to 1.5×10^3 scintillation photons for a typical plastic scintillator. Nuclear Enterprises' Pilot U scintillator was used for optimum timing resolution and Hamamatsu R1450 photomultipliers were chosen for their good lifetime and timing specification.

3.2.3 The Bremsstrahlung Radiator

For a given photon beam flux the choice of an ideal radiator thickness is dependent on the relative importance of various sources of background radiation under the particular conditions of the experiment. A radiator which is thin

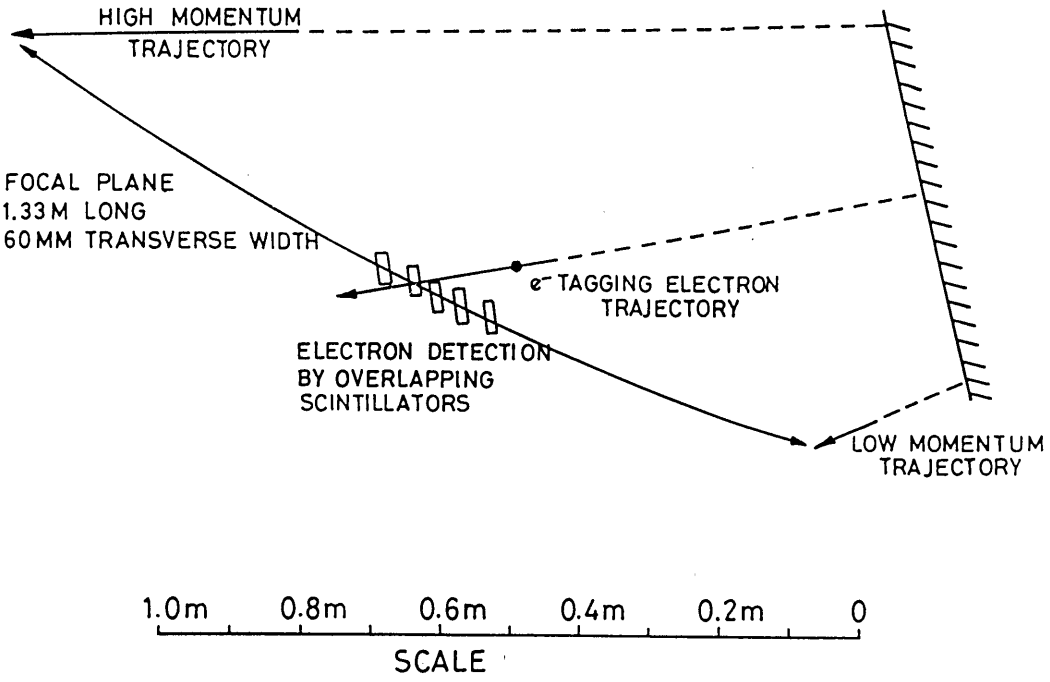

Figure 3.5: *The spectrometer focal plane*

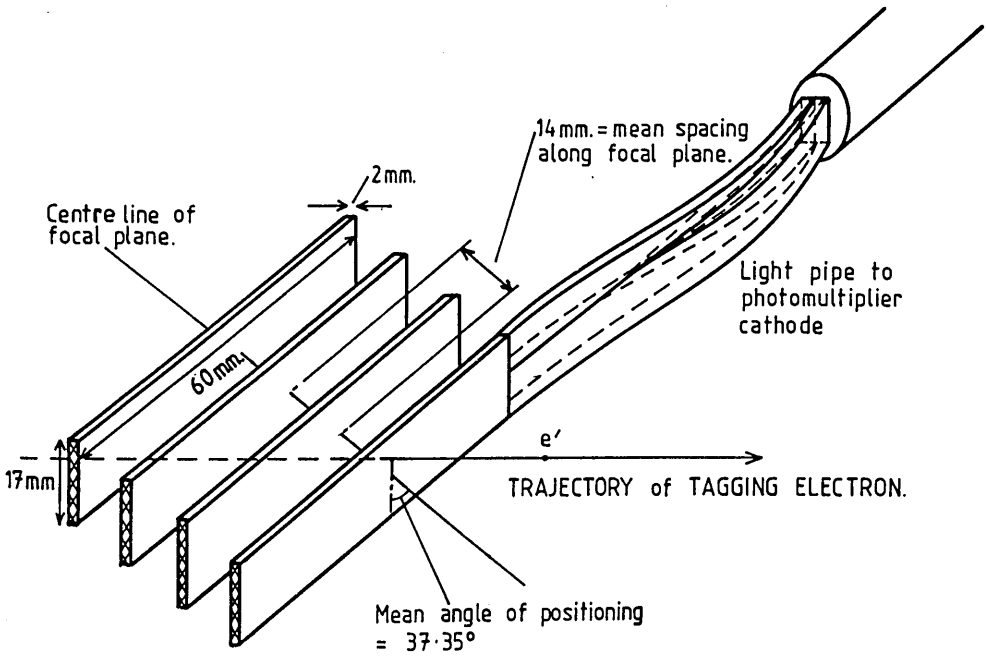

Figure 3.6: *Arrangement of detectors on the focal plane*

(in terms of radiation lengths) requires the use of a higher electron beam current and thus the creation of more background from the beam stop. A thicker radiator requires a lower current to produce the same photon flux but the electron beam will suffer more small-angle multiple scattering in the radiator and thus degraded it will produce more background in the beamhandling system as it is transported away from the experimental area. Trials under normal experimental conditions at Mainz lead to the adoption of a 25 μm aluminium foil ($\equiv 2.8 \times 10^{-3}$ radiation lengths) as the standard radiator.

It is convenient to have an automated system for removing and replacing the bremsstrahlung radiator, for interchanging different radiators and for introducing crosswires and fluorescent screens when adjusting the beam transport system. If a fine wire radiator is to be used instead of a foil (section 2.1.5) then the automated movement must be accurately reproducible. The system used for the present experiment consists of wheel rotating about an axis parallel to the beam axis. The wheel has 16 equidistant mounting positions spaced about the circumference. These contain radiator foils of varying materials and thicknesses, an alignment cross-wire, a Zn S coated fluorescent screen and an empty position which allows unimpeded passage of the electron beam. The wheel is rotated by a stepper motor, stepping in 8000 increments per revolution, corresponding to lateral movements of ± 0.15 mm on the beam axis.

3.2.4 The Photon Beam Collimator

The bremsstrahlung beam must be collimated in order to produce a beam spot of acceptable diameter at the target position. For the purposes of this

experiment the beam diameter at the target was restricted to 4 cm. The beam, which diverges from what is effectively a point source on the radiator, is restricted to a cone of half angle 4.46 mrad by a tapered tungsten alloy collimator 15 cm deep (40 radiation lengths) . This process alone cannot produce an entirely 'clean' beam however, there remains a penumbra of scattered photons and photoproduced e^+e^- pairs surrounding the main beam. A 0.4 tesla permanent magnet placed directly in front of the collimator serves to sweep the charged particles out of the beam and then the beam is passed through a lead collimator of slightly larger diameter, sufficiently large to allow passage of the main beam while still intercepting the halo. The scattering produced by the second collimator is of negligible intensity. Tests with a thin plastic scintillator detector have shown that the boundary of the beam is defined to within $\pm$ 1 mm after collimation.

It follows from the use of a collimator that the focal plane detector will register tagging electrons for which there is no corresponding photon in the beam. Since the beam normalisation is obtained by integrating the ladder signals it is necessary to introduce a correction factor to compensate for this *tagging efficiency* effect. The procedure by which the tagging efficiency is measured will be described in the section on normalisation procedures.

3.3 The Proton Detector System

3.3.1 General Design

The present experiment is one of a series of (γ, p) and (γ, pn) measurements undertaken by the Glasgow-Mainz collaboration. In view of the available tagged photon fluxes and the magnitude of the photonuclear cross-sections to

be investigated it was necessary to construct a large solid angle charged particle detection system. The design specification of the system was as follows:

- $\sim$ few MeV energy resolution for protons of energies 25 - 150 MeV .
- Angular resolution $\sim 5°$ or better.
- Solid angle in the range 0.5 - 1.0 sr.
- Timing resolution $\sim$ 2 ns.
- $\frac{dE}{dx}$ discrimination between protons, deuterons and electrons.
- Low background rates from neutral or low energy charged particles via a detection coincidence requirement between several detector elements.

The arrangement of detectors is shown in figure 3.7 . The system consists of 3 sets of plastic scintillators, two thin transmission elements (ΔE detectors) and a stopping detector (E detector)

Each bank of detectors consists of a series of parallel strips or blocks of scintillator. Position information along the length of the strip is obtained from the difference in arrival times of signals detected by the photomultipliers at either end. The combination of horizontal E segments and vertical ΔE strips fixes the point of incidence of particles upon the plane of the detector. This technique has been described previously in references [52] [53] [54] [55].

Detector ΔE_2 is placed close to the target and, when operated in coincidence with ΔE_1 and E serves to collimate the flux of particles incident on the rear elements restricting its source to the region of the target since there is no line-of-sight through the three banks of scintillators from the photon

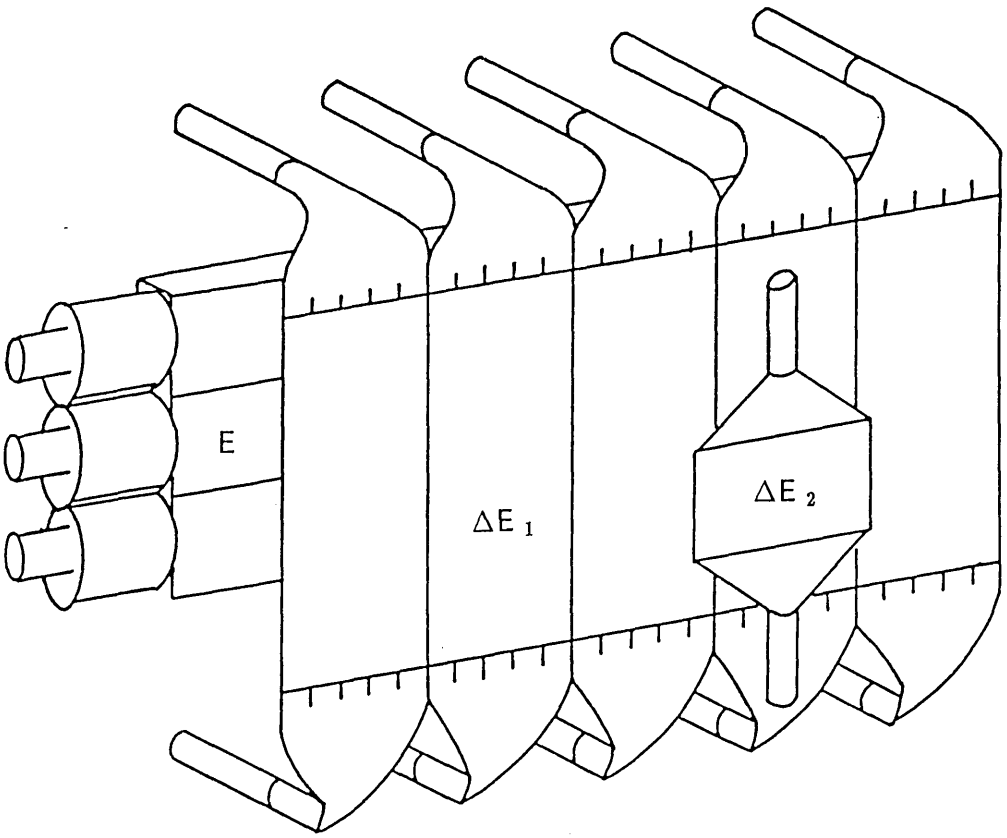

Figure 3.7: *Arrangement of the scintillator elements in the proton detection system.*

	E	ΔE_1	ΔE_2
no. of elements	3	5	1
horizontal (mm)	1000	200	440
vertical (mm)	135	500	160
depth (mm)	110	3	1
total area (mm^2)	1000×405	1000×500	440×160
Photomultiplier	EMI9823KB 130 mm ϕ	EMI9954KB 50 mm ϕ	EMI9954KB 50 mm ϕ
Scintillator	NE110	NE110	NE110

Table 3.3: *Specification of the Proton Telescope*

beam collimators, beam path or dump. The shape and position of the ΔE_2 element varies with the dimensions of the target and the aim of the particular experiment and so it will be discussed separately. The second bank of transmission detectors (ΔE_1) are used in conjunction with the E blocks for particle identification. These latter two detector subsystems are built into a common mechanical framework and are operated as a single unit. The thickness of the E detectors is sufficient to stop a ~125 MeV proton entering the block at normal incidence. The specifications of the detector are summarised in table 3.3 .

In scintillator blocks of this length light attenuation may be a significant problem. The scintillation material used, NE110, was chosen for it's relatively long attenuation length (4 metres). The surfaces of the plastic blocks were

polished to facilitate the transmission of light along the block by successive total internal reflections. The blocks were then loosely wrapped in aluminised mylar foil which reflected some of the transmitted light that would otherwise be lost. The photomultipliers used were 14 dynode, 130 mm diameter EMI 9823KB tubes. These have a high gain, fast rise time and a spectral response well suited to the light output of NE110.

3.3.2 Detector Performance

In the absence of a low intensity variable energy proton test beam the performance of the proton telescope must be inferred from suitable experimental photoreaction data. While such a method is not ideal for the extraction of general performance parameters, such as position and energy resolution, it has the advantage of placing the detector response in the context of the particular experimental conditions in which it must operate. For example, figure 3.8 shows the pulse height signal measured in ΔE_1 plotted against the stopping detector signal E for the reaction $^{12}C(\gamma, p)$. This figure shows clearly the ability of the detector to separate protons and deuterons by means of differential energy loss.

3.3.3 Position Response

A 5 mm thick steel plate pierced with a regular pattern of 20 mm diameter holes was placed immediately in front of the plane of the ΔE_1 detectors. This mask was sufficiently thick to stop protons of 55 MeV and to degrade severely the energy of those of higher energy. Used in conjunction with a thick low-Z target the plate has the effect of producing a set of localised high

energy proton sources at well determined positions. Figure 3.9 shows a time difference spectrum for high energy protons for one E block and one mask position. The centroids of each peak are used to calibrate the time difference information in terms of position. The response of one E detector is shown in figure 3.10 . The time-to-position relationship is linear over the central 85% of the length of the detector. The response of the ΔE detectors was found to be linear over nearly the whole length, in particular over the central 40 cm of the detector which is backed by a stopping detector.

Allowing for the finite diameter of the holes in the steel mask, the position resolution of the detector was found to be 24 mm FWHM horizontally and 41 mm FWHM vertically. At a target distance of 50 cm this represents an angular resolution of 2.7 °horizontally and 5.2 °vertically. These figures were determined using high energy protons issuing from the normal target position and so are relevant to normal experimental conditions. This is valuable since the spatial distribution and time structure of the light pulse created in the scintillator block by a proton cannot be reproduced by 'artificial' means, such as a radioactive source or LED light pulser.

3.3.4 Energy Response

The light transmitted through a long scintillator suffers attenuation through absorption and incomplete reflection. Tests with similar devices [52] suggest that the light attenuation may be modelled as an exponential function of distance from the photomultiplier tube, except in the region very close to the tube face. Making this assumption the total light collected at the ends of a

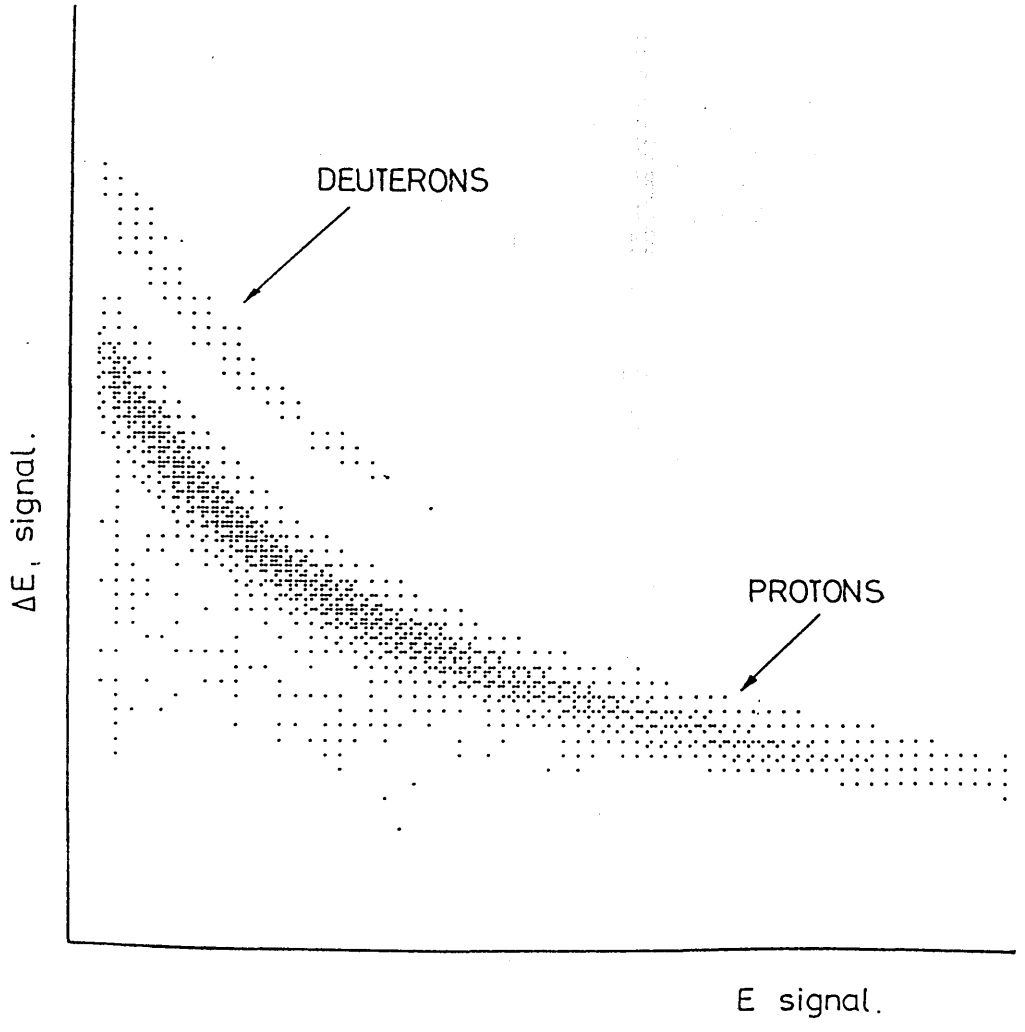

Figure 3.8: *Particle identification by means of differential energy loss in* E *and* ΔE_1.

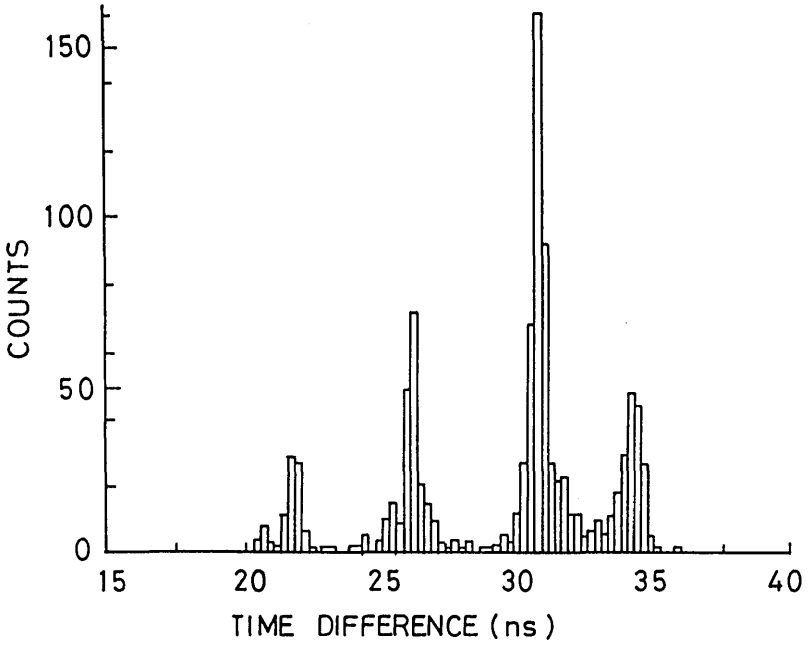

Figure 3.9: *Time difference spectrum for an* E *detector*

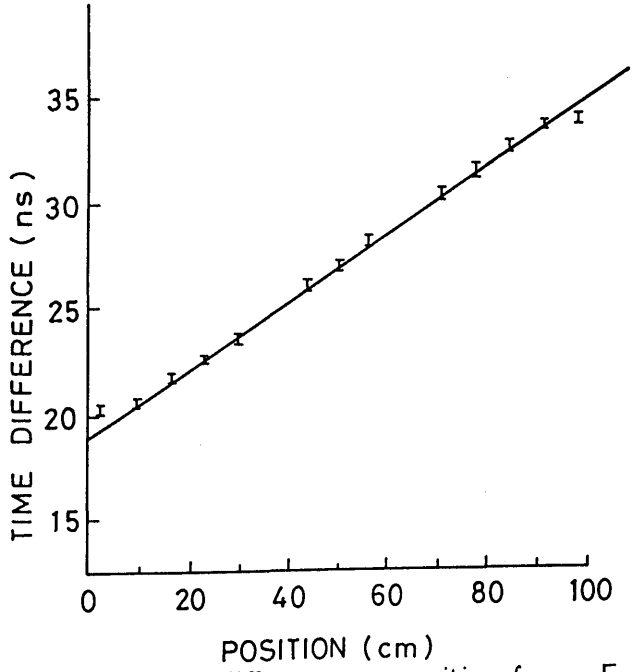

Figure 3.10: *Time difference vs. position for an* E *detector*

scintillator of length d due to an event at position x has the form :

$$\Sigma_1 + \Sigma_2 \equiv Ce^{-\lambda x} + Ce^{-\lambda(d-x)} \tag{3.2}$$

However, if the geometric mean $\sqrt{\Sigma_1 \Sigma_2}$ of the two signals is used instead of the sum then the position dependence cancels.

The effective attenuation length of the E blocks was measured to be 2.3 m. This is rather shorter than the quoted attenuation length of 4 m for NE110 bulk material. The difference is attributable to the light transmission mechanisms operative in a long thin block. The bulk of the light reaching the photomultiplier tubes will have been reflected from the long faces of the block several times. Not only does this increase the effective path length in the scintillator and thus the absorption losses but it also allows light to be lost due to incomplete internal reflection. Close to the photomultiplier face however, the light output of the detector increases sharply as the light can now be directly collected by the photomultiplier which subtends a large solid angle. The nonlinearity of the position response towards the ends of the detector as seen in figure 3.10 may also be related to this effect since the characteristic time structure of the pulse is dependent on the light collection mechanism.

The response of the detector to high energy protons was determined via the D(γ, p) reaction with tagged photons where the knowledge of the photon energy and proton emission angle fix the initial energy of the proton at the target. The energy losses suffered in the air and the Δ E detectors may be calculated to determine the energy actually absorbed in the stopping detector. Figure 3.11 shows the measured proton pulse height signal plotted against the calculated proton energy over a range of energies from 39 MeV to 97 MeV . The response is seen to be linear over this energy range.

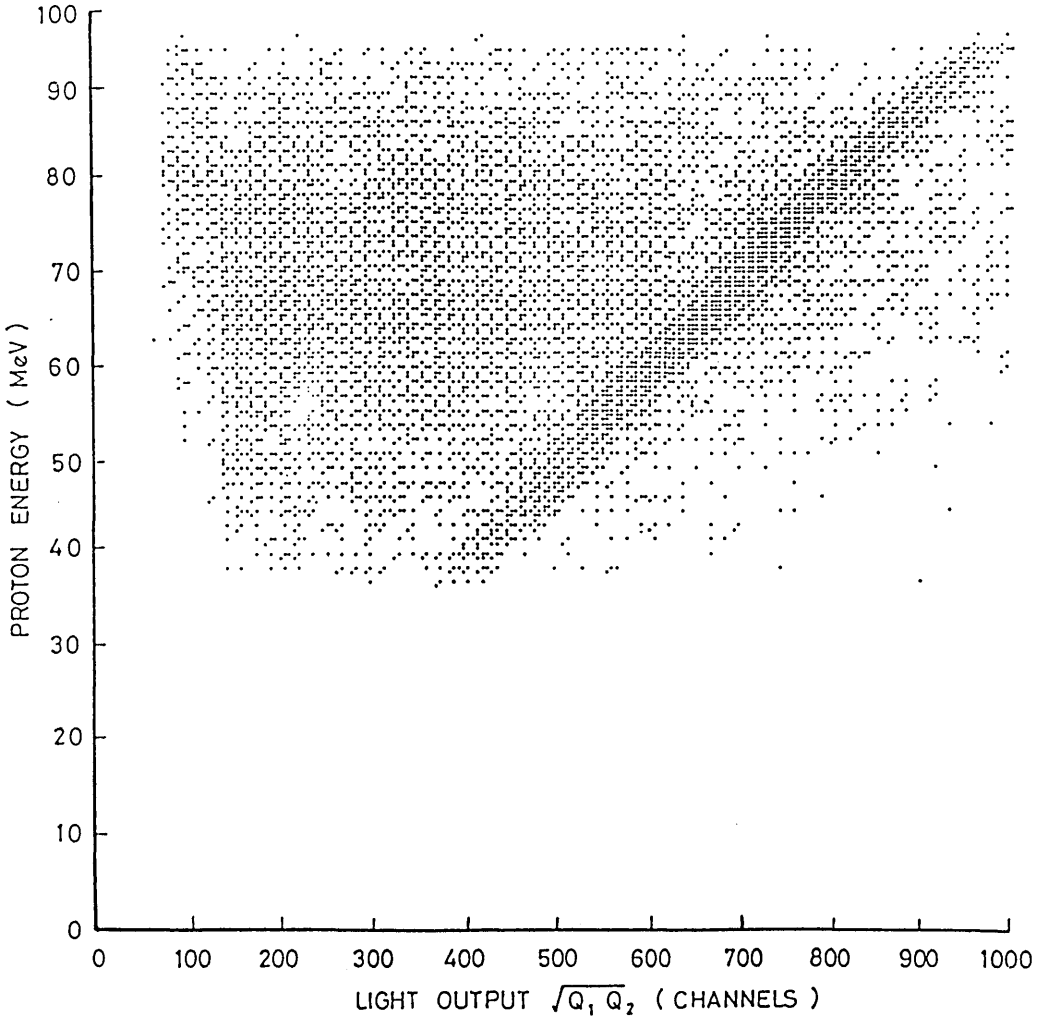

Figure 3.11: *Calculated proton energy vs. measured energy signal.*

E_p (MeV)	FWHM (MeV)
46	2.1
60	2.8
71	3.1

Table 3.4: *Energy resolution of the proton telescope: All energies in* MeV .

The width of the proton locus in figure 3.11 is increased by variations in energy loss of protons originating in different parts of the D_2 target and by the finite resolution of the measured proton angle and photon energy. When these contributions are assessed and unfolded the results of table 3.4 are obtained for the resolution of the system.

3.4 Triggering and Data Acquisition

The instrumentation of the detector system must fulfill two principal functions. Firstly, it is necessary to make online decisions as to when the raw detector signals presented to the processing electronics constitute a useful event. In the present experiment the basic requirement is that a charged particle with the energy loss characteristics of a proton be detected in coincidence with an electron in the tagging detector. (In practice, a considerable latitude is allowed in the imposition of these conditions, to ensure that all the potentially valid events are recorded.) The second function of the electronics is to convert the analogue and timing signals from the detector system to digital information which can be stored on magnetic tape. In the present Mainz

system these operations are performed by CAMAC modules controlled by an HP1000 computer. The arrangement is shown schematically in figure 3.12 .

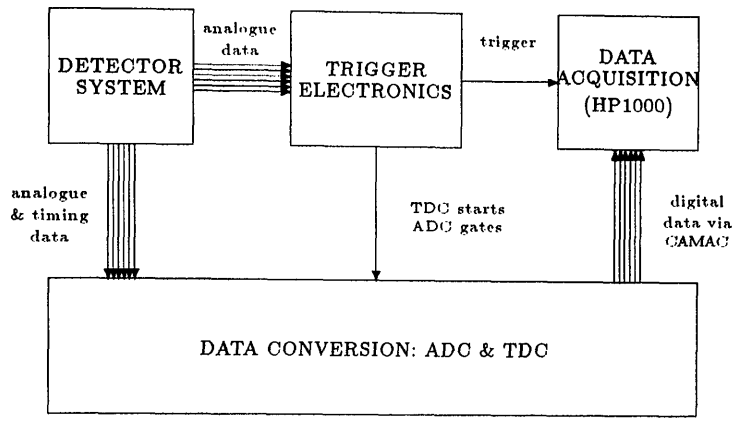

Figure 3.12: *Triggering and data acquisition*

3.4.1 Focal Plane Detector Electronics

The FPD electronics consist of a large number of identical channels required to do one specific task which is to register the trajectory of fast electrons through the focal plane. Accurate pulse height information is not required from the signals presented to the electronics, only timing information. Thus the scintillators in the focal plane array are performing what is essentially a logic function. Their associated electronics need only process analogue pulses with a limited dynamic range though the circuitry must be fast enough to cope with data rates of up to 10^6 per channel without appreciable dead time. It was thought to be inappropriate to instrument the focal plane with a large number of commercial modular NIM type units to perform this specialist task and it was decided to custom build the FPD electronics.

The FPD circuitry is mounted directly on the detector array itself to minimise the effects of dispersion in the connecting cables and preserve the rise-time of the analogue pulses. This measure, together with the small dynamic range of the signals, permits the use of fast leading edge type discriminators without prejudicing the time resolution of the system. The logic outputs of the 92 scintillator channels are fed in 91 adjacent pairs into overlap coincidence units with a coincidence width set to 8 ns. Up to this point ECL circuitry has been used and now the ECL logic is converted to NIM type and fed to CAMAC controlled pattern recognition units. The triggering rate in the ladder must be integrated throughout the experiment for the purposes of flux normalisation. To this end the logic outputs are fanned in groups of 8 into prescalars which divide the rate by 2^4 and then the divided rates are fed into 12 free running CAMAC scalers. At normal beam rates a further divide factor of 2^{15} is used before integration.

3.4.2 Proton Detector Electronics

Figure 3.13 shows the instrumentation of the proton detector. Each scintillator element has two photomultipliers, the signals from which are fed to constant fraction discriminator units. A coincidence between the logic outputs from each pair is registered in a mean timing coincidence unit, which produces an output whose timing is independent of the light propagation delays to either end of the scintillator. This is the signal which indicates that a detector element has fired. A three-fold coincidence of ΔE_1, a ΔE_2 element and an E element identifies a charged particle emerging from the target. Most of the electrons incident on the detector can be rejected online by means of a lower level threshold set on the weighted analogue sum of the E and ΔE_1

signals. This is essentially a $\frac{dE(E)}{dx}$ discrimination between particle types. This part of the circuit produces a veto pulse which suppresses the previous coincidence output. The logic output pulse which is produced when all of the above conditions are satisfied is time correlated with the detector element whose pulses arrive at the three-fold coincidence gate latest. It is important to set the relative time delays on the E , ΔE_1 and ΔE_2 circuits such that one or other detector bank always makes the event timing. In the present experiment either the E detectors or the ΔE_2 detector may be chosen. The ΔE_2 detector is very close to the target and so it provides a timing signal which is independent of variations in particle flight times due to differences in energy or flight path. However, the intrinsic timing resolution properties of the E detectors are superior to that of the ΔE_2 detector because of their very much greater light output.

3.4.3 Trigger Electronics

The basic task performed by the instrumentation of a tagged photon experiment is to record coincident signals from the experimental detectors and the tagging detectors. The present system has been designed in such a way that the signal from different experimental systems can be interchangeably 'plugged into' the master coincidence with the FPD . The detector system is required to produce a single signal for this purpose which is identified on figures 3.13 and 3.14 as the X-trigger. The X-trigger timing is taken as the reference time for the event, against which the arrival time of all the individual detector signals is measured.

The trigger circuit which makes the master coincidence is shown in figure

3.14 . It is necessary to identify which FPD channels fire in coincidence with the X-trigger. This is achieved using 6 CAMAC pattern recognition units (PUs). These are essentially 16 channel gated flip-flops into which are fed the logic outputs of the 91 individual FPD channels. [1] The flip-flops are enabled by a pulse derived from the X-trigger(this is typically set to $\sim$ 60 ns) whose width determines the online coincidence resolution of the experiment. This is significantly greater than the observed intrinsic resolution of the detectors, however the use of a relatively long coincidence gate permits sampling of the random coincidence background as well as the true coincidences. The PU makes a fast coincidence between the gate pulse and the .OR. of the FPD inputs, the output pulse being time correlated with the earliest FPD signal. The .OR. of the PU coincidence outputs is used to start the data acquisition procedure by setting a flip-flop which disables the X-trigger input and by setting the CAMAC controller input register which provides the interrupt request for the HP1000 computer.

3.4.4 Data Conversion and Acquisition

Data Conversion is based on LeCroy 2228A time-to-digital converters (TDCs) and Le Croy 2249A charge sensitive analogue-to-digital converters (ADCs). The TDCs are 8 channel units with a common start input. They have 12 bit resolution (2048 ch) and a conversion gain switchable between 50 or 100 ps per channel (nominal). The 11 bit (1024 ch) ADCs are 12 channel units with a common gate input and a sensitivity of 250 pA full scale.

Each photomultiplier output has an associated ADC, gated by a pulse de-

[1] The actual division of channels is 12,16,16,16,16,15

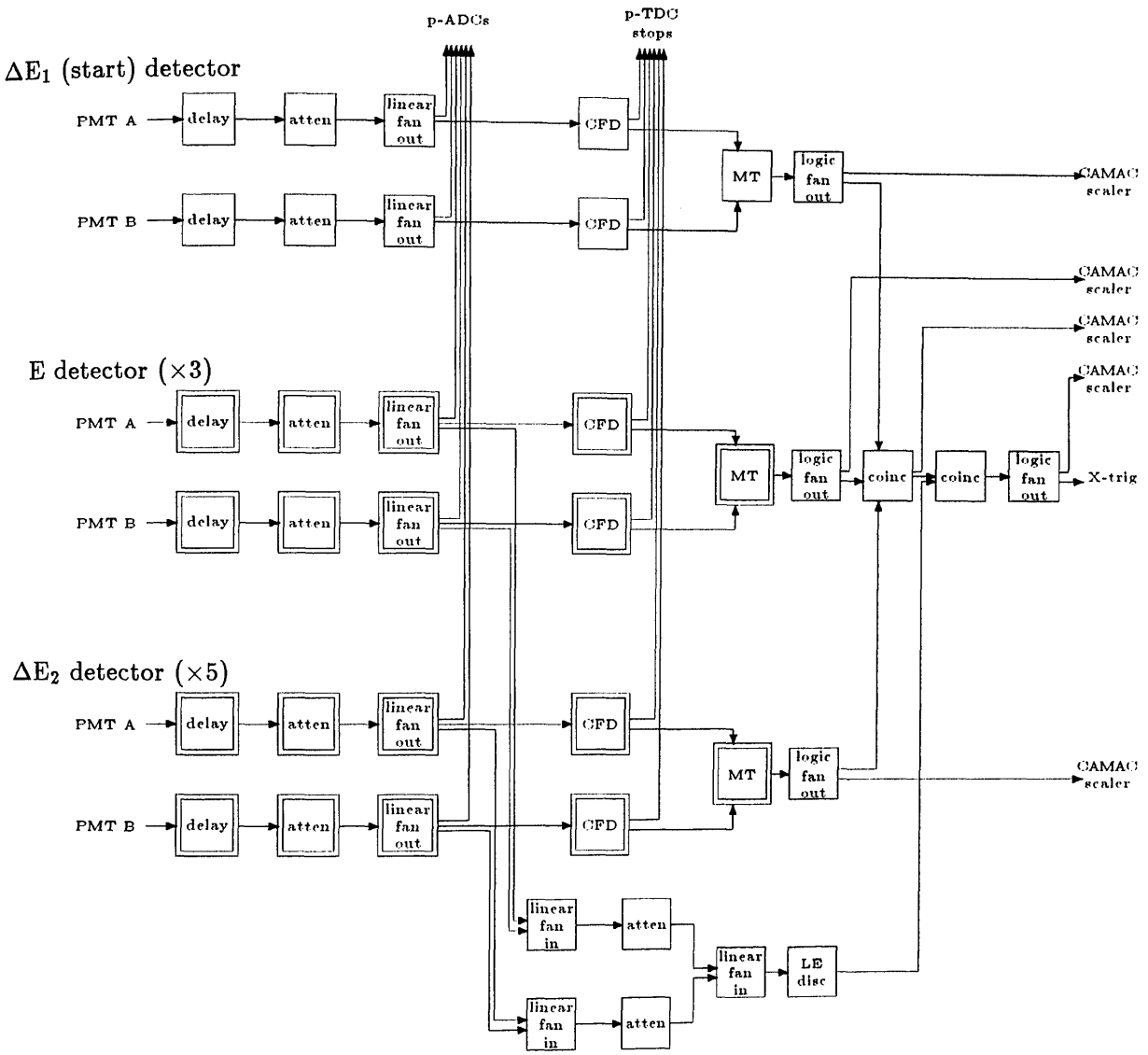

Figure 3.13: *Block diagram of proton detector electronics. Double box indicates several identical units as indicated. coinc – coincidence unit; atten – attenuator; LE disc – leading edge discriminator; CFD – constant fraction discriminator; MT – mean timer*

rived from the X-trigger. The typical gate width in use with plastic scintillator detectors is 120 ns, comfortably longer than the scintillator decay time but not so long as to present difficulties with pulse pile up under normal running conditions. The constant fraction discriminator output from each photomultiplier channel is used to stop a TDC started by the X-trigger thus giving the timing of that channel relative to the reference time for the event.

There are also 6 TDCs started by the X-trigger and stopped by the PU coincidence output signals described above. These give the timing of the detector signal with respect to the tagging signal. Thus each TDC is stopped by the .OR. of $\leq$ 16 FPD channels. This arrangement was chosen for reasons of economy of circuitry and CAMAC rack space. There is also a TDC stopped by the .OR. of all 91 channels. This has proved to be convenient for online data monitoring and for the initial stages of offline analysis.

When the HP1000 receives an interrupt request the PUs, TDCs and ADCs are read sequentially via a serial line. When the data transfer is completed the CAMAC crate controller output register is reset which in turn enables the X-trigger input. The content of each ADC and TDC is stored as a 16 bit data word, the 4 most significant bits identify the channel and the 12 remaining bits store the channel contents. At this stage the data is compressed in the HP1000 by the removal of all zero datawords before being stored as a complete 'event' in one half of a swinging buffer (The two halves of the buffer are filled and transferred to the HP3000 alternately.) The HP3000 computer writes the incoming data to magnetic tape and can also be used for on-line analysis and display.

The data rate was limited to $\sim$ 50 Hz throughout the experiment. At this

rate dead-time effects were found to be negligible. The effective limit on the data rate was the rate of random coincidences between tagging electrons and X-triggers produced by untagged photons.

3.5 Flux Normalisation

Absolute normalisation is particularly important in the present experiment. The use of the tagging technique permits the determination of the photon flux from the electron beam rate. There is a complication, namely the tagging efficiency effect discussed earlier. A system has been devised by which ϵ_T is measured at intervals and checked for constancy throughout the experiment. The tagging efficiency is measured by placing a photon detector in the beam and directly measuring the ratio of tagged photons to tagging electrons. Since the detector cannot be left in the beam during experiments and cannot operate at normal experimental beam fluxes an ion chamber is placed in the shielded beam dump to monitor the photon flux continuously. The ion chamber is not calibrated as a quantameter, rather the ratio of the ion chamber current to the ladder scaler rate is used to monitor changes in ϵ_T.

3.5.1 Tagging Efficiency

The detector used for the tagging efficiency measurements is required to be effectively 100% efficient for photons in the tagged region. However it is not essential that the detector absorb the electromagnetic shower completely since pulse height resolution is not important for this purpose. It must also have a reasonably short decay time since it must absorb the whole bremsstrahlung distribution and not just the tagged photons. Even when the tagging rate has

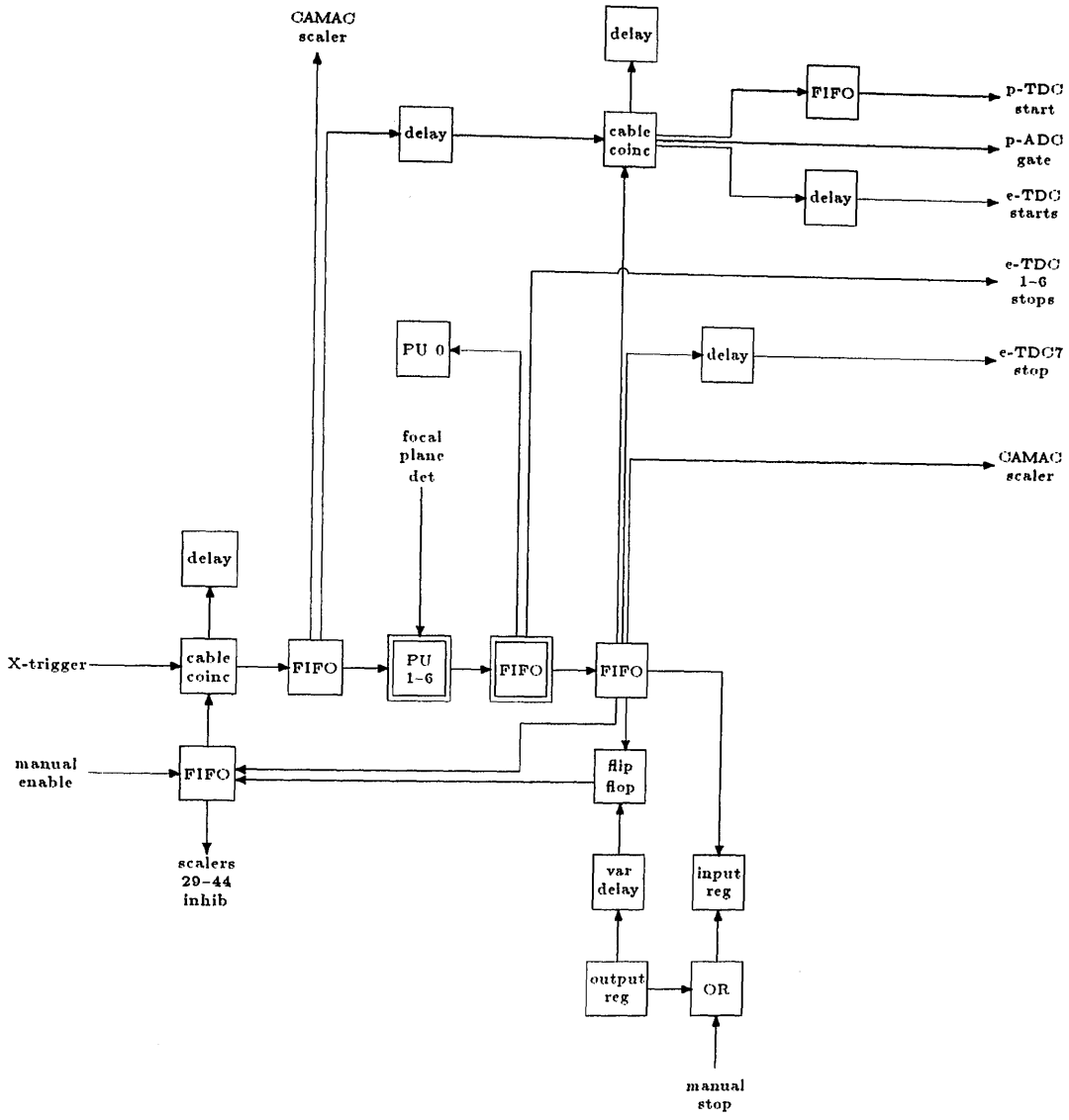

Figure 3.14: *Block diagram of the processing electronics from the detectors to the HP1000 computer. Double boxes indicate six identical units. FIFO – fan-in fan-out unit; PU – bit pattern recognition unit; cable coinc – coincidence unit in which a length of cable is used to set the output pulse width.*

been reduced to 10^3 the total rate in the detector could be 10^6. The system chosen for the purpose was a $15 \times 15 \times 50$ cm^3 block of SCG1-C scintillating glass coupled to an EMI 9823KB photomultiplier. (This represents a thickness of 12 radiation lengths). SCG1-C is a cerium loaded barium glass compound which scintillates and also waveshifts it s Cerenkov radiation, improving its transmission. It produces approximately five times more light than a conventional Pb glass Cerenkov detector. This reduces the phototube noise level to less than the equivalent of 20 MeV allowing a threshold to be set such that the detector can be used as a 100% efficient monitor for the tagged photons. The measured resolution of the detector was 29% FWHM at 100 MeV , which compares favourably with the figure of 50% obtained with a similar piece of Pb Glass. The rise time of the pulses in SCG1-C is 4 ns and the characteristic decay time 70 ns.

The tagging efficiency ϵ_τ is defined as the ratio of the tagged photon rate vs. the tagging electron rate, with a (small) correction for background in the ladder. The tagging monitor detector was placed in front of the collimator and data recorded with and without a radiator in the beam. The input data are the 12 ladder scalers, the X trigger scaler and the livetime scalers for both radiator-in and radiator-out runs. The tagging efficiency (averaged over the whole ladder) is then defined as

$$\epsilon_\tau = \frac{Interrupts^{Rad\ in}}{\sum_{i=1-12}^{Rad\ in} Ladder \; - \; (\sum_{i=1-12}^{Rad\ out} Ladder \times \frac{Livetime^{Rad\ in}}{Livetime^{Rad\ out}})} \tag{3.3}$$

The high total counting rate in the scintillating glass detector limits the tagging rate to $\sim 10^3$ during an efficiency measurement as opposed to $\sim 10^7$ during a typical experiment. Therefore beam independent room background, which is a negligible consideration during normal running, may become a

serious effect. There is of course also a beam dependent background from the beam-line and beam-dump. Measuring with the radiator removed allows both effects to be taken into account. In practice the background correction is only of the order of 1%.

3.5.2 Ion Chamber

The ion chamber is of the thick walled NBS type [56]. The unsealed chamber has a 6 cm aluminium converter on the front face and is operated at 1200 V. It is mounted in a shielded beam dump 5 metres downstream of the target. The conversion efficiency of the thick input wall is sufficient to swamp the conversion due to the target contents and so target-full and target-empty runs may be directly compared. The high voltage plates are connected to an electrometer whose output is fed to a current digitiser and thence to a scaler. The sensitivity of the ion chamber is such that a 20 nA electron beam incident on a 25 μm aluminium radiator results in a 3 nA current in the ion chamber. This is to be compared with a leakage current of $\leq$ 0.5 pA obtained after several hours of operation.

3.6 the Liquid Deuterium Target System

The target system consists of a 50 cc cell filled from a refrigerator operated in a closed deuterium gas system. The cell is enclosed in an evacuated chamber which includes a large kapton window to permit the passage of the the photon beam and the outgoing protons. The cell is mounted on a flange close to the cold head at the bottom of the refrigerator. The refrigerator is coupled to the scattering chamber via a bellows section whose operation permits the cell to

be raised and lowered into the beam.

3.6.1 The Scattering Chamber

The shape of the scattering chamber is determined by the need to maximise the deuterium containment volume in the case of a leak in the cell while minimising the area of the chamber window. The chamber, which is of welded, cylindrical construction, was made from 5 mm aluminium with a 20 mm base plate. The top flange engages with the bellows/refrigerator system while the base plate rests on the broad flange of a pumping stand. The pumping stand incorporates a turbo pump and a rotary pump connected in series. A vacuum of $\sim 10^{-8}$ bar is required before the convective heating rate falls below that of the radiative heating at liquid hydrogen temperatures. This would take many hours to achieve using the pumps alone. The cold cell, however, acts as a cryogenic pump and the system easily reaches the required pressure.

The chamber has a single 'wrap-around' window which is designed to permit the passage of protons at all scattering angles on one side of the target and which also serves as the beam entrance and exit window. The window, which is approximately 500 cm^2, is made from 120 μm kapton. The size of the window is such that three quarters of the circumference of the chamber is cut away, thus making it necessary to add additional supporting struts to the proton detector side of the chamber. The struts (shown in figure 3.15) were designed to be movable in order not to interfere with the proton flight paths corresponding to different detector orientations. (figure 3.20) They were fitted with springloaded studs at either end which fitted into indentations in the top and bottom flanges of the chamber. Once the struts were installed

the chamber could be evacuated and then the additional compressional force locked them into place.

3.6.2 The Deuterium Refrigerator and Target Cell

The refrigerator, which is shown schematically in figure 3.16, is a two stage commercial device operated in conjunction with a 20 bar helium compressor. The primary stage of the device can attain 40°K with a cooling power of 1 W. The second stage can cool the cold head to 10°K. The cold head is shielded by a dome shaped screen attached to the primary refrigerator. The gaseous deuterium is piped to a chamber attached to the cold head flange where it condenses and drips into the target cell. The thermal coupling of the cell to the cold head is rather poor and the cell is cooled by the continual evaporation of the deuterium. When the cell is sufficiently cold the liquid begins to accumulate, the rate of filling or emptying being governed by the relative rates of evaporation and recondensation. The cold head is fitted with a temperature monitor (a calibrated resistor; platinum for $T > 70$°K, carbon for $T < 70$°K) and a heating coil which are connected to a feedback controller. Once the cell is full the cold head must be stabilised at a temperature where a dynamic equilibrium is established between the evaporation rate and the condensation rate. To achieve this a reference temperature is set on the feedback controller which then alters the heating current according to the temperature reading. In order to achieve finer control of the system both the amplification and time constant of the feedback loop are adjustable. In practice the nominal reference temperature used was 19.5°K (c.f. deuterium boiling point 20.4°K, and freezing point 14°K). The system was operated at the upper end of the usable temperature range in order to prevent the liquid

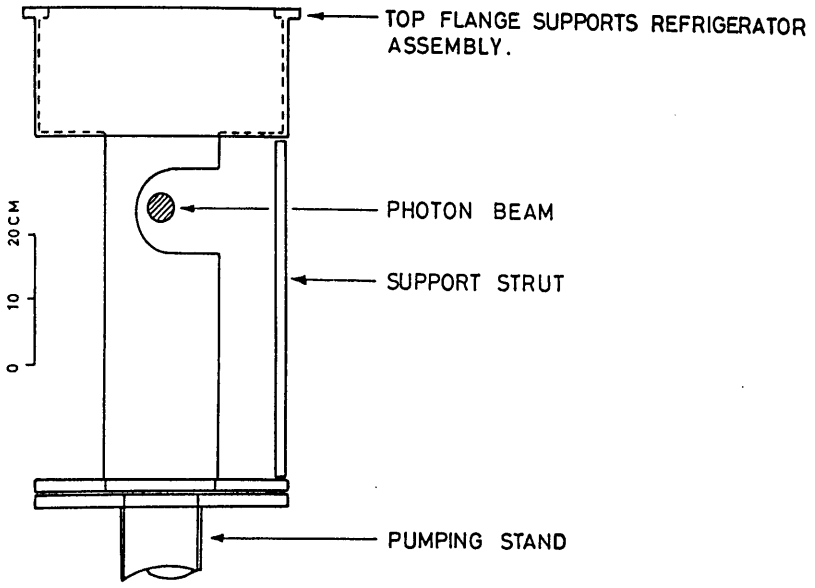

Figure 3.15: *The scattering chamber.*

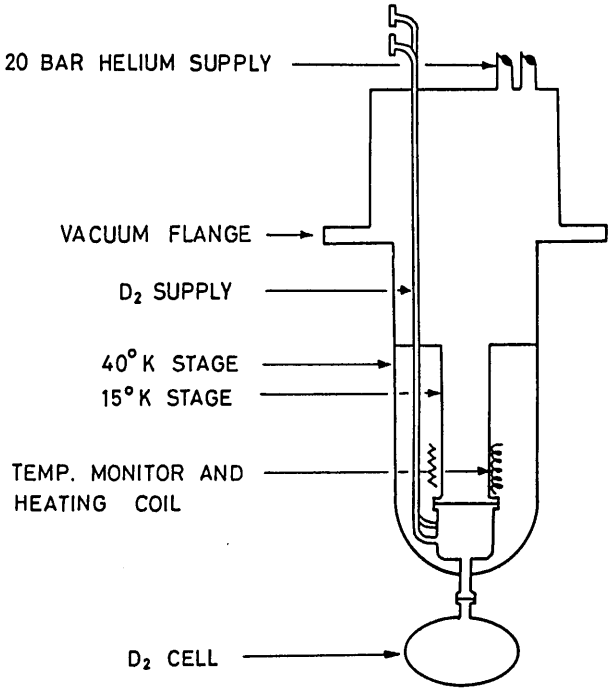

Figure 3.16: *The refrigerator system.*

freezing in the narrow filling pipe near the cold head. If this were to happen the cooling by evaporation would cease and the cell could explode. Although most of the cell was wrapped in superinsulating foil there was nontheless a large input of radiated heat from the surroundings which caused the liquid in the cell to boil quite vigourously. The boiling reduced the mean density of the target and therefore the count rate. A series of measurements which were made to determine the magnitude of this effect are described in Appendix D. The boiling correction was determined to be $(7.5 \pm 1)\%$.

The target cell (figure 3.17) consisted of an elliptical aluminium frame, 4 mm thick with major and minor axes 53 mm and 25 mm respectively. Kapton windows 70 μm thick were glued onto the frame and elliptical plates bolted onto both sides of the assembly while the epoxy was still soft. The profile of the cell windows at a series of overpressures from 1 to 1.5 bar was measured on a 1 cm grid using a clock gauge. The sections shown in figure 3.17 are for 1.1 bar, the normal operating pressure. The combination of a cell with curved windows and a photon beam with a nonuniform spatial distribution results in the effective target thickness being greater than that obtained by averaging the cell thickness over the beam spot. The correct beam-weighted average thickness was obtained by means of a Monte Carlo calculation described in chapter 4. The magnitude of the correction for a target angle of 30°and a 40 mm diameter beamspot was 10%.

3.6.3 Deuterium Gas Supply

The gas supply system is shown in figure 3.18. The high pressure deuterium reservoir was never opened directly to the rest of the system. The deuterium

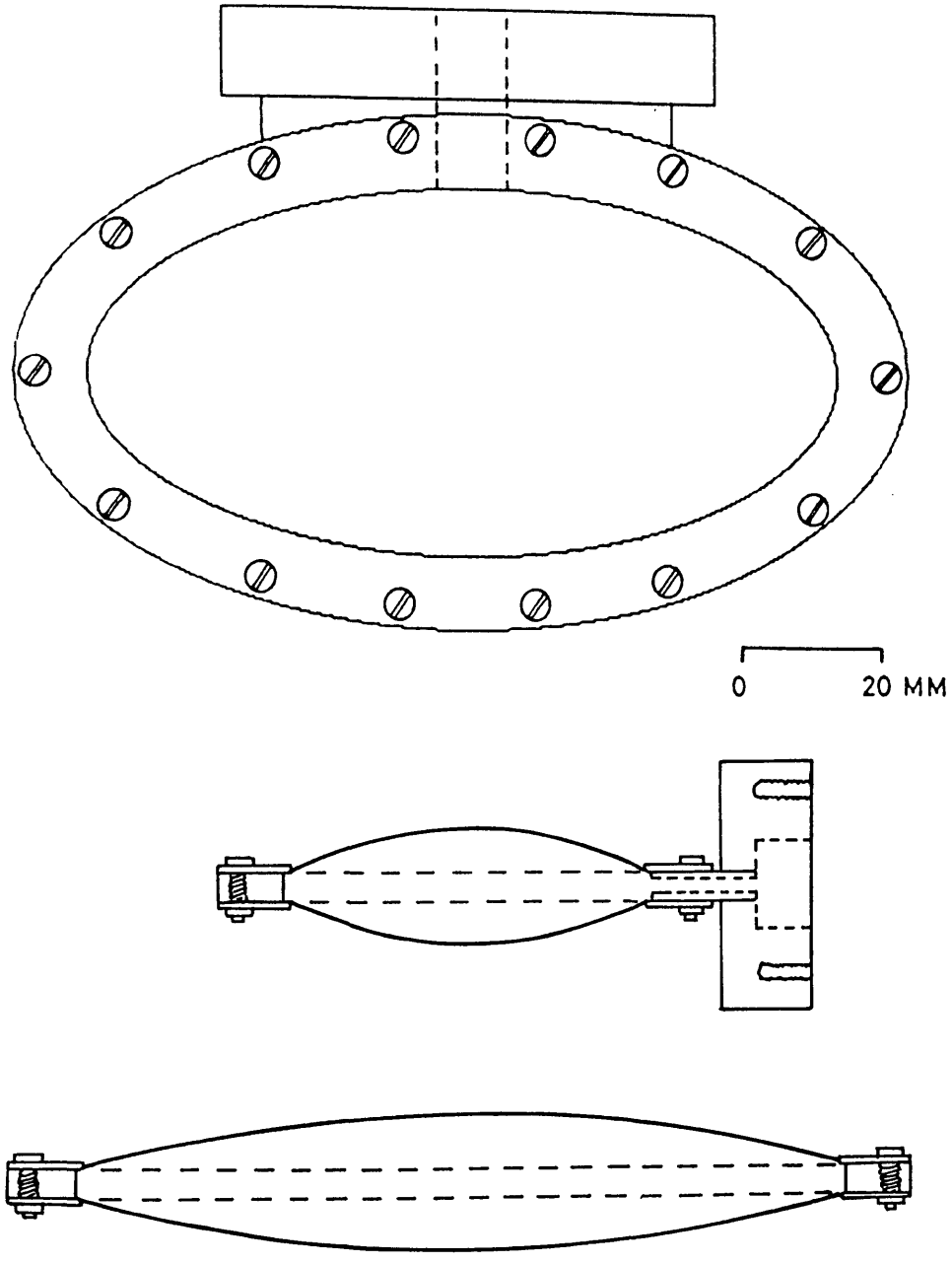

Figure 3.17: *Liquid deuterium target cell*

was instead transferred in small quantities via a low pressure buffer tank. The buffer tank was used to maintain the pressure in the deuterium circuit at between 1 and 1.5 bar. The upper limit was determined by the strength of the cell windows and the lower limit was set to ensure that a leak in the system would not result in the ingress of atmospheric water vapour which would freeze in the coldest part of the system with dangerous consequences. When not in use the deuterium circuit could be pumped out, flushed with dry nitrogen and then stored filled with nitrogen at slight overpressure to prevent contamination. The normal deuterium pumping line, the emergency overpressure release line and the scattering chamber pumping stand were all vented to atmosphere outside the outside buildings via long hoses in order to prevent a build up of deuterium in the experimental areas.

3.6.4 The Active Collimator

The actual design of the detector represented as ΔE_1 in figure 3.7 was complicated by the need to have an scattering chamber around the liquid deuterium target. Indeed the 20 cm radius overhang above the window prevents the use of a detector with vertical fishtail light guides as shown in figure 3.7. Horizontal lightguides of conventional design are unsuitable because they would protrude into the photon beam when the detector system was placed at forward or back angles. The device eventually constructed was based on an MIT design [57] as shown in figure 3.19. Two 40 mm diameter cylindrical light guides attach tangentially at each end of a $1 \times 440 \times 160$ mm rectangular sheet of scintillator. Light from the scintillators enters the lucite cylinders and spirals towards the photomultiplier tubes. The detector was fixed onto the underside of the scattering chamber overhang in one of three positions covering the range of

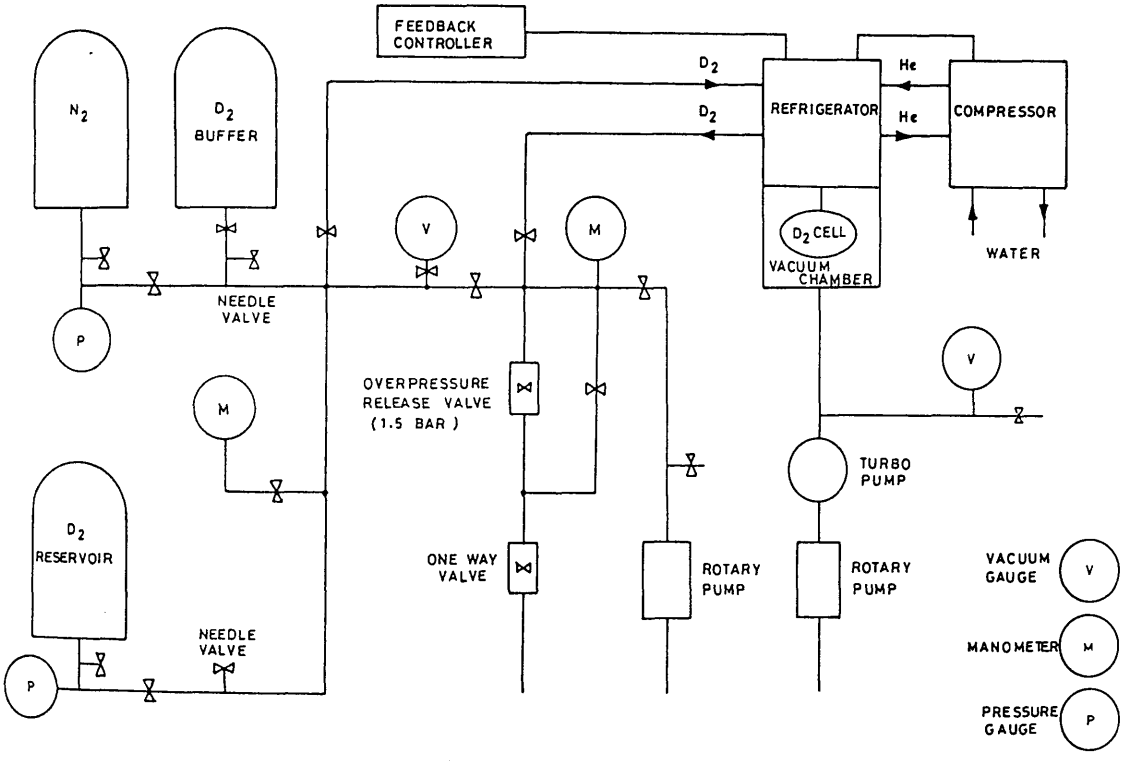

Figure 3.18: *Deuterium gas supply system*

proton emission angles. The light collection efficiency of this configuration is rather low and the transmission in the long thin scintillator is poor. For this reason the detector was not used as part of the dE/dx system. Nontheless, tests indicated that the system should be 100 % efficient for proton detection and so it could be used as a collimator, acting essentially as a logic element in the detector system. It was decided, however, to err on the side of caution and the detector trigger was wired to require an .OR. of the two phototube signals rather than the more usual .AND..

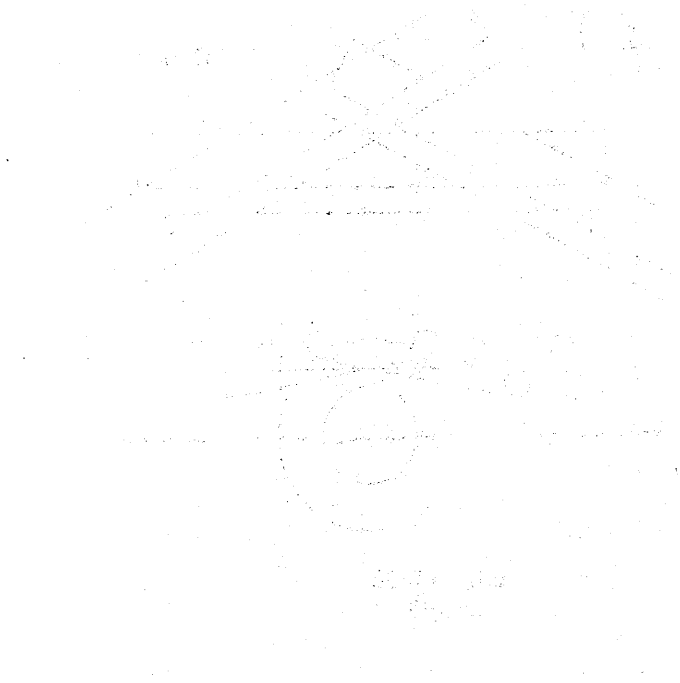

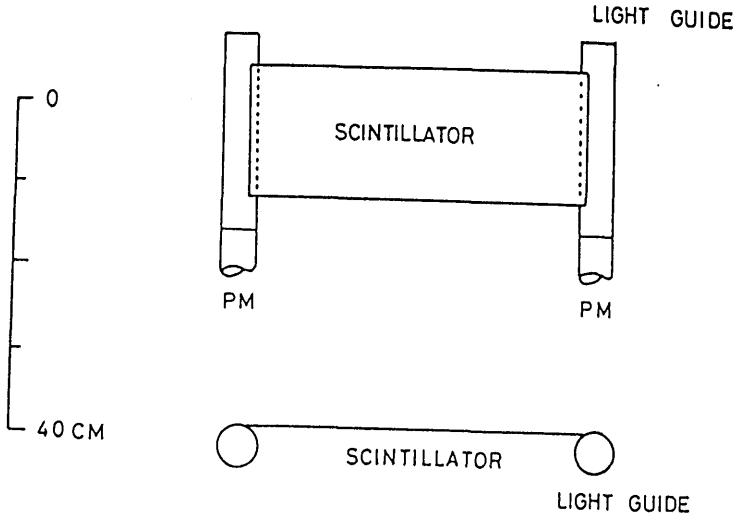

Figure 3.19: *The on-target active collimator detector*

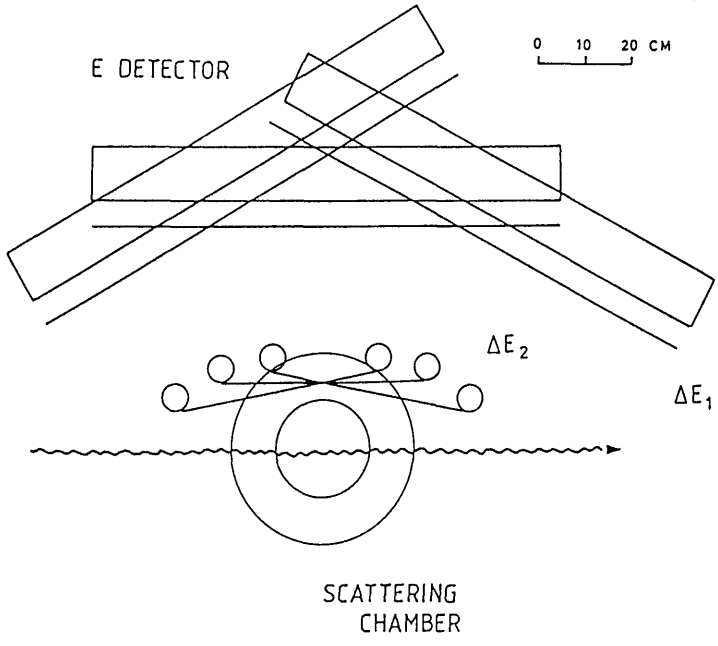

Figure 3.20: *Plan view of experimental system showing the three detector configurations used to cover the angular distribution of photoprotons.*

Chapter 4

Monte Carlo Simulations

4.1 Introduction

This chapter describes a complete Monte Carlo simulation of the present $D(\gamma,p)$ experiment which has been developed in order to evaluate the systematic corrections to the data. Included in the simulation are effects due to the beam-target geometry, the detector acceptance in the centre of mass frame, energy losses of the protons in the target, energy deposition in the detector, light production non-linearities, nuclear interactions of the protons in the CH scintillator medium, and also variations in the light collection efficiency throughout the scintillator blocks. The Monte Carlo data is analysed and binned in the same fashion as the real experimental data and therefore the simulation provides an efficiency correction factor specific to each data point as well as providing global normalisation factors to account for the tagging efficiency and the combination of beam and target geometries.

4.2 Tagging Efficiency

This section of the code models the production of bremsstrahlung radiation arising from the passage of a relativistic electron beam of energy E_0 through a thin (finite) foil with atomic and mass numbers Z and A respectively. Photons of energy E_γ and angle θ (*wrt* the initial electron direction) are selected from approximate angle and energy distributions in order to calculate the fraction of the total flux falling within a specified collimation angle θ_c. This fraction represents the *tagging efficiency* ϵ_τ . Account must be taken of the multiple small-angle coulomb scattering of the electron beam as it passes through the radiator foil since this will tend to broaden the photon angular distribution.

Similarly, provision is made for the inclusion of a finite beam divergence and it is also possible to introduce an angular offset between the beam axis and the nominal collimation axis. These latter two effects permit the assessment of the variation in ϵ_τ to be expected over a reasonable range of non-ideal experimental conditions.

Figures 4.1 and 4.2 show the results of the tagging efficiency calculation for a range of radiator thicknesses and photon energies. The tagging efficiency calculated for the experimental conditions, $E_0 = 183$ MeV , $E_\gamma = 140$ MeV , radiator 25 μm aluminium and collimation angle 4.5 mrad , is 65.9 % in good agreement with the measured values which range from 64.1 % to 65.7 %.

The model used for the bremsstrahlung process is that of Bethe and Heitler [28] which gives rise to a differential bremsstrahlung cross-section calculated in the first order Born approximation. Schiff [27] has analytically integrated this expression over outgoing electron angles using a screened atomic potential of the form,

$$V(r) = \frac{Ze}{r} e^{-r/a} \tag{4.1}$$

where a is given by

$$a = \frac{C}{137} \frac{\hbar^2}{me^2 Z^{\frac{1}{3}}} = \frac{C\hbar}{mcZ^{\frac{1}{3}}} \tag{4.2}$$

and C is a dimensionless number of order 137 determined by comparison with a full numerical calculation of the Bethe-Heitler cross-section using the Thomas-Fermi potential. The Schiff expression therefore represents the distribution in energy and angle of radiation from relativistic electrons in very thin targets.

It is convenient to work in terms of a reduced angle ϑ defined as $\vartheta = \frac{\theta}{\theta_B}$ where $\theta_B = \frac{m}{E_0}$. The probability of radiating at reduced angle $\vartheta, d\vartheta$ is given

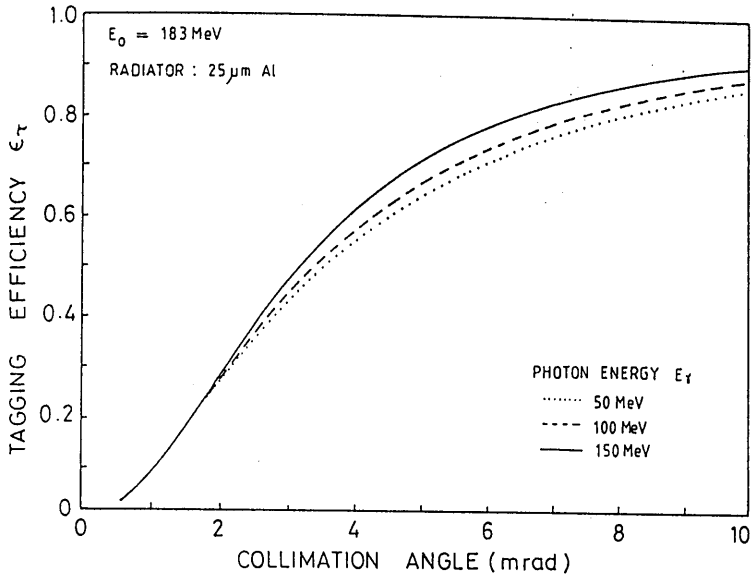

Figure 4.1: *Tagging Efficiency as a Function of Energy*

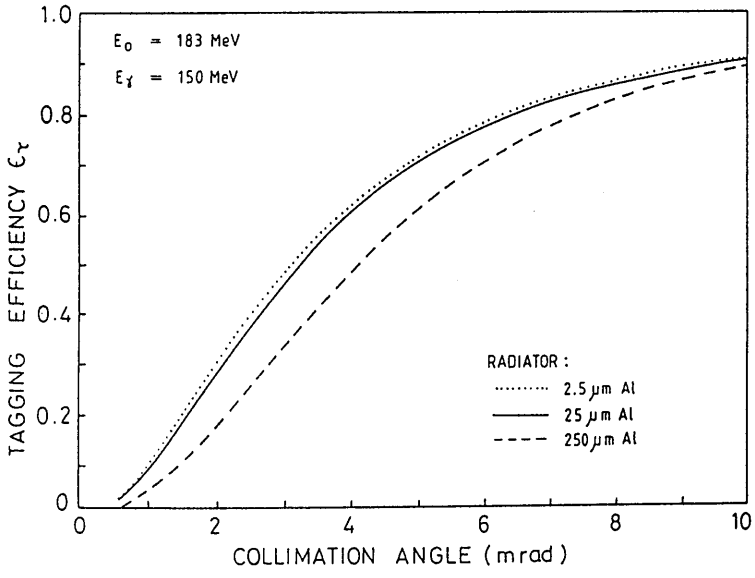

Figure 4.2: *Tagging Efficiency as a Function of Radiator Thickness*

by,

$$P(\vartheta)d\vartheta \propto \vartheta d\vartheta \frac{1}{k}\left[\frac{16\vartheta^2(1-k)}{(\vartheta^2+1)^4} - \frac{(2-k)^2}{(\vartheta^2+1)^2} + \left\{\frac{(2-k)^2}{(\vartheta^2+1)^2} - \frac{4\vartheta^2(1-k)}{(\vartheta^2+1)^4}\right\} lnM\right] \tag{4.3}$$

where

$$\frac{1}{M} = \left[\frac{\theta_B k}{2(1-k)}\right]^2 + \left[\frac{Z^{\frac{1}{3}}}{C(\vartheta^2+1)}\right]^2$$

$$C = 111$$

$$\vartheta = \theta\frac{E_0}{m}$$

$$k = \frac{E_\gamma}{E_0}$$

This expression is not suitable for use near the bremsstrahlung end point ($k = 1$), i.e. where the outgoing electrons have kinetic energies of only a few times mc^2 and the extreme relativistic conditions no longer apply. However for the present purpose one need consider k no larger than 0.85 and the plane wave Born approximation is adequate. Although the Schiff formula has been analytically integrated [58] it is more convenient to use a simpler approximate function $P_{approx}(\vartheta)$ in the Monte Carlo process and then re-weight the event by a factor $W = \frac{P(\vartheta)}{P_{approx}(\vartheta)}$. The function used to approximate the bremsstrahlung distribution is

$$P_{approx}(\vartheta)d\vartheta = \frac{2\vartheta d\vartheta}{(1+\vartheta^2)^2} \tag{4.4}$$

and the re-weighting W is given by

$$W = \frac{(2-k)^2}{k}[lnM - 1] + \frac{4(1-k)}{k}\frac{\vartheta^2}{(1+\vartheta^2)^2}[4 - lnM] \tag{4.5}$$

The tagging efficiency for a typical collimation angle ($\sim$ 5 mrad) is not a strong function of photon energy and in the regime under consideration

($0.45 < k < 0.85$ and $\delta k \sim 0.05$ per data bin) it is sufficiently accurate to take

$$P(E_\gamma)dE_\gamma \propto \frac{dE_\gamma}{E_\gamma} \tag{4.6}$$

as the photon energy distribution.

A gaussian approximation is used to model the multiple small-angle coulomb scattering undergone by the electrons as they pass through the target foil. In terms of the reduced angle ϑ one may write

$$P(\vartheta)d\vartheta = \frac{1}{\vartheta_m^2} exp\left[-\frac{\vartheta^2}{2\vartheta_m^2}\right]\vartheta d\vartheta \tag{4.7}$$

where the r.m.s. multiple scattering angle ϑ_m has the form [59]

$$\vartheta_m = \frac{14.1}{0.511}\sqrt{t}\left\{1 + \frac{1}{9}log_{10}t\right\} \tag{4.8}$$

t being the depth, measured in radiation lengths, in the target at which the distribution is to be sampled. Thickness t (radiation lengths) is calculated from thickness d (gm/cm/cm) using the following [60]

$$t = d\frac{Z(Z+1)}{716A} ln\left[\frac{183}{Z^{\frac{1}{3}}}\right] \tag{4.9}$$

4.3 Effective Target Thickness

In order to obtain an absolute cross-section it is necessary to calculate the *luminosity* of the experiment, that is, the product of the total beam flux and the density (cm^{-2}) of the target nuclei. However, in the present case it is not sufficient to multiply the average density by the total flux. This is because both the photon beam intensity and the target density distribution are non-uniform in the plane perpendicular to the the beam direction. The luminosity L is therefore given by the more general expression:

$$L = \int \Phi(x,y)\rho(x,y)dxdy \tag{4.10}$$

where the beam direction lies along the z axis, Φ is the photon flux, ρ is the target thickness and the integral is performed over the projected area of the beam spot. This integral is performed most conveniently by a Monte Carlo calculation. The beam profile is modelled as in the previous section and the shape of the target cell is given by interpolation within a mesh of measured co-ordinates as described in Chapter 3.

The point of intersection of the photon path with the x-y plane is calculated and the z co-ordinates z_1 and z_2 corresponding to the points (x, y) on the surfaces representing the 'front' and 'back' cell windows are calculated by interpolation. The target thickness $\rho(x, y)$ is then given by the difference $z_2 - z_1$. In order to provide an interaction position for the succeeding stages of the simulation a random z co-ordinate is chosen between the limits z_1 and z_2, this must be weighted according to the target thickness at (x, y). The total event weight is now the product of the photon weight (previous section) and the target thickness weight.

The effects of beam-weighting the target thickness are as follows. When the target is rotated to 30 deg with respect to the beam axis, the thickess along the beam axis is 33.9 mm, the *average* thickness over the 40 mm diameter beam spot is 27.7 mm while the *beam-weighted* target thickness averaged over the same area is 30.7 mm.

4.4 Detector Acceptance

The general definition of the solid angle subtended by an object at a point P whose position vector is $\vec{r}_P$ is:

$$\Omega_P = \int_s \frac{\vec{n} \cdot (\vec{r} - \vec{r}_P)}{|\vec{r} - \vec{r}_P|^3} ds \tag{4.11}$$

where s is the surface 'visible' at P, $\vec{r}$ is the position vector of surface element $ds \equiv d^2r$ and $\vec{n}$ is the normal unit vector at ds.

If the average solid angle subtended by a detector with respect to an extended source distribution is to be calculated then the above expression must also be integrated over the source volume v. (where $dv \equiv d^3r_P$)

$$\Omega_{av} = \frac{\int_v \int_s \frac{\vec{n} \cdot (\vec{r} - \vec{r}_P)}{|\vec{r} - \vec{r}_P|^3} ds dv}{\int_v dv} \tag{4.12}$$

The simplest approach to this problem lies in a 'hit or miss' Monte Carlo integral. Placing the source at the origin, random unit vectors $\vec{r}_I$ are generated isotropically and those events where the detector surface intersects the extension of the directed line $\vec{OI}$ are deemed to be 'hits'. The solid angle Ω is then given by

$$\Omega = 4\pi \frac{\Sigma hits}{\Sigma total} \tag{4.13}$$

The extension to a distributed source is straightforward, points A are randomly chosen within the source volume and vectors $\vec{AI}$ are generated isotropically with respect to A.

This procedure results in a solid angle calculated in the laboratory frame. To evaluate the c.m.s. solid angle subtended by the detector surface it is necessary to regard the isotropic distribution as being produced in the centre of mass system and then perform a Lorentz transformation into the laboratory

frame. In order to do this it is necessary to consider the kinematics of a particular reaction, in this case the $D(\gamma,p)n$ reaction.

The Event Generator

The detector acceptance and efficiency calculations require a source of test particles produced with an isotropic distribution in the centre of mass system and with the angle-energy relationship of $D(\gamma,p)$ photoprotons.

The isotropic distribution of test trajectories is produced by randomly choosing $\cos\theta$ in the range $-1 \rightarrow 1$ and ϕ in the range $0 \rightarrow 2\pi$.

The velocity of the c.m.s. in the lab frame is β', given by:

$$\beta' = \frac{k_\gamma}{k_\gamma + M_D} \tag{4.14}$$

If the proton has momentum p_{cm} and direction θ_{cm} in the c.m.s. then it's laboratory scattering angle θ_{lab} is given by:

$$\tan\theta_{lab} = \frac{p_{cm}\sin\theta_{cm}}{\gamma' p_{cm} cos\,\theta_{cm} + \beta'\gamma' E_{cm}} \tag{4.15}$$

The proton energy E_{cm} is given by

$$E_{cm} = \frac{s + m_p^2 - m_n^2}{2\sqrt{s}} \tag{4.16}$$

where $\sqrt{s}$ is the total c.m.s. energy. s is given by

$$s = (k_\gamma + M_D)^2 - k_\gamma^2$$

The proton energy in the lab frame is calculated as follows.

for $0 < \theta_{lab} \leq 90\,\mathrm{deg}$

$$E_{lab} = \frac{B - \sqrt{D}}{2A} - m_p \tag{4.17}$$

for $90 < \theta_{lab} < 180\,\mathrm{deg}$

$$E_{lab} = \frac{B + \sqrt{D}}{2A} - m_p \tag{4.18}$$

where

$$A = (k_\gamma \cos\theta_{lab})^2 - (k_\gamma + M_D)^2$$

$$B = (k_\gamma + M_D)(m_n^2 - m_p^2 - M_D^2 - 2k_\gamma M_D)$$

$$C = 4k_\gamma^2 m_p^2 \cos^2\theta_{lab} + (m_n^2 - m_p^2 - M_D^2 - 2k_\gamma M_D)$$

$$D = B^2 + AC$$

Detector and Track Geometry

This section describes the formalism used for defining the experimental geometry and for tracking particles through detector elements. It is used for both the detector acceptance calculation described above and for the detector efficiency calculation which follows.

Particle tracks are defined by the co-ordinates of their point of origin and by a unit vector which gives the direction of flight.

Cuboidal detector volumes ('boxes') are defined by the co-ordinates of their eight vertices. Initially their position is given with respect to an origin at the bottom left-hand front corner of the 'box'. The box is moved to its correct laboratory position by means of a translation and subsequent rotation of its co-ordinate system.

The six planar faces of a box are defined by a vector normal to the plane and by one point contained within the plane. Depending on the orientation of the box with respect to the target each face is defined to be a particle input

face or a particle output face, and the direction vector of the plane is given to be positive in the direction of particle travel. There will usually be only one input face, although there may be as many as three. The normal vector is constructed from the vector product of two vectors corresponding to the directions of the edges of the box. These edge vectors are in turn given by the difference between the position vectors of two vertices. It is also necessary to define the area of each plane which corresponds to the face of the detector.

The tracking routine first checks for a hit on an input face of the detector and, if one is found, then searches for an exit point on one of the the output faces. If a hit is found then the tracking routine sets a logical variable HIT to be .TRUE. and passes the particle entrance and exit co-ordinates (transformed back to the proper frame of the detector) to the detector signal simulation routine.

Definitions

The following results are used in the tracking algorithm.

Parametric Equation of a Line

The line which passes through the point with position vector $\vec{A} = (a, b, c)$ and which has the direction vector $\vec{u} = \{\alpha, \beta, \gamma\}$ is defined by the following parametric equations.

$$\frac{x-a}{\alpha} = \frac{y-b}{\beta} = \frac{z-c}{\gamma} (= t) \tag{4.19}$$

where t is the parameter value corresponding to the point (x, y, z).

Scalar Equation of a Plane

The plane containing the point with position vector $\vec{P} = (l, m, n)$ and for which the normal direction is defined by the vector $\vec{n} = \{\lambda, \mu, \nu\}$ is defined by the following equation.

$$\lambda x + \mu y + \nu z = \lambda l + \mu m + \nu n (= d) \tag{4.20}$$

where d is a constant whose value identifies a particular member of a set of parallel planes.

Intersection of a Line and Plane

The parameter value t at which the a line and a plane intersect is given by, in the above notation:

$$t = \frac{\vec{n} \cdot \vec{P} - \vec{n} \cdot \vec{A}}{\vec{n} \cdot \vec{u}} \tag{4.21}$$

In the context of a particle track with a direction, one may ensure that the particle is heading towards the plane by checking that the scalar product $\vec{n} \cdot \vec{u}$ is positive definite.

4.5 Detector Response and Efficiency

The acceptance calculation described above determines whether the emitted particle hits the front face of the detector. However it does not automatically follow that the particle triggers the detector and produces a decipherable signal. The response of the detector to incident radiation depends on the detector geometry and composition as well as the particle type, energy and specific energy-loss characteristics. To understand fully the behaviour of the

system in a particular set of experimental circumstances it is also necessary to recreate approximately the angle and energy distribution of the reaction yield which is to be measured.

The main features of the simulation are as follows.

- Track particle through detector system.
- Calculate energy loss in target cell and ΔE strip.
- Within each E block traversed, follow the track in small steps $\vec{x} \rightarrow \vec{x} + \Delta\vec{x}$. At each step:
  - Test for nuclear reaction induced by particle while traversing Δx and calculate reaction Q value, recoil etc.
  - Calculate Bethe-Bloch energy loss ΔE while traversing Δx.
  - Calculate scintillation light output ΔL associated with ΔE.
  - Correct for (position dependent) light collection efficiency for source at $\vec{x}$.
  - Increment signal collected in E element $L \rightarrow L + \Delta L$
  - Decrement residual particle energy $E \rightarrow E - \Delta E(-Q)$
  - Transport particle to point $\vec{x} + \Delta\vec{x}$.
  - Test for exit from block.
- Test for hardware trigger from each E block passed through.
- Calculate centroid of distribution of light produced in each block. return average of centroids as x co-ordinate of event. (fold experimental resolutions into calculated x and y co-ordinates)

- Sum signals and calibrate in terms of proton energy.

Bethe-Bloch energy losses are calculated from range energy data which are interpolated from tables [61]. If the initial energy is E_0 corresponding to a range R_0 then the energy ΔE lost in Δx of material is given by,

$$\Delta E = E_0 - E(R = R_0 - \Delta x) \tag{4.22}$$

Since the tabulated function $R(E)$ is monotonic it is readily inverted and interpolated to give $E(R)$.

The problem of the inelastic reactions undergone by protons in scintillation detectors has been studied previously by Measday and Richard-Serre [62]. This work incorporated tabulated cross-sections for the most probable interactions of protons in carbon and this data was used as input to the present calculation. The results of [62] were not used directly because the present requirement is for a more complete detector response simulation applied to a specific experimental configuration.

The reactions considered were $^{12}C(p,\gamma)^{12}C^*$, $^{12}C(p,\alpha)X$ and $^{12}C(p,n)X$. The energy corresponding to the reaction Q value was considered lost, as was the recoil of heavy residuals because of the nonlinearity in scintillation light output. This also severely degraded the light produced by outgoing α particles. the interaction lengths of the emitted γ rays and neutrons is large compared to the size of the detector elements and so their further interaction was neglected. It was possible to compare the results of this calculation with that of [62] by 'switching off' the other effects in the calculation. By doing so it was possible to reproduce the Measday results. These stated that the fraction of protons whose signal is degraded by more than 10 MeV ranges from 2% at 35 MeV to 11% at 104 MeV .

For non-relativistic charged particles the production of scintillation light is not a linear function of energy deposition . The rate of light production along a particle track is given by the following semi-empirical relation. [63]

$$\frac{dL}{dr} = \frac{\frac{dE}{dr}}{1 + C\frac{dE}{dr}} \tag{4.23}$$

Where C is given by $9.5 \times 10^{-3} g\,\mathrm{cm}^2\mathrm{MeV}^{-1}$ for NE102 plastic scintillator which has the composition $CH_{1.105}$.The stopping power may be parameterised as follows, [64]

$$\frac{dE}{dr} = Br^{-0.448} \simeq Br^{-1/2} \tag{4.24}$$

where for protons $B = 17.91$ MeV $(g\,\mathrm{cm}^{-2})^{-1/2}$ and for α particles, $B = 67.76$ MeV $(g\,\mathrm{cm}^{-2})^{-1/2}$.

Whence:

$$\frac{L}{E} = 1 - \frac{2CB^2}{E} \ln\left[1 + \frac{E}{2CB^2}\right] \tag{4.25}$$

defining E_0 as $2CB^2$ and X as E/E_0 this becomes

$$\frac{L}{E} = 1 - \frac{\ln(1+x)}{x} \tag{4.26}$$

where E_0 is 6.1 MeV (protons) or 87.1 MeV (α particles). Since the calculation follows the particle track in small steps the formula is used in differential form, i.e. ΔL corresponding to ΔE is given by

$$\Delta L = L(E + \Delta E) - L(E) \tag{4.27}$$

The above expression has not been cast in absolute units, however it may be taken as giving the light output relative to electrons of the same energy. The light output for electrons will be linear since the equivalent x value will be very large.

The efficiency with which the photomultiplier tubes collect the emitted light varies as a function of the position of the source within the block. A separate Monte Carlo code PHOTON [65] was used to calculate the light collection efficiency on a 1 cm^3 lattice throughout the block. The program operates by tracking a large number of isotropically emitted photons through the block and calculating the fraction that reach the face of a photomultiplier tube at one or other end, allowing for absorption in the volume and reflection or transmission at the surfaces . The incremental signal produced at each step on the track was multiplied by the efficiency factor corresponding to the nearest lattice point. The light collection calculation is time consuming ($\sim$ 10 minutes per lattice point) and so the lattice data was prepared in advance and read in from a separate file at run time.

In the actual experiment the hardware trigger thresholds on the E blocks were set at pulse heights equivalent to between 5 and 10 MeV electron energy. The Monte Carlo calculation automatically produces signals in terms of equivalent electron energy (MeV_{ee}) and the Monte Carlo trigger threshold was set at 7 MeV_{ee}. This reproduced the observed effective proton threshold of $\sim$ 28 MeV . (see Chapter 3).

4.6 Results

The detector simulation produces as output the x and y co-ordinates of the event in the proton detector and the pulse heights recorded in each E block. This is the input required by the data analysis routines used with the real experimental data (see Chapter 4) and so the Monte Carlo data analysis proceeds along identical lines using the same routines for angle and energy calibration,

event selection and data binning.

The efficiency calculation works by simulating a $D(\gamma,p)$ experiment where the model 'cross-section' has been assumed to be isotropic in the centre-of-mass system and where every photon produces a reaction. The detector efficiency for a given angle-energy bin is then given by

$$\varepsilon = \frac{4\pi}{\Delta\Omega}\frac{Y}{\Phi} \tag{4.28}$$

where Y is the event weight accepted by the hardware and software conditions, Φ is the total event weight generated by the program and $\Delta\Omega$ is the nominal solid angle subtended by the software defined $\theta - \phi$ bin. If the detector is perfectly efficient and if the acceptance of the data bin is given by the nominal solid angle, then $\varepsilon \equiv 1$. This can be checked by switching off the detector response routines and using a point target. In practice the efficiencies ε are usually < 1. Exceptionally, where a position calibration nonlinearity effect puts too many events into a data bin, the net efficiency could exceed unity.

The overall structure of the program is shown in figure 4.3. Events are generated with a weighing factor and the total event weight integrated throughout the experiment. At each subsequent stage in the event history, some events are accepted and the others rejected. The accepted events are totalled at each stage. 7 running totals, labelled $\Sigma_{1,7}$, are maintained. These are defined as follows.

Σ_1 : Photon weight

Σ_2 : Photon weight after collimator

Σ_3 : Photon weight $\times$ target thickness $\rho(x,y)$ ($\equiv$ event weight)

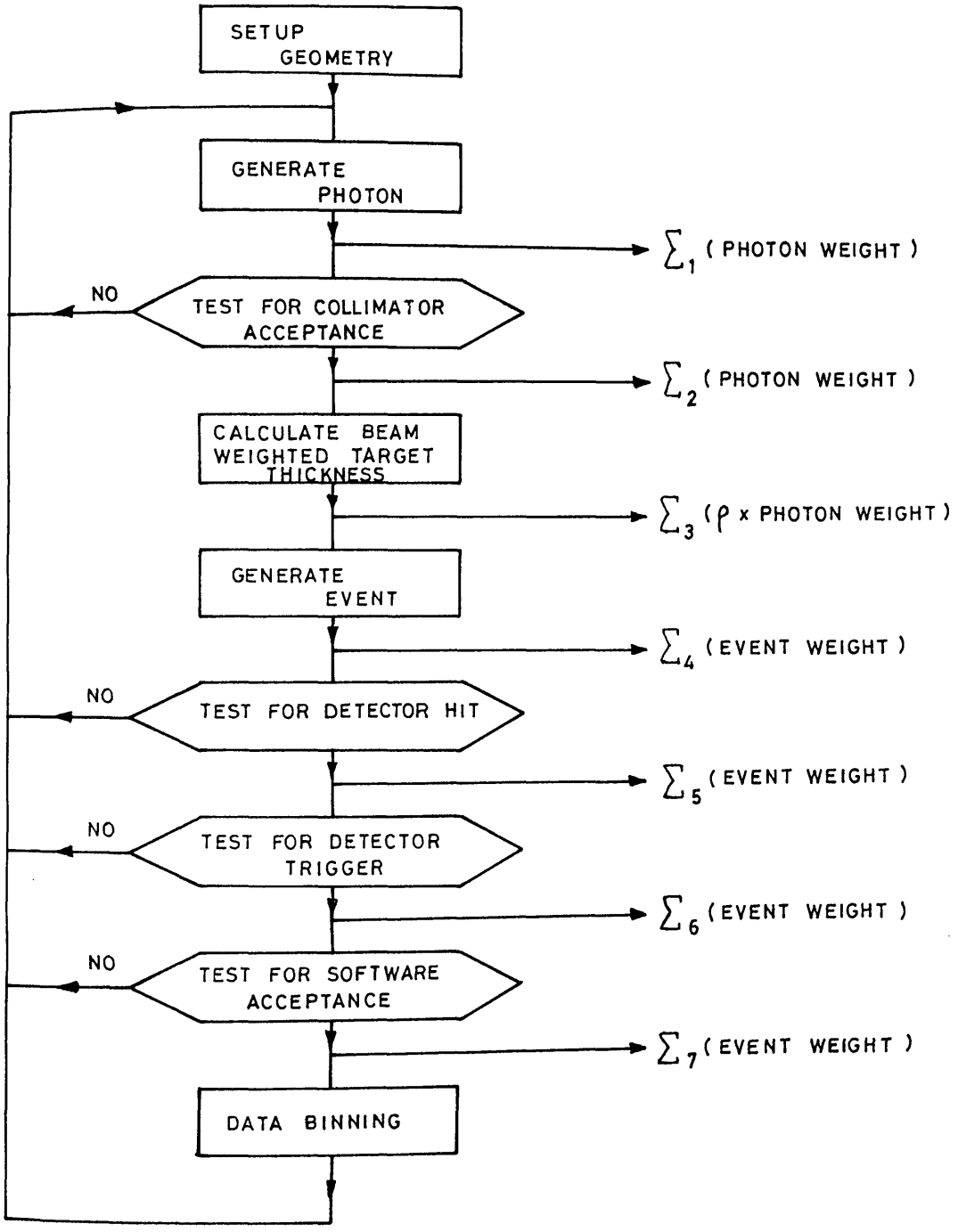

Figure 4.3: *Structure of the Monte Carlo Simulation*

Σ_4 : Event weight

Σ_5 : Geometrically accepted event weight

Σ_6 : Event weight after hardware trigger

Σ_7 : Event weight after software trigger

These totals are used to calculate global normalisation factors such as tagging efficiency and effective target thickness. They also provide average numbers for the efficiency at various stages of the calculation in addition to the histogram of finally accepted event weights which provides the efficiency corrections for each data bin. The quantities calculated are as follows

Σ_2/Σ_1: Tagging efficiency ϵ_τ

Σ_3/Σ_2: Effective target thickness ρ_{eff}

Σ_5/Σ_4: Total solid angle

Σ_6/Σ_5: Hardware trigger efficiency

Σ_7/Σ_6: Software efficiency

In order to obtain a measure of the uncertainties of the calculated correction factors the running time of the program is divided into 10 parts and 10 values of each quantity are calculated. The mean and standard deviation of each set of ten values are calculated and the estimated uncertainty returned as $\frac{\sigma}{\sqrt{10}}$.

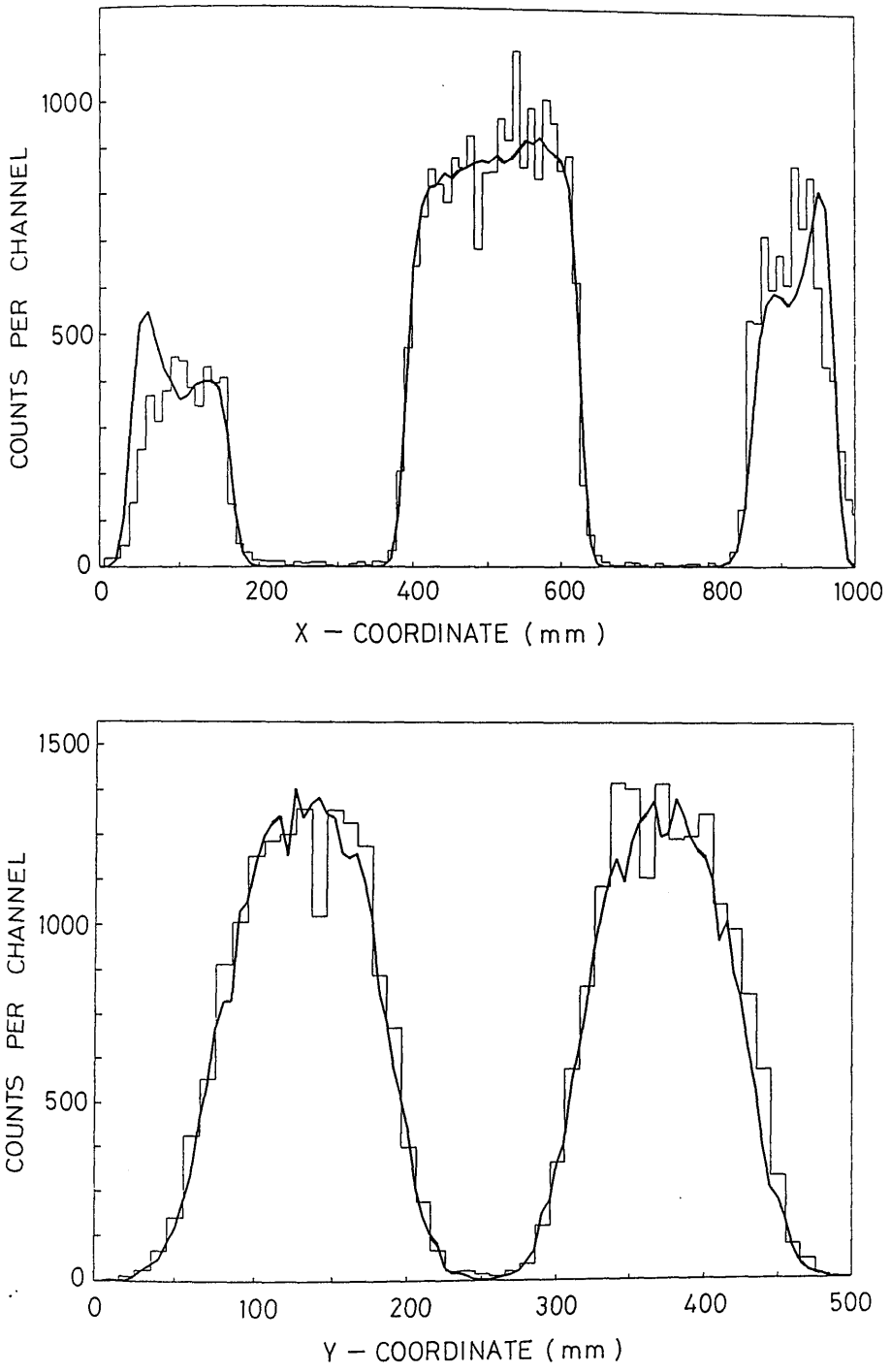

Figure 4.4: *(a) Prediction of horizontal position response. (b) Prediction of vertical position response.*

Position Response Predictions

The Monte Carlo code can be used to reproduce experimental spectra and this has proved useful in interpreting the data used to establish the x and y position calibrations for the proton detector. The physical edges of the detector elements can be used as reference points in determining the absolute scale of the $x-y$ reconstruction but the interpretation of the apparent position of these landmarks requires a detailed model of the detector response.

Figure 4.4.(a) shows the reconstructed position spectrum in an E detector where only those events passing through the 1st,3rd and 5th ΔE strip have been selected. The heavy continuous line represents the Monte Carlo prediction and the histogram the experimental result. The event position is given by the difference in arrival times of the light signal at either end of the E block as described in section 3.3. A linear time-difference to position relationship was used to calibrate the detector. A similar linear position reconstruction routine provided a Monte Carlo position spectrum consistent with experiment to $\pm$1cm over the central $\sim$ 70cm of the block. At the extreme ends however the linear prediction fails. Figure 4.4 (a) was obtained by introducing a nonlinearity into the Monte Carlo position reconstruction to simulate the anomalous light collection behaviour which occurs close to the photomultiplier tubes. The section from 10 – 90cm remains linear but the 10cm at each end were smoothly telescoped into 6.5cm.

Figure 4.4 (b) shows a similar plot for a ΔE detector where only events triggering E blocks 1 and 3 have been selected. In this case the uncertainty in interpreting the experimental data lies in the efficiency of the corners of the E blocks for the detection of protons which pass through without stopping.

The outside edges of the two peaks seen in figure 4.4 (b) are determined by the protons which clip the edges of the outer E blocks while still depositing enough energy to trigger the detector whereas the position of the inner edges is determined by those protons which pass through the middle block *without* causing it to trigger. Again the data and prediction are consistent to $\pm$1cm.

Pulse Height Response

Figure 4.5 shows the results of simulated $D(\gamma,p)$ experiments at 55 MeV , 80 MeV and 140 MeV photon energies. The scatter plot depicts the original proton energy calculated from photodisintegration kinematics plotted against the recorded pulse height signal quoted in MeV_{ee}. The response is linear at the energy of the present experiment (E_γ = 140MeV). However at 80 MeV the response to the lower energy protons is degraded as a result of the combined effect of energy losses outwith the E blocks and nonlinear light production within the scintillator. The proton yield from the 55 MeV experiment lies almost entirely below a threshhold of 7 MeV_{ee} .This corresponds to an initial energy of $\sim$ 30 MeV which is in agreement with experimental experience.[66]

Figure 4.6 is an effective proton pulse height spectrum obtained from $D(\gamma,p)$ data taken over a range of emission angles and photon energies by subtracting the (calibrated) energy measured in the detector from that calculated from the photodisintegration kinematics. The main peak therefore appears at 0 MeV in the figure. The long low energy tail observed below the full energy peak is caused partially by edge effects in the E detectors and partially by the occurrence of inelastic nuclear reactions between the incident protons and the carbon nuclei in the detector material. The width of the

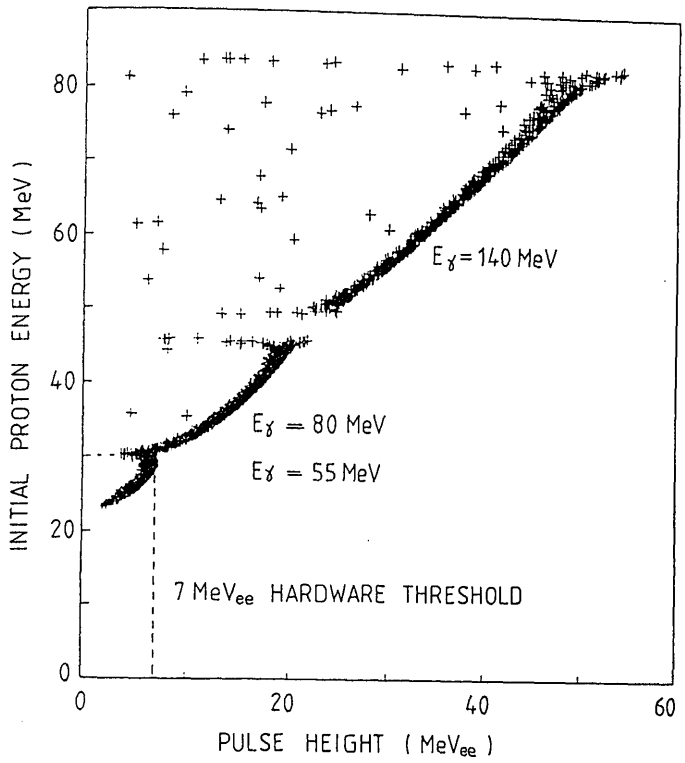

Figure 4.5: *Initial proton energy vs. pulse height for* $E_\gamma = 55, 80, 140$ MeV

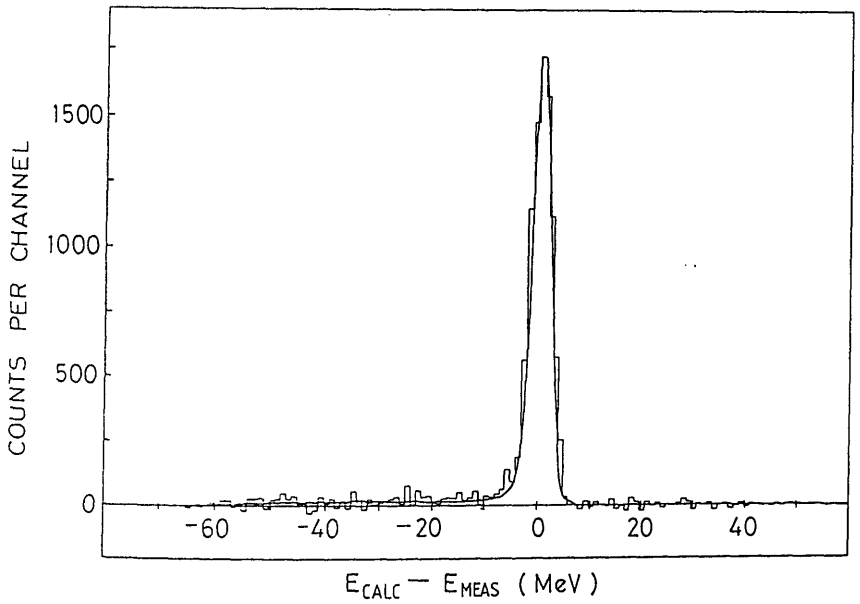

Figure 4.6: $E_{calc} - E_{calib}$ *for* $E_\gamma = 130 - 155$ MeV . *The smooth line is the Monte Carlo prediction of the pulse height response of the detector system.*

peak is a product of the pulse height response of the detector, kinematic reconstruction errors due to finite position resolution, and energy losses of the protons in the liquid deuterium target and the ΔE strips.

Accuracy of the Results

The errors inherent in the random sampling process are very small, since it is possible to average the results over a large number of Monte Carlo histories. The errors due to the approximations of the model are harder to quantify. The treatment of the purely geometric effects should be reliable since it was possible to perform a detailed calculation. Furthermore the good agreement obtained for both the pulse height and the position response of the detector gives cause for confidence in the model. The largest uncertainty must be due to the effects of inelastic nuclear interactions in the scintillator since these represent the largest single efficiency correction. An assessment of the various sources of systematic error, including those associated with the Monte Carlo calculation, is made in section 5.6.6

Chapter 5

Data Analysis

5.1 Data Reduction

The data stored during the experiment consisted of those events where a detector signal coincided with signals from one or more focal plane detector (FPD) channels. The most basic requirement for the analysis of tagged photon data is that the photon energy be identifiable and so the first task in the data reduction process is to reject any event where multiple ladder hits makes the photon energy and the detector-FPD coincidence timing ambiguous. The data may then be partitioned into a prompt coincidence subset containing all the genuine tagging coincidences plus some random coincidences and an equivalent random background subset which will be used to provide an appropriate correction to the data. At this stage the raw experimental signals, which take the form of TDC and ADC information, must be calibrated in terms of the physical observables of the experiment, i.e. the energies and trajectories of the particles. It is then possible to reject a large part of those events which do not correspond to the products of a $D(\gamma, p)$ reaction. The data is histogrammed in the form of angular distributions and then background corrections are made using the random coincidence subset. Corrections for tagged background originating from the cell windows and the beam line are made using data taken with an empty target cell. Finally the angular distributions are normalised to produce angular differential cross-sections.

5.1.1 Multiple Ladder Coincidences

Rate Effects

In order to determine unambiguously the energy of the photon which induced a particular reaction it is necessary to identify the ladder channel which registered a tagging electron. The timing of the coincidence between the tagging electron and the reaction trigger is registered in a TDC which is started by the X-trigger signal and stopped by the ladder signal. The identity of the channel is recorded in one of six pattern units. The effective range of the TDC is restricted by the width of the X-trigger coincidence pulse to $\sim$ 50 ns. A typical TDC spectrum is shown in figure 5.1 . The 2 peaks in the middle of the range correspond to the arrival of protons and electrons produced by tagged photons. The electrons are all relativistic and arrive early forming a peak which is widened only by the range of flight paths and the intrinsic time resolution of the apparatus. For example, the flight time for electrons over $\sim$ 0.5 metres will be $\sim$ 1.5 ns. The flight time for protons will vary from 7.2 ns to 3.1 ns for energies in the range 50 – 100 MeV . There is also a significant low energy (i.e. long flight time) tail on the proton peak which is produced mainly by low energy background events involving heavier nuclei in the cell windows etc. In figure 5.1 the electron peak lies on the right because the TDC is stopped by the ladder. The peak at the left hand end is an artifact of the coincidence electronics. In addition to the peaks there is also a smooth background of random coincidences underneath. Since the tagging electrons arrive randomly it is possible that more than one will be registered within a gate period. This has some undesirable consequences. Firstly it introduces an ambiguity into the determination of the photon energy and secondly it

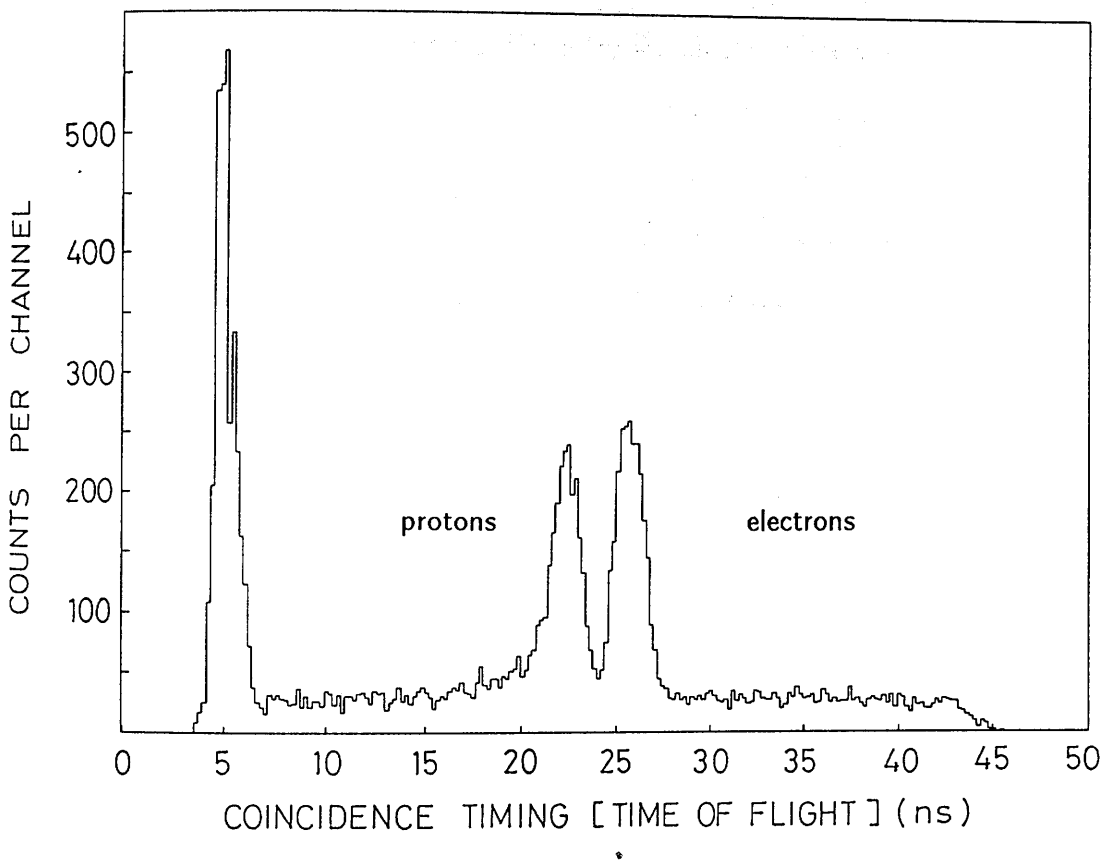

Figure 5.1: *Sample of coincidence time spectrum. (Time of flight spectrum)*

complicates the subtraction of the random background in two ways. If the two or more channels that fire are served by one ladder TDC then only one electron arrival time can be recorded, corresponding to the first ladder 'stop' pulse to arrive and so the event cannot be ascribed to the 'prompt' region or to a 'random' region of the TDC range. Furthermore, it can be shown (Appendix E) that if there is a significant probability of more than one random electron arriving in a gate width then the timing distribution of randoms under the prompt peak has an exponential slope. Alternatively, one can select for analysis only those events where a single ladder channel fired within the gate time. This removes the energy and real/random ambiguities and has the added advantage that the random background is now flat (appendix E). The disadvantage is that some fraction of the tagged events will be discarded. For the purposes of an absolute cross-section this fraction must be evaluated and an appropriate correction made. The full details of the analysis of the focal plane detector (FPD) multiplicity spectrum are given in appendix E. The probability that a tagging electron is accompanied by one or more additional uncorrelated electrons is given in terms of the Poisson distribution by

$$\sum_{n=1}^{\infty} P(n, N\tau) = 1 - P(0, N\tau) = 1 - e^{-N\tau} \tag{5.1}$$

where $P(n, N\tau)$ is the probability that n electrons register in a gate time τ sec given that the mean rate is N sec^{-1} . For example, in a typical case of a 60 ns gate width and a flux of 10^7 sec^{-1} the probability that at least one random electron accompanies a true tagging electron is 0.45. If each FPD channel could be treated independently then the effective rate would be $\sim 10^5$ sec^{-1} and the chance of a double hit would be negligible. However the smallest group of FPD channels which can be treated independently is the group fanned into a particular TDC. The effective electron beam rate in the

case of the present experiment is therefore $\sim$ 1.6×10^6 sec^{-1} corresponding to a multiple hit probability of 9%.

Geometric Effects

The construction of the FPD, which is described in chapter 3, provides for a slightly greater than 50 % overlap of each scintillator strip with its neighbour. Therefore each channel (2 adjacent scintillators) overlaps the next one slightly and so a single electron passing through the focal plane can trigger 2 channels (i.e. 3 adjacent scintillators). A similar effect is produced by δ electrons ejected from the detector strips which can cause double or even triple triggering in consecutive channels. These geometric effects must be corrected prior to correcting the statistical multiple firings. The approach taken has been to construct a 'corrected' pattern spectrum by reassigning all neighbouring multiple hits as single hits. The error involved in this procedure is small. For example, the fraction of genuinely random neighbouring doubles is $\frac{2}{92}$ of the total random double rate, which is itself $5 - 10$ % of the total rate. By comparison, the observed geometric double rate, measured at very low beam intensities where random coincidences are a negligible effect, is $\sim$ 10 % of the total rate.

The procedure adopted for the selection of single hit data was as follows. Events were accepted if there was exactly 1 'corrected' FPD hit in the group of channels served by a single TDC. In this way six subsets of reduced data were obtained, each pertaining to one of the six focal plane TDCs. Thus, although a particular event may be selected for inclusion in any number of subsets from 0 to 6 no ambiguity remains concerning the photon energy or

coincidence timing since each data subset is analysed independently. Problems of 'double counting' do not arise because each event can only correspond to 0 or 1 correlated tagging electrons and after an appropriate random coincidence correction only the tagged events are given weight.

5.1.2 Prompt and Random Events

No individual event can be said to have been caused by the absorption of a tagged photon. All that can be said with certainty is that a region of the TDC spectrum can be defined which contains all the prompt events as well as a background of random coincidences, and that the rest of the TDC spectrum contains only random events. In order to correct final results for the presence of random background it is necessary to perform analysis in parallel on two data subsets. One must contain the whole prompt region and the other should contain only random events. The event-by-event data analysis then proceeds identically in the two cases. The final step is to subtract the yield from the random background dataset from the yield derived from the prompt dataset. The weight given to events produced by untagged photons will cancel in the subtraction. To improve the statistical precision it is possible to use a random region which is longer (in TDC space) than the prompt region and then to perform the subtraction with an appropriate normalisation constant. The problem of normalisation is greatly simplified if the background distribution under the prompt peak is flat. This is the case if only single hit data is selected.(appendix E) For the above procedure to be applicable it is necessary that the character of the events produced by untagged photons is independent of the timing of the randomly coincident electron.

In the present analysis it has been found useful to combine the real/random data selection with the next stage of data reduction which involves the rejection of electron background. This is described below in section 5.3.2 .

5.2 Calibrations

5.2.1 Energy Calibration

The pulse height response of the detector system requires to be calibrated in terms of proton energy. This has been accomplished by reference to the fully determined two body kinematics of the $D(\gamma,p)n$ reaction. Figure 3.11 shows the correlation of the measured pulse height for deuteron photoprotons (after calibration) and the energy calculated from the known photon energy and proton emission angle. The calibration is assumed to have the linear form

$$E(\text{MeV }) = A_1(\text{MeV .ch}^{-1}).Q(\text{ch}) + A_0(\text{MeV }) \tag{5.2}$$

where A_0 and A_1 are calibration constants and Q is the pulse height signal derived from the geometric mean of the signals from the two ends of the detector Q_a and Q_b.

$$Q = \sqrt{Q_a.Q_b} \tag{5.3}$$

The offset constant A_0 is necessary for two reasons. The light produced in the last part of the proton track is proportionally less than that produced when the proton has higher energy (as described in chapter 4). This has the effect of displacing the total integrated pulse height downwards, such that the extrapolated zero of energy occurs at a negative pulse height. The other effect is the energy lost by the protons in the ΔE detectors. This is different for each proton energy and trajectory. For the present purpose, however, a

global correction was found to be adequate given the range of proton energies encountered at a given detector position. The total offsets used at forward, middle and backward angles were of the order of 20, 14 and 10 MeV .

The three E detectors were calibrated individually and in cases where two blocks fired the results were summed to produce a final energy. In these cases the offset constant should only be added for the second of the blocks which the proton passes through. It is assumed that two triggerings only occur when the particle enters the middle block (block E 2) and passes through it into the upper or lower block.(blocks E 1,3) Therefore the calibration formula is modified to be

$$E(\text{MeV }) = A_1(\text{E } 2).Q(\text{E } 2) + A_1(\text{E } 1,3).Q(\text{E } 1,3) + A_0(\text{E } 1,3) \qquad (5.4)$$

5.2.2 Position Calibration

The position calibrations were assumed to be linear and of the following form.

$$x(\text{mm}) = C_1(\text{mm.ch}^{-1}).(\text{ch}) + C_0(\text{mm}) \qquad (5.5)$$

The calibrations were calculated independently for each of the detector positions to allow for time variations in the TDCs and discriminators. In the horizontal direction there are also systematic variations at different proton detector angles. This is because higher energy protons penetrate to greater depths in the scintillator and therefore produce light with a different spatial distribution within the block. When the proton enters the block at an angle deviating significantly from the normal direction then this effect will alter the apparent horizontal co-ordinate of the proton track. It would have been impractical to repeat the full calibration measurement (described in chapter 3)

before each measurement. The procedure adopted was to adjust the calibration constants until the observed position spectra from a series of sample files corresponded to the Monte Carlo predictions.(chapter 4)

In cases where two E blocks triggered a tolerance condition was set such that the difference in reconstructed x position in the two blocks was to be less than 10 cm. If this condition was met then the average of the two x positions was returned as the horizontal co-ordinate. If all three blocks or the top and bottom blocks triggered then the event was probably caused by a random coincidence involving a cosmic ray and so was rejected. Events where more than two ΔE strips fired or where two non-adjacent strips fired were also rejected. Where two neighbouring strips fired the average position was calculated. Once again a 10cm tolerance condition was imposed. The final correction for the small number of events rejected by these conditions was negligible because they consisted almost entirely of atomic background events where electrons scattering at large angles in the scintillators produced anomalous signals.

5.3 Background Rejection

Prompt background processes may be divided into two classes. In the first place there is background resulting from photon interactions in the target cell windows, in the air along the photon beam path and in the collimators. Secondly, there will be atomic background emanating from the target itself. Background from sources other than the deuterium target itself can be corrected by subtracting the yield obtained from an empty cell. In contrast, the target-full atomic contamination must by rejected in event-by-event analysis.

Three methods have been used to separate protons and electrons. $\frac{dE}{dx}$ particle identification selects protons, both tagged and untagged. Time-of-flight data can be used to select prompt protons as described below, and kinematic reconstruction can be used to identify prompt protons issuing from $D(\gamma,p)n$ reactions. Severe cuts on the data must be made with caution. Although there are clearly visible loci corresponding to $D(\gamma,p)$ events in both the time-of-flight plot and the $\frac{dE}{dx}$ plot (figures 5.2,5.3) they will not contain 100 % of the events. If the proton underwent a nuclear reaction in the detector or passed through one corner of it without stopping then the combination of signals produced would remove the event from the $D(\gamma,p)$ loci. These events may have to be discarded eventually but it is important that it does not happen accidentally. The approach chosen was to apply a series of 'safe' cuts each of which would preserve all the foreground events while perhaps being individually insufficient to remove all the background. In combination, however, they would have the effect of selecting only the $D(\gamma,p)$ events.

5.3.1 dE/dx Electron Rejection

Figure 5.3 shows the sum of the ΔE signals plotted against the sum of the E detector signals. The $E-\Delta E$ cut already made in hardware is visible in the bottom left hand corner of the scatterplot. The analysis of other experiments performed at Mainz with similar apparatus has proceeded by performing tight cuts on the proton locus in similar plots where each of the 15 combinations of E and ΔE were selected separately to improve the definition of the proton locus.(see figure 3.8) . In the present case, because of the importance of the absolute cross-section determination, it was decided not to cut tightly underneath the visible proton region in figure 5.3 . Protons whose pulse height

signal is degraded will move out of the proton locus and into the electrons on this plot and conversely electrons which scatter through large angles will deposit more energy in the detector than would be normal and so could appear amongst the protons. The software $E - \Delta E$ cut finally chosen removed the dense region of low pulse height electrons visible in figure 5.3.

5.3.2 Combined Time of Flight Cut and Prompt/Random Cut

As described above the prompt region of the master coincidence TDC spectrum contains two peaks, one corresponding to electrons and one to protons. The structure of the T.o.F. spectrum is revealed in figure 5.2 which represents a scatter plot of pulse height vs. time of flight. The electrons produce a wide range of pulse heights but essentially the same flight time. On the other hand, the protons display a definite correlation between pulse height and flight time. It is also seen that the $D(\gamma, p)$ protons have a flight time/pulse height relationship different to that of the background. Figure 5.4 shows the first cut made on the data to remove the prompt electrons and the random 'spike' at the left hand end of the spectrum. The extent to which the electron background is eliminated by this cut is seen in figure 5.5 which may be compared to the raw data shown in figure 5.3. Examples of the prompt and random regions selected for analysis appear in figure 5.4. The sloping cuts were designed to preserve all the prompt proton events while minimising the random background underneath. They were obtained by performing a skew-transformation on the plane represented by figure 5.4 . The transformation has the form

$$\text{ToF} = \text{ToF} - \alpha \times \text{Pulse Height} \tag{5.6}$$

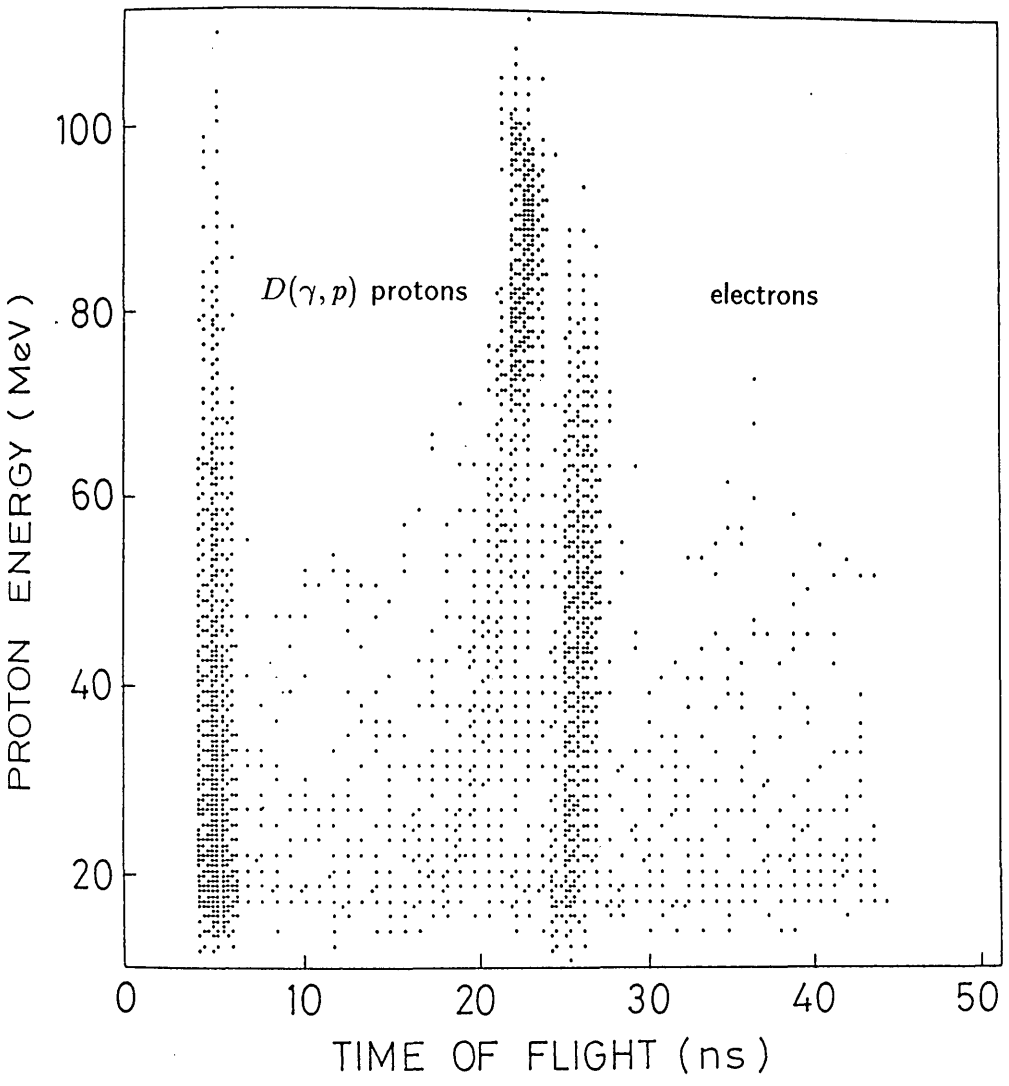

Figure 5.2: *Scatterplot of proton pulse height vs. Time of flight spectrum.*

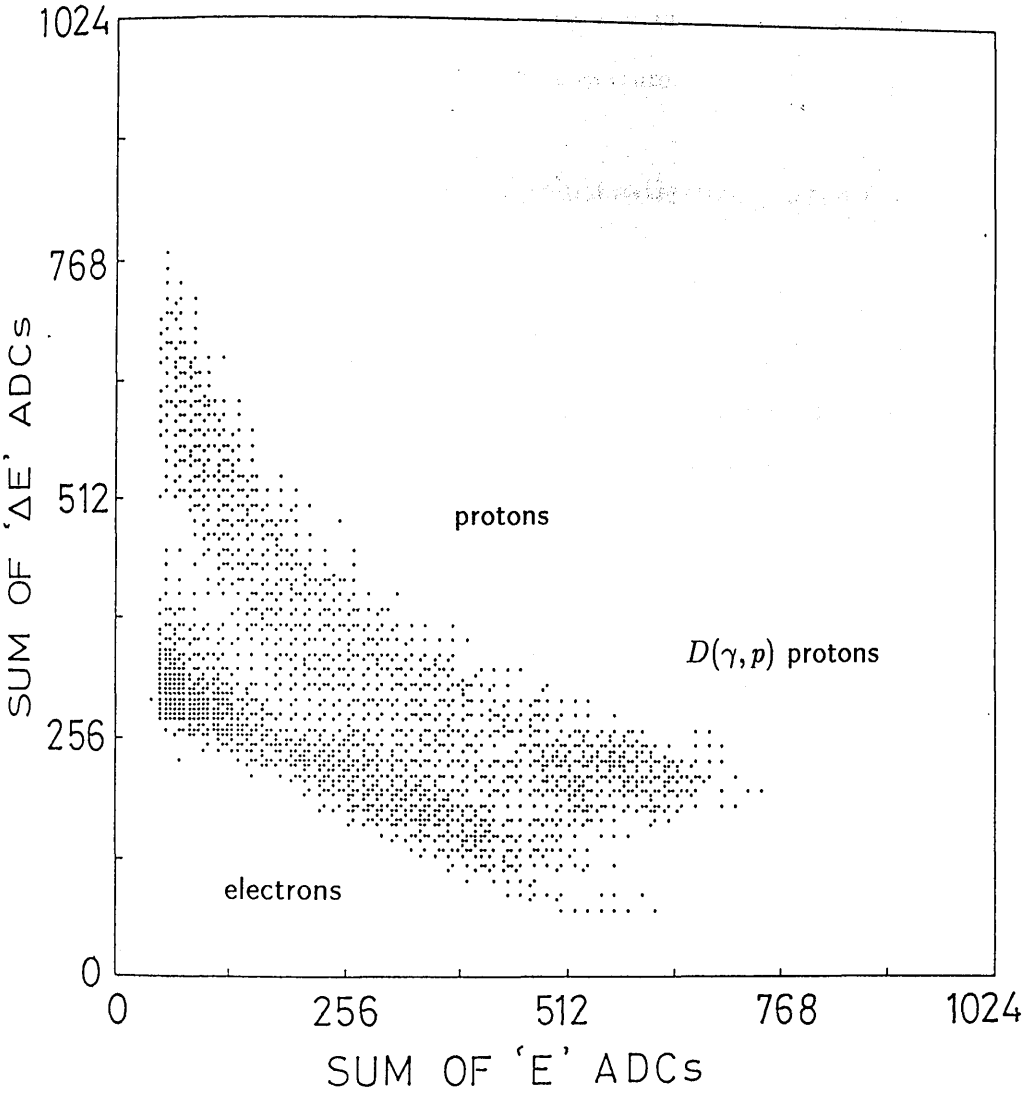

Figure 5.3: *Scatterplot of* ΔE *signal vs.* E *signal.*

Where α is a constant which sets the slope of the cut. This procedure has the effect of producing a transformed time of flight spectrum upon which normal one-dimensional cuts may be made. Future references to prompt and random time regions refer to this transformed spectrum.

5.3.3 Reconstruction of Photodisintegration Kinematics

The basic physical information recovered for each event consists of the pulse height signal calibrated in terms of energy, the particle emission angle and the tagged photon energy. Events which correspond to deuteron photodisintegrations induced by tagged photons have a definite relationship between the proton angle and energy. The calibrated proton energy should equal that calculated from the kinematic relations. Figure 5.6 shows the kinematic correlation displayed as the difference between the calculated energy and the measured energy.

In principle the spectrum shown after background subtraction in figure 5.6 (b) could be integrated as it stands to produce the final reaction yield. Unfortunately, however, the presence of the long tail of low energy events below the main peak adversely affects the statistical accuracy of the measurement because of the magnitude of the background subtraction in that region. It may also be possible that there is a systematic error in the normalisation of the subtracted yield. Furthermore, the small fraction of the electron background which is not vetoed by the previous cuts becomes significant at the most forward angles and contributes to the lower part of the tail. These sources of error can be avoided if one accepts the validity of the pulse height response model presented in chapter 4. For these reasons it was decided to apply a

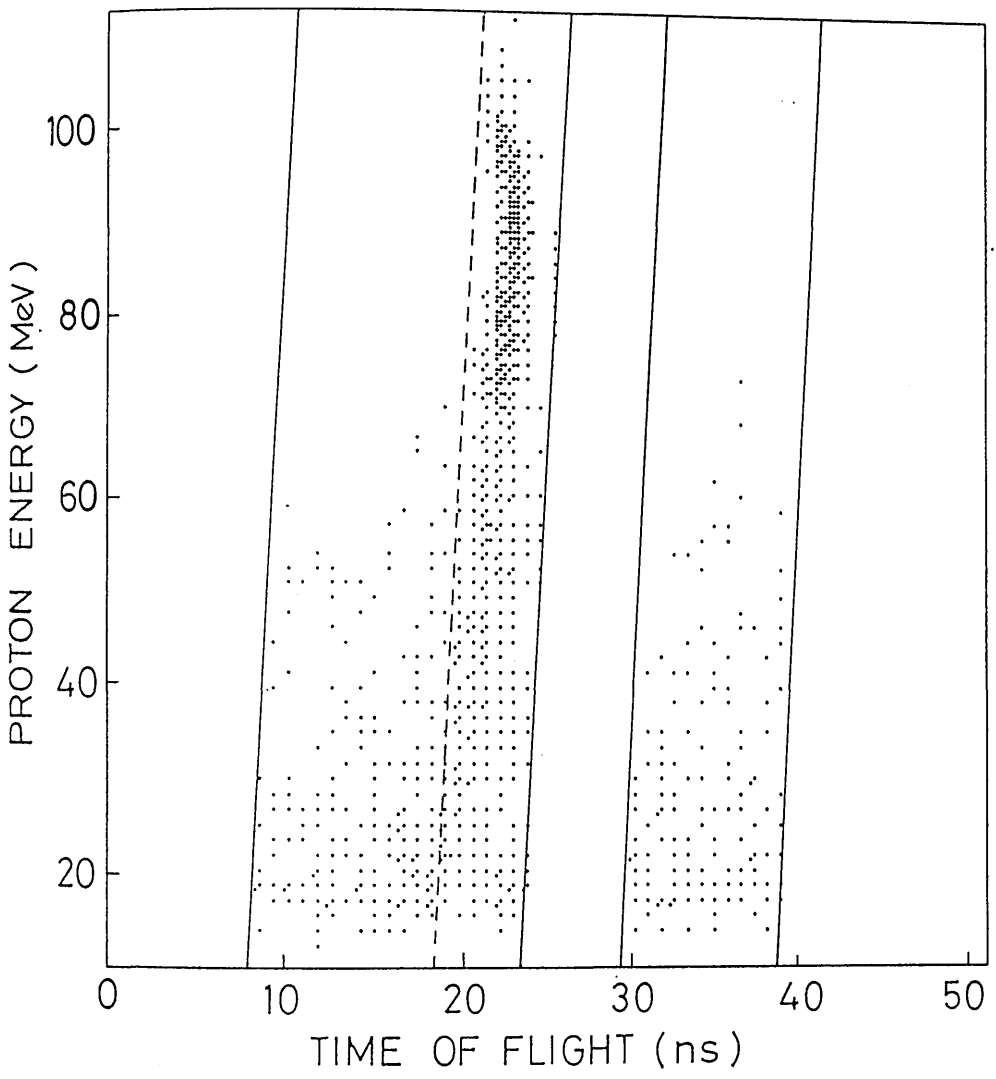

Figure 5.4: *Cuts used on the pulse height vs. T.o.F plot. Solid lines are the initial cuts, dashed line represents final prompt cut.*

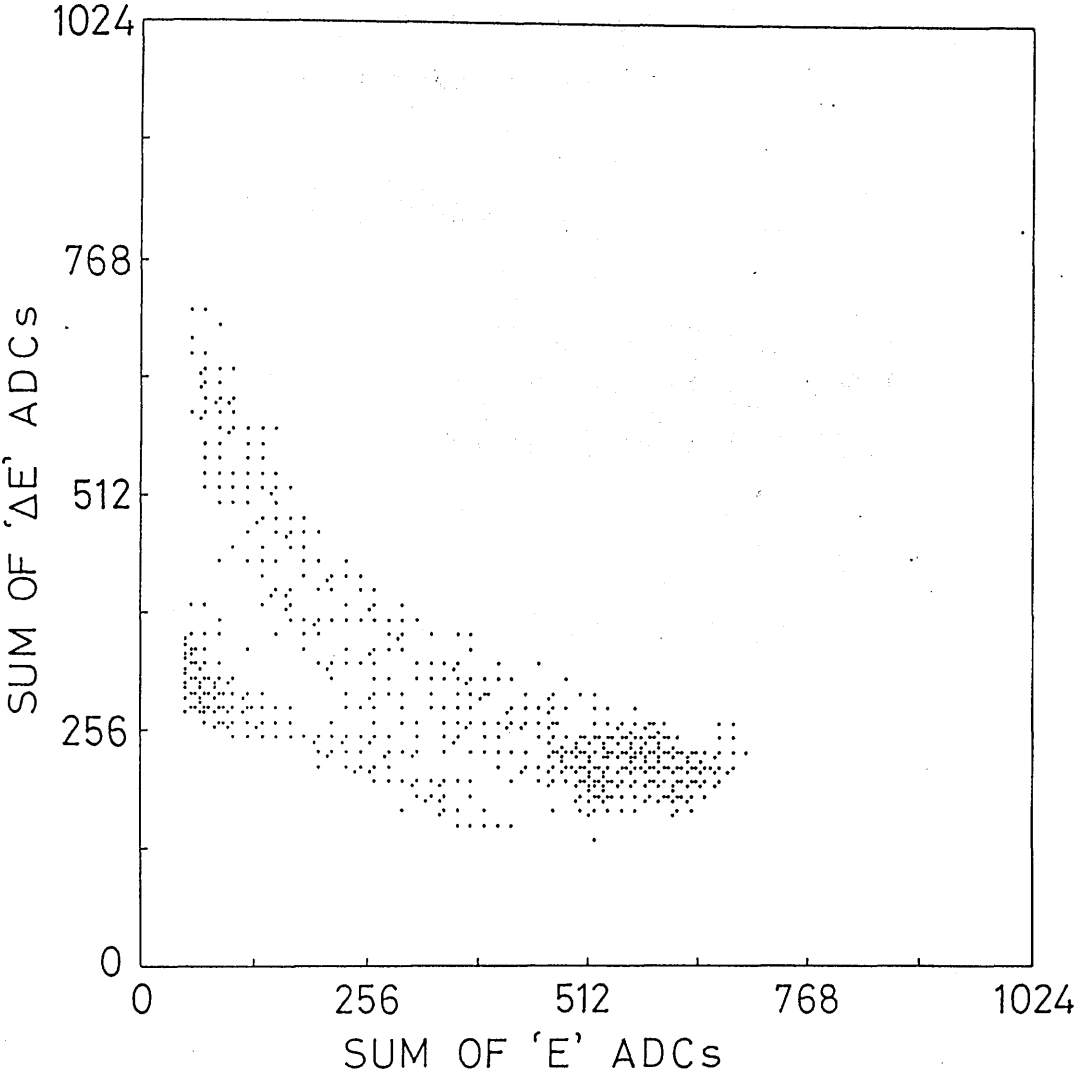

Figure 5.5: *E-dE plot after time of flight cut (solid lines in figure 5.4)*

cut at -10 MeV on figure 5.6 . The correction for the discarded events was then calculated from the Monte Carlo simulation. The magnitude of the calculated correction is consistent with the integral of the observed pulse height tail however the statistical precision is rather poor.

5.4 Data Binning

Six reduced data sets were created from each original raw data file, each one containing events with one coincident tagging electron in the appropriate FPD section. The selected events have an unambiguously tagged photon and a definite particle interaction in the proton detector with interpretable x and y co-ordinates. Each data set contained both prompt region and random region data. There were data sets for both target-full and target-empty runs.

The final data reduction and angle-energy binning now proceeded together. Two passes were made through each data file. The first pass selected events in a narrow time window around the prompt peak and the second pass accepted a random sample in a rather wider time region. The data was binned according to the proton emission angle, θ, in the centre of mass system, which was calculated from the observed laboratory angle and the known photon energy. The θ limits were $0, 10, 20 \ldots 180°$. The azimuthal limits (ϕ) were dependent on the detector orientation and were set differently for each θ bin at each detector orientation. The angular bins therefore formed rectangles in θ, ϕ space for which

$$d\Omega(\theta_1, \theta_2; \phi_1, \phi_2) = (\phi_2 - \phi_1)(\cos\theta_1 - \cos\theta_2) \tag{5.7}$$

The ϕ limits were designed to cut out the top and bottom edges of the proton detector where the detection efficiency was uncertain. The θ range was unre-

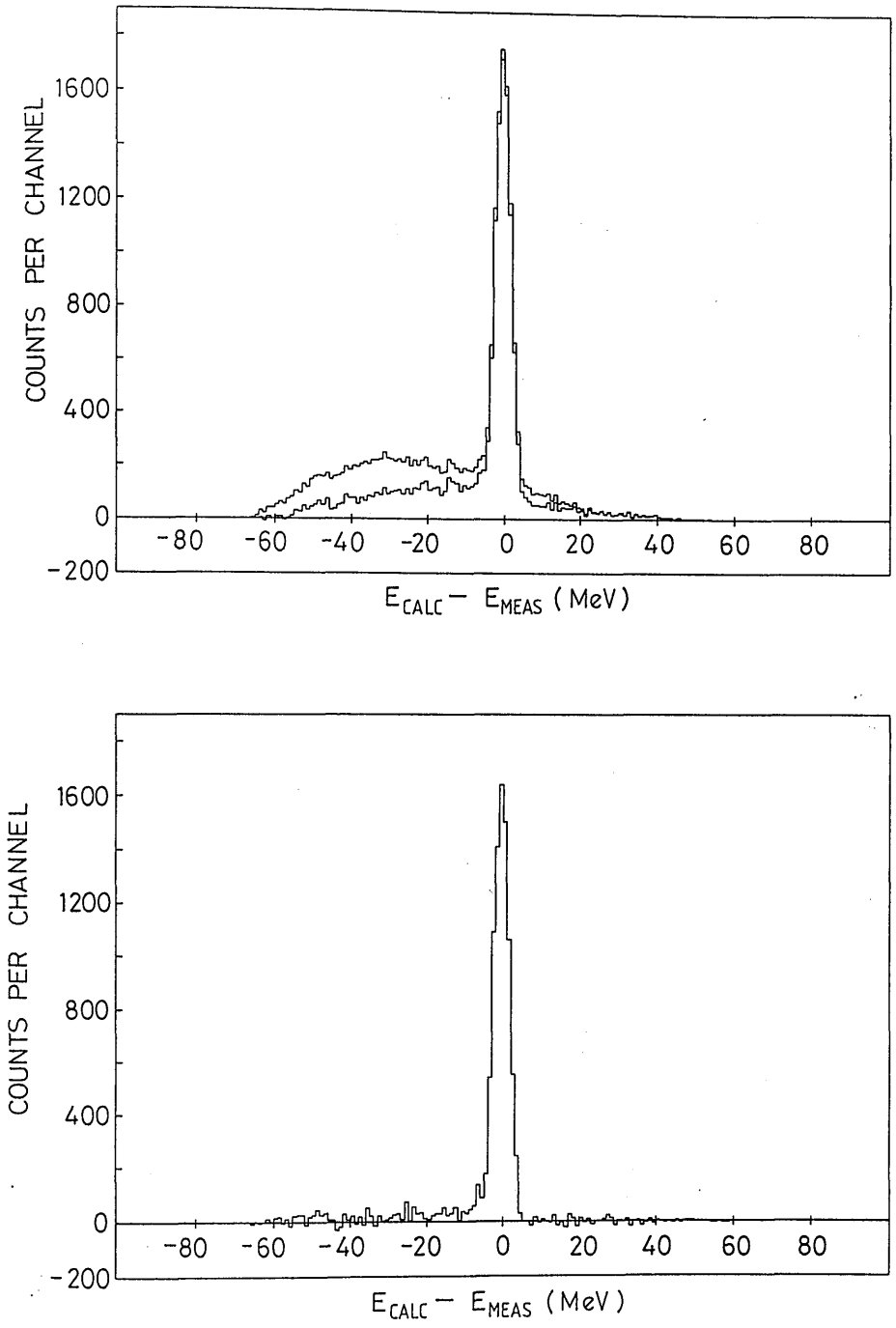

Figure 5.6: *Reconstruction of photodisintegration kinematics (E_{calc} - E_{meas}). (a) With and without random subtraction. (b) after background subtraction.*

stricted. It was, however, understood that the forward and backward edges of the detector would not generally correspond to the limits of an angle bin. The θ, ϕ rectangle described above does not, in fact, correspond to a sharply defined region of the proton detector surface. The edges are 'softened' by the variation in the energy of the tagged photons. The finite angular resolution of the system will also lead to smearing effects between neighbouring angular bins. These effects were incorporated into the Monte Carlo acceptance calculation.

The energy binning is done automatically, since the six ladder sections each cover a ~ 4 MeV range of photon energy. Two photon final energy bins were created by adding the subfiles in groups of three. Using the standard spectrometer magnet currents and an electron beam energy of 183.5 MeV the energy bins were calculated to be [67] 133.0 – 145.8 MeV and 145.8 – 158.3 MeV .

5.5 Background Subtraction

At this point in the analysis there were 12 angular distribution histograms corresponding to each original data file, 6 for the prompt events and 6 for the equivalent random samples. In addition, there were corresponding sets of histograms for the target empty files. The background subtraction is done by adding and subtracting the histograms with appropriate normalisation constants. If a histogram is labelled as $H(p, f, i, j)$ depending on whether it is prompt-p (random-r), full cell-f (empty-e), TDC i (1-6) and file j then the

subtraction procedure can be summarised as follows.

$$\sum_j \sum_{i=1}^{3} [H(p,f,i,j) - \alpha_i H(r,f,i,j)] - \beta \sum_{j'} \sum_{i=1}^{3} [H(p,e,i,j') - \alpha_i H(r,e,i,j')] \tag{5.8}$$

and similarly for TDCs 4-6. The α_i are given by the ratio of the lengths of the prompt and random regions defined on the spectrum of TDC i. The constant β is defined as the ratio of the total target-full electron flux to the total target-empty flux.

It was necessary to adopt a different procedure in order to treat the backward angle data. During the backward angle empty-target runs the tagging efficiency dropped by a factor of two. Inspection of the proton angular distributions also indicated that the the quality of the beam had been severely degraded and this data proved to be unusable. Some of the target-full data files were similarly affected. The remaining files were analysed in the standard fashion in order to produce kinematic correlation spectra similar to figure 5.6 a. The background under the peak was assumed to have a linear slope and a background subtraction figure was calculated. The spectrum integration was cut off at 10MeV below the peak and the Monte Carlo correction for the reaction tail added as in the previous case.

5.6 Normalisation

5.6.1 The Cross Section Formula

The yields obtained within angle-energy bins must be normalised with respect to solid angle, beam flux, target thickness and detector efficiency in order to produce the double differential cross-section $\frac{d^2\sigma}{d\Omega_p dE_\gamma}$. If the yield correspond-

ing to the datum point $\sigma(E_i, \theta_j)$ is defined as Y_{ij} then the cross-sections are defined as follows.

$$\sigma(E_i, \theta_j) = \frac{Y_{ij}\alpha_i\varepsilon_{ij}}{\varphi_i\epsilon_\tau^i\Delta\Omega_j\rho_N} \tag{5.9}$$

where

- φ_i is the electron flux corresponding to photons in energy band i.
- ϵ_τ^i is the tagging efficiency for photons in energy band i. (The photon flux is given by $\epsilon_\tau\varphi$)
- $\Delta\Omega_j$ is the nominal solid angle of the $\theta\phi$ bin j.
- ρ_N is the effective area-density of target nuclei.
- ε_{ij} is the Monte Carlo calculated detector efficiency and acceptance correction.
- α_i is the correction for events discarded because of multiple ladder firings.

5.6.2 Electron Flux

The electron flux is recorded on 12 free-running scalers. 6 scalers integrate the flux corresponding to TDC sections 1-3 (i.e. $E_\gamma = 145.8 - 158.3$MeV) and similarly 6 scalers record the flux for TDCs 4-6 .($E_\gamma = 133.0 - 145.8$MeV) The scaler input is divided down by a factor of 2^{19} to prevent overflows so the flux is given by

$$\varphi = \alpha_D 2^{19} \sum_{n=1}^{6} \text{scaler}(n) \tag{5.10}$$

Where α_D is a correction for dead time in the scalers. The ladder pulses are initially 12 ns long but dispersion in the signal cables results in their becoming

25 ns long at the scalers. This is comparable with the intrinsic dead time of the scalers which are rated at 40 MHz. For a given dead time τ_D the observed rate k and the true rate m are related as follows

$$\frac{1}{\alpha_D} \equiv \frac{k}{m} = e^{-m\tau_D} \tag{5.11}$$

Using $\tau_D = 25\ ns$ the above equation may be solved for m with the following results.

$\alpha_D = 1.02$ (backward and middle angles , $k \sim 10^7\ s^{-1}$)

$\alpha_D = 1.008$ (forward angles , $k \sim 4 \times 10^6\ s^{-1}$)

5.6.3 Tagging Efficiency

The tagging efficiency was measured at the beginning and the end of the experiment and also at the times when the proton detector was moved to a new position. The efficiency measurements (figure 5.7) averaged over the whole energy range are consistent with a mean value of $(0.65 \pm .01)$. The Monte Carlo prediction was 0.659 . The predicted values for the two energy bins were 0.653 and 0.671 for the 140 and 150 MeV bins respectively. The values used in normalising the cross-section were $(0.64 \pm .01)$ and $(0.66 \pm .01)$ respectively. Figure 5.7 also shows the file-by-file ratios of the ion chamber scaler to the ladder scalers. The 'standard' value changed from $\sim$ 32 to $\sim$ 182 because the sensitivity range of the ion chamber electrometer was changed. The sudden change from $\sim$ 32 to $\sim$ 16 remains unexplained however. These were the backward angle target-empty files which were discarded as described in the last section. The ion chamber/ladder ratio was otherwise constant to $\pm 1\%$.

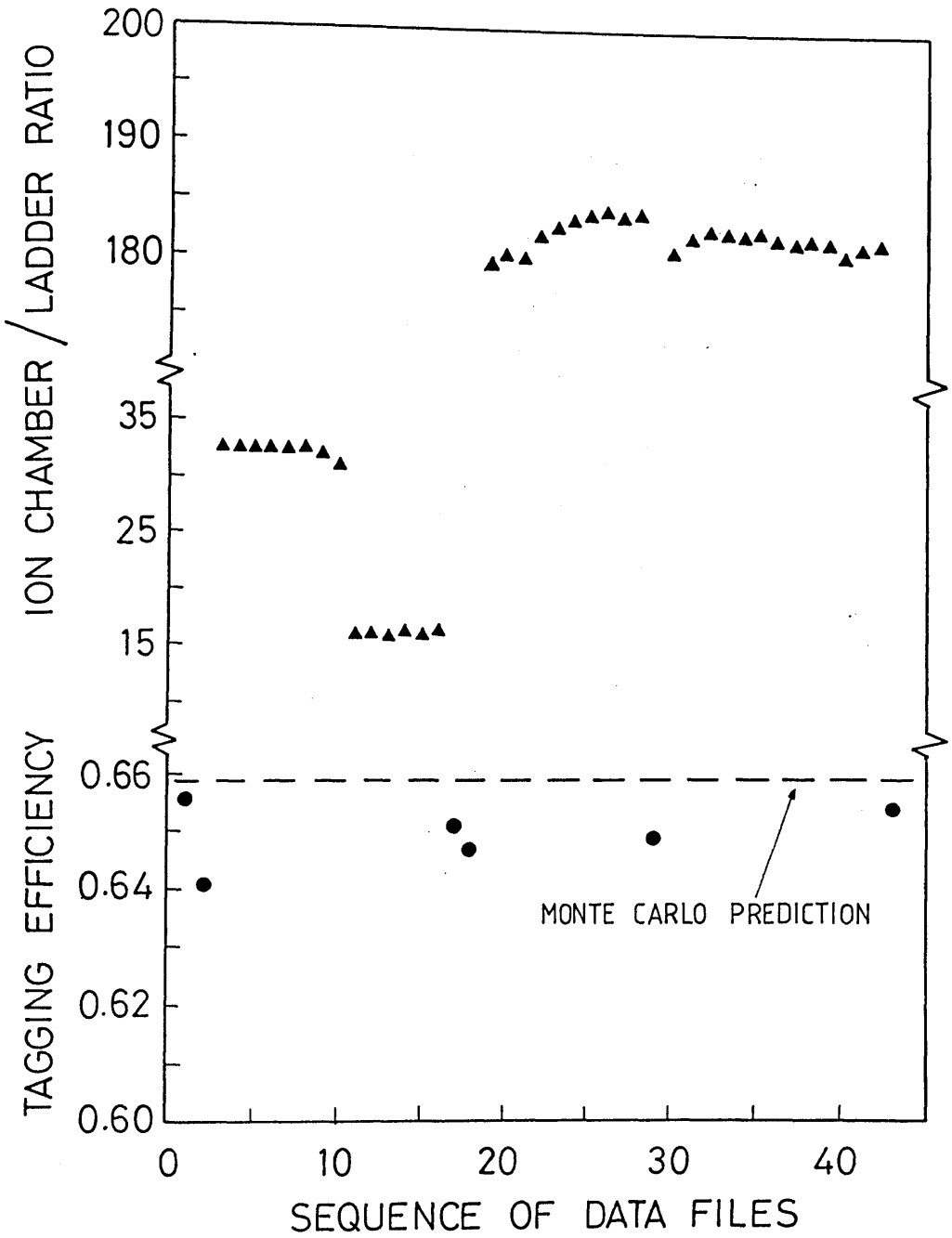

Figure 5.7: *Absolute tagging efficiency and ion chamber monitor readings plotted file by file throughout the experiment.*

5.6.4 Target Density

The density of target nuclei per unit area, ρ_N, is given by the following formula

$$\rho_N = 2N_A \frac{\bar{t}\rho'}{M_{mol}} \tag{5.12}$$

where N_A is the Avogadro constant, M_{mol} is the molar mass of deuterium, $\bar{t}$ is the effective target thickness, (see chapter 4) and ρ' is the effective density of the deuterium liquid. (see appendix D). Taking $\bar{t} = 3.07$cm and $\rho' = (0.153 \pm 0.005) g\ \mathrm{cm}^{-3}$ then $\rho_N = (1.41 \pm 0.05) \times 10^{23} \mathrm{cm}^{-2}$.

5.6.5 Multiplicity Corrections

The analysis of the loss of events caused by multiple ladder hits is given in appendix E. Essentially, the probability that a tagged event is *not* affected by a random coincidence is the probability that a time gate triggered by a true tagging electron contains 0 random electrons. If the random electron time distribution is described by a Poisson distribution then the required correction is

$$[P(0, N\tau)]^{-1} \equiv e^{N\tau} \tag{5.13}$$

where N is the mean electron rate incident upon a group of FPD channels served by a TDC and τ is the coincidence gate width. Taking the gate width as 58 ns the corrections are as follows.

	140MeV	150MeV	mean rate
fwd angle	0.95	0.95	6.6×10^5
mid angle	0.90	0.91	1.6×10^6
bwd angle	0.90	0.91	1.6×10^6

5.6.6 Systematic Errors

The systematic errors are estimated as follows:

tagging efficiency The continuous relative tagging efficiency monitor was constant to $\pm 1\%$ as were the periodic measurements of the absolute efficiency.

x-calibration The horizontal calibration matched the model prediction to within ~ 1 cm in 100. i.e. there is an associated solid angle uncertainty of $\pm 1\%$. Of course, the model itself could be inaccurate.

y-calibration The vertical position calibration is uncertain at the level of 1 part in 40. i.e. $\pm 2.5\%$

detector position An error of ± 5 mm in the detector to target distance would result in a solid angle error of $\pm 2\%$

target density The uncertainty in the determination of the target density was estimated to be $\pm 3\%$. This refers to the offline measurements made after the experiment. In order for this data to be relevant it must be assumed that the conditions were sufficiently similar to those of the experiment.

detector efficiency The most significant detector efficiency corrections are due to inelastic reactions undergone by the protons in the scintillator. The uncertainty in the corrections is estimated to be $\pm 2\%$

If all these systematic uncertainties are added in quadrature then the overall estimate of the systematic error is of the order of 5%.

5.7 Cross Sections

The angular differential cross-sections are given in tables 5.1 and 5.2 and displayed in figure 5.8 . The values are quoted both with and without the Monte Carlo efficiency corrections. The calculated efficiency factors represent the fraction of $D(\gamma,p)$ protons belonging to a particular angle-energy bin which satisfy the binning conditions. Events can be lost because the reconstructed proton angle or energy is wrong. On the other hand, the apparent efficiency can be increased if events are wrongly ascribed to the data bin. Generally, however, the net leakage of events from one bin to its neighbour will be small.

The angular distribution data comprises three overlapping sets of points corresponding to the forward, middle and backward angle proton detector positions. The three data sets are distinguished in figure 5.8 by the symbols used. The forward angle points are represented by circles, the middle angles by squares and the backward angle data by triangles. This convention is observed throughout the discussion of the results.

Most of the calculated efficiency factors lie between 0.85 and 0.95 but several of the points lying at the extremes of the angular range seen from each detector position require a very much larger correction. This is because the end of the physical detector system only covers a fraction of the solid angle subtended by the software defined $\theta - \phi$ angular bin. Conversely, the efficiency factor associated with the 135 °point in the mid-position data set is almost unity. In this case the loss of events due to nuclear interactions and external energy losses is cancelled by the excess events which are wrongly ascribed to this region of the detector as a result of the nonlinear position response towards the ends of the E blocks. The angular bins were chosen so

as to avoid the edges of the detector as much as possible. Therefore the most important cause of detector inefficiency is nuclear inelastic scattering in the scintillator. This effect becomes more important at higher proton energies. This is in keeping with the general trend of the efficiency factors which become smaller towards more forward angles. The observation that the Monte Carlo predictions give a reasonably good account of the efficiency corrections even when they are very large gives cause for confidence in their application to the main body of data.

The errors quoted in the tables are mainly the raw statistical errors associated with the reaction yields after the subtractions have been performed. The exceptions are the backward angle data points which are quoted with an additional error of 3% associated with the background subtraction. Similarly, the mid-angle 135 °point has been ascribed an error of 3% related to the uncertainty in the detector position response function towards the extreme end of the scintillator.

The calculated efficiency corrections are mean values calculated from a very large number of Monte Carlo histories. The variances associated with these estimates of the mean are very small. The estimated errors associated with the calculation are $< 0.5\%$. However this only represents the errors involved in the sampling of the model distributions included in the calculation. The errors inherent in the use of the approximate model response functions may be rather larger than the sampling errors.

$\theta_{cm}(deg)$	$\sigma(\mu b/sr)$	*efficiency*	$\sigma_{corr}(\mu b/sr)$
25	0.957 ± 0.03	0.299	3.20 ± 0.10
35	4.21 ± 0.08	0.858	4.91 ± 0.09
45	4.18 ± 0.08	0.880	4.76 ± 0.09
55	4.36 ± 0.08	0.899	4.86 ± 0.09
65	4.38 ± 0.08	0.876	5.00 ± 0.09
75	4.31 ± 0.08	0.910	4.75 ± 0.09
85	4.18 ± 0.08	0.929	4.51 ± 0.09
95	4.18 ± 0.08	0.941	4.45 ± 0.09
105	0.325 ± 0.009	0.121	2.67 ± 0.08
55	2.99 ± 0.07	0.575	5.19 ± 0.01
65	4.93 ± 0.09	0.952	5.18 ± 0.09
75	4.39 ± 0.08	0.933	4.71 ± 0.09
85	4.36 ± 0.08	0.932	4.68 ± 0.08
95	3.87 ± 0.08	0.933	4.15 ± 0.08
105	3.48 ± 0.08	0.934	3.72 ± 0.08
115	3.48 ± 0.08	0.937	3.71 ± 0.09
125	3.52 ± 0.08	0.946	3.73 ± 0.09
135	2.96 ± 0.12	0.998	2.97 ± 0.12
105	3.65 ± 0.15	0.871	4.18 ± 0.17
115	3.62 ± 0.15	0.934	3.88 ± 0.16
125	3.51 ± 0.17	0.947	3.71 ± 0.17
135	3.11 ± 0.15	0.918	3.38 ± 0.16
145	2.92 ± 0.15	0.880	3.32 ± 0.17
155	0.777 ± 0.051	0.232	3.35 ± 0.22

Table 5.1: *Angular differential cross section without Monte Carlo efficiency corrections (σ) and including corrections (σ_{corr}): $E_\gamma = 133 - 145$MeV*

$\theta_{cm}(deg)$	$\sigma(\mu b/sr)$	*efficiency*	$\sigma_{corr}(\mu b/sr)$
25	0.860 ± 0.03	0.299	2.87 ± 0.12
35	3.87 ± 0.09	0.858	4.62 ± 0.11
45	4.09 ± 0.09	0.880	4.65 ± 0.10
55	4.28 ± 0.09	0.899	4.76 ± 0.10
65	4.29 ± 0.09	0.876	4.84 ± 0.01
75	4.08 ± 0.10	0.910	4.47 ± 0.10
85	4.11 ± 0.09	0.929	4.42 ± 0.10
95	4.17 ± 0.09	0.941	4.42 ± 0.12
105	0.378 ± 0.01	0.121	3.12 ± 0.09
55	2.34 ± 0.06	0.575	4.07 ± 0.11
65	4.66 ± 0.09	0.952	4.90 ± 0.09
75	4.39 ± 0.08	0.933	4.71 ± 0.09
85	4.22 ± 0.08	0.932	4.53 ± 0.09
95	3.96 ± 0.08	0.933	4.23 ± 0.08
105	3.61 ± 0.08	0.934	3.87 ± 0.08
115	3.46 ± 0.08	0.937	3.70 ± 0.09
125	3.32 ± 0.09	0.946	3.51 ± 0.09
135	2.96 ± 0.13	0.998	2.97 ± 0.13
105	3.57 ± 0.18	0.871	4.10 ± 0.20
115	3.70 ± 0.18	0.934	3.97 ± 0.20
125	3.61 ± 0.20	0.947	3.82 ± 0.21
135	3.08 ± 0.18	0.918	3.35 ± 0.20
145	2.85 ± 0.19	0.880	3.25 ± 0.21
155	0.918 ± 0.091	0.232	3.95 ± 0.20

Table 5.2: *Angular differential cross sections without Monte Carlo efficiency corrections (σ) and including corrections (σ_{corr}): $E_\gamma = 145 - 158$MeV*

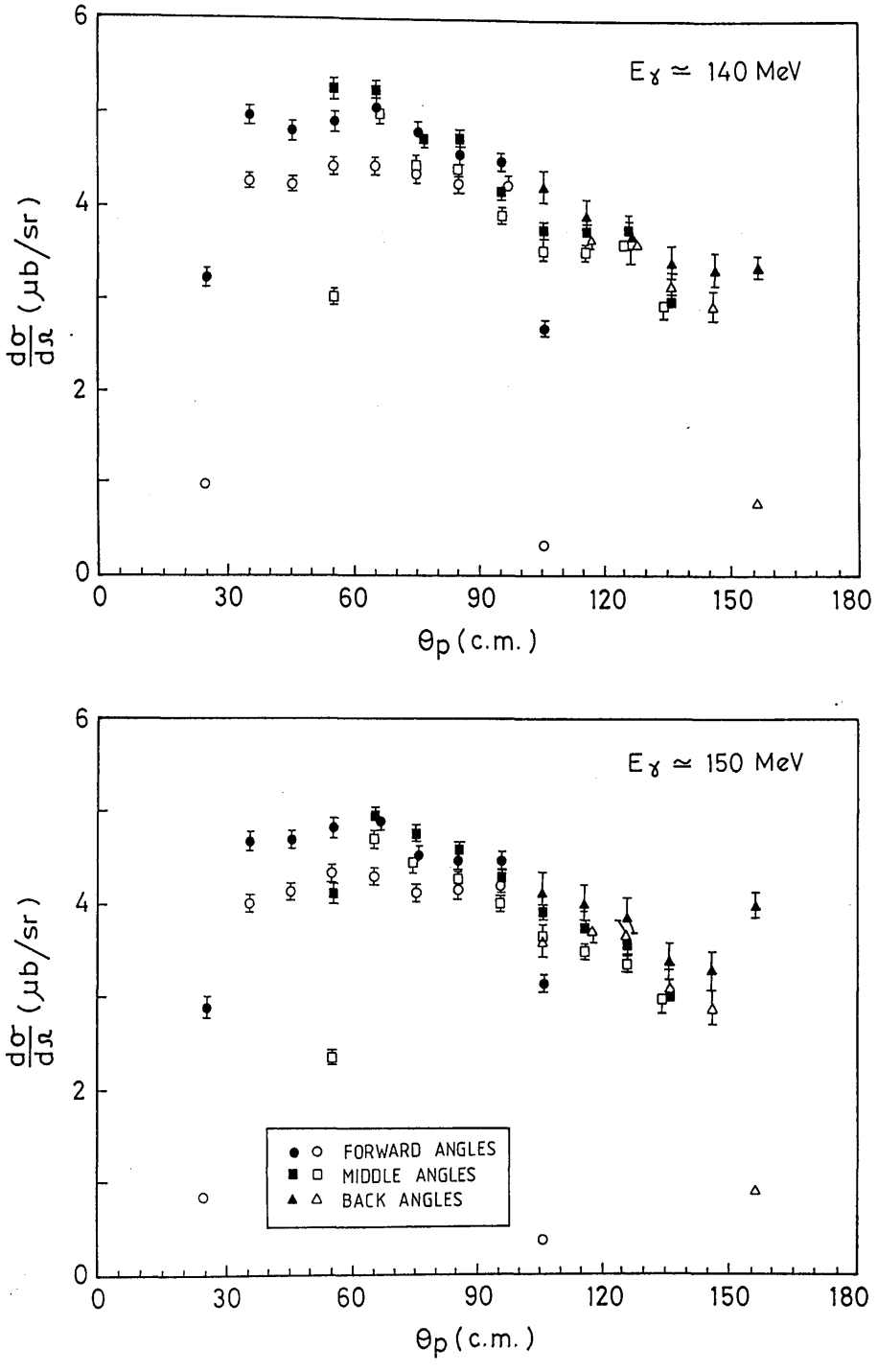

Figure 5.8: *Angular differential cross-sections with (solid points) and without (open points) Monte Carlo efficiency corrections.*

Chapter 6

Discussion and Conclusions

6.1 Final Cross Sections

The final cross-sections are given in table 6.1 . Only those data points for which the calculated efficiency correction is less than 15 % have been retained. Figure 6.1 shows the data plotted in comparison with the other recent measurements from INFN and TRIUMF. The three overlapping angular subsets which make up the angular distribution are each shown in full. This means that there are two data points at most of the angles in figure 6.1 . It was decided to present the data in this form because the three measurements are individually normalised and the stated 5 % systematic error is applicable independently to each data set. There exists, therefore, a systematic uncertainty not only in the absolute magnitude of the cross-section but also in its angular distribution. The three partial angular distributions are in agreement to within the errors quoted although the backward angle data appears to be systematically 6 % in excess of the middle angle data. The 35°point at 140 MeV appears to be anomalously high. This may be due to contamination by the sharply forward peaked atomic background, although if this were the case it would affect the corresponding 150 MeV data point to a similar extent.

6.2 Comparison with Recent Measurements

If the present result is qualitatively compared with previous work it is observed that the peak around middle angles in the angular distribution is less pronounced than that in the other measurements. The present data is lower in the middle of the distribution and higher at forward and backward angles. In order to place these comments on a more quantitative basis the various data

$\theta_{cm}(deg)$	$\sigma(\mu b/sr)$ $133-145$MeV	$\sigma(\mu b/sr)$ $145-158$MeV
35	4.91 ± 0.09	4.62 ± 0.11
45	4.76 ± 0.09	4.65 ± 0.10
55	4.86 ± 0.09	4.76 ± 0.10
65	5.00 ± 0.09	4.84 ± 0.01
75	4.75 ± 0.10	4.47 ± 0.10
85	4.51 ± 0.09	4.42 ± 0.10
95	4.45 ± 0.09	4.42 ± 0.12
65	5.18 ± 0.09	4.90 ± 0.09
75	4.71 ± 0.09	4.71 ± 0.09
85	4.68 ± 0.08	4.53 ± 0.09
95	4.15 ± 0.08	4.23 ± 0.08
105	3.72 ± 0.08	3.87 ± 0.08
115	3.71 ± 0.09	3.70 ± 0.09
125	3.73 ± 0.09	3.51 ± 0.09
135	2.97 ± 0.12	2.97 ± 0.13
105	4.18 ± 0.17	4.10 ± 0.20
115	3.88 ± 0.16	3.97 ± 0.20
125	3.71 ± 0.17	3.82 ± 0.21
135	3.38 ± 0.16	3.35 ± 0.20
145	3.32 ± 0.17	3.25 ± 0.21

Table 6.1: *Final cross-sections for* $E_\gamma = 133 - 145$MeV *and* $E_\gamma = 145 - 158$MeV

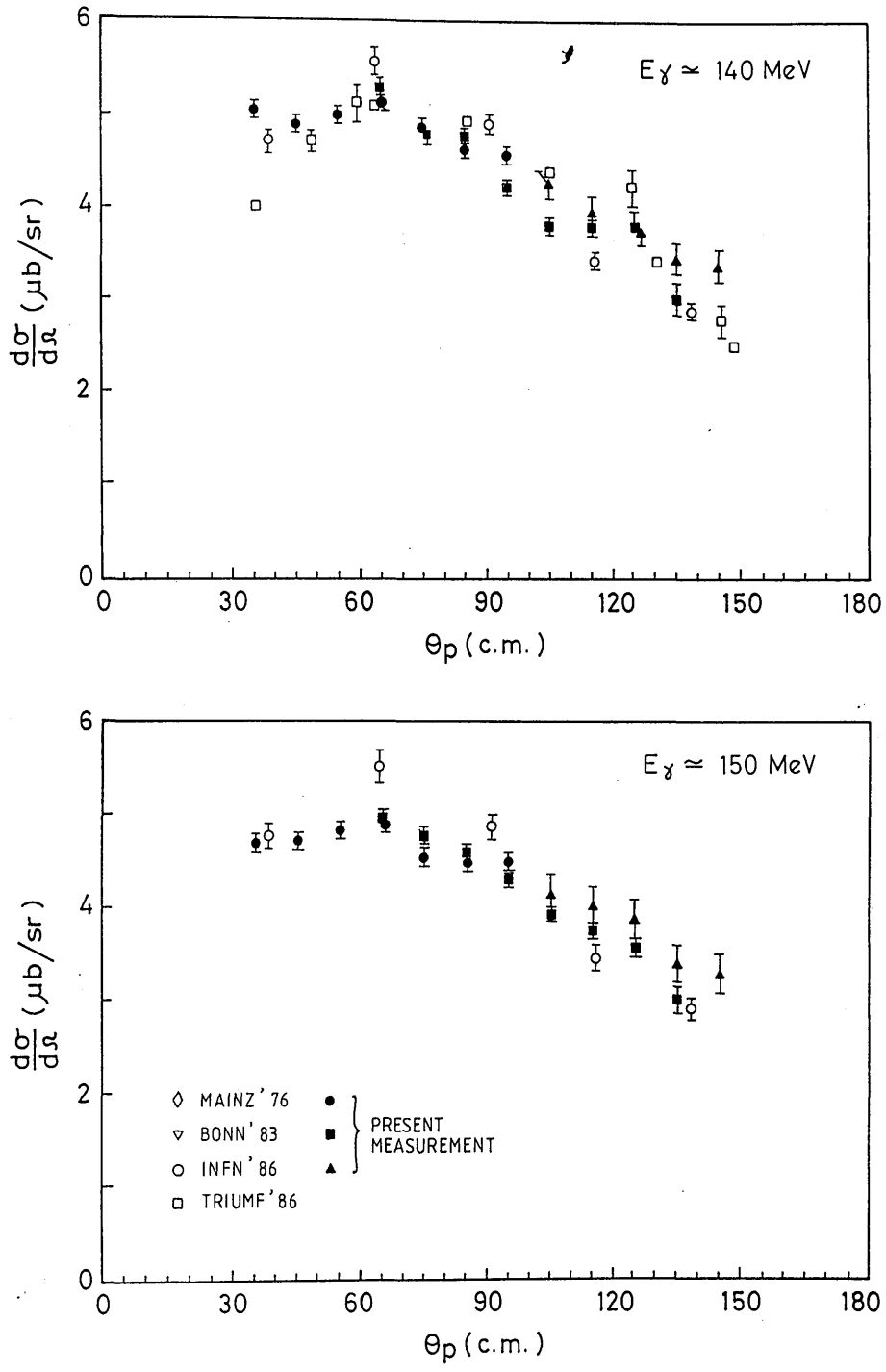

Figure 6.1: *Comparison of the results of the present experiment with other recent data on $D(\gamma,p)n$: data referenced in table 2.1*

sets were parameterised in terms of a series of Legendre polynomials $P_i(\cos\theta)$.

$$\frac{d\sigma}{d\Omega} = \sum_{i=0}^{4} A_i P_i(\cos\theta)$$

This parameterisation has the advantage that the total cross-section is given by

$$\sigma_{tot} = 4\pi A_0$$

The coefficients calculated from a least squares fit are given below. The angular distributions included in the comparison at 140 MeV are those of INFN and TRIUMF. In addition to the angular distribution data, all three data sets include 0 °and 180 °points extrapolated respectively from the Mainz 1976 and Bonn 1983 measurements (see table 2.1 for details). Figure 6.2 shows the present 140 MeV data plotted over the fit to the comparison data set.

coeff	140MeV this exp	150MeV this exp	140MeV comparison
A_0	4.20 ± 0.02	4.10 ± 0.02	4.20 ± 0.02
A_1	1.12 ± 0.04	1.03 ± 0.04	0.95 ± 0.03
A_2	-0.84 ± 0.05	-0.82 ± 0.05	-1.42 ± 0.04
A_3	-0.42 ± 0.05	-0.28 ± 0.05	-0.36 ± 0.05
A_4	-0.33 ± 0.05	-0.23 ± 0.05	-0.08 ± 0.05

At 140 MeV the A_0 values, and therefore the inferred total cross-sections, are similar. The contributions to the angular distribution made by the other Legendre coefficients can be seen from figure 6.3 where the first four Legendre functions are plotted. The A_1 coefficients are similar to within 20 %. These multiply the $P_1(\cos\theta)$ function which produces a slope from forward down to backward angles. The A_2 coefficients are negative and the value for the comparison data set is the greater by 70 %. This is primarily due to the more obvious peak in the middle angle region. The A_3 values differ by 17 %

and are again negative. This parameter governs the forward angle bias of the maximum value of the angular distribution.

Both the INFN and the TRIUMF experiments quote systematic uncertainties of the order of 5 % which is the same as that estimated for the present measurement. However, from the information available it seems that the systematic corrections in the TRIUMF experiment are significantly larger than those of the present one. For example the reaction tail in the deuteron detector was estimated to give rise to a 34 % efficiency correction and the corrections for the efficiency of the Cerenkov detectors were in some cases as large as 20 %. In comparison, the detector efficiency corrections applied in this experiment ranged from 14 to 5 %.

The INFN $D(\gamma, p)$ measurement lacked the kinematic overdetermination which proved to be very valuable for the suppression of background in the present experiment. This was because the bremsstrahlung photon contribution was not subtracted from the annihilation photon yield and therefore the experiment was not actually performed with a monoenergetic beam. The acceptance and efficiency corrections for the INFN detector system, which consisted of an array of small individually collimated telescopes, may also have been rather more complex than that for a large solid angle position sensitive detector. Furthermore in both of the above mentioned experiments the method of obtaining the absolute cross-section was more indirect than that used with a tagged photon system. For these reasons it may be that the 5 % uncertainty claimed in the case of this measurement represents a more conservative estimate than the similar figure quoted in the other experiments.

However, even allowing for possible systematic discrepencies in the angular

distributions, the total angular differential cross-section data set derived from recent experiments lies within a smoothly varying band of relative width $\sim$ 10 %.

6.3 Comparison with Recent Calculations

The photodisintegration of the deuteron has attracted a great deal of renewed interest from theoretical workers in recent years and there are now several model predictions available with which to compare the present data. The latest versions of the calculations of several theory groups are presented in figure 6.4 in comparison with the results of this experiment. The total data set is displayed similarly in figure 6.5.

It is seen that none of the available calculations gives a fully satisfactory account of the differential cross-section. The predictions of Wilhelm, Leidemann and Arenhövel (WLA) [70] and Jaus and Woolcock (JW) [21] appear to be in closest agreement. Cambi, Mosconi and Ricci (CMR) report that their treatment of the $N-N$ interaction is only valid below the pion threshold and that their present calculation may not be reliable at 140 MeV.[69]

The potentials most frequently used in modern calculations are the Bonn [15] and Paris [24] models. Both potentials use the well established one pion exchange mechanism (OPE) for the long range part of the interaction. (i.e. $>$ 1.5 fm). This gives a satisfactory account of the static properties of the deuteron, in particular the value of the electric quadrupole moment Q_D. In fact, although the two models predict different D-state probabilities for the deuteron wave function (Bonn - 4.25 % ; Paris 5.75 %) the value of Q_D is dependent on the value of the S/D ratio at large radial distances where the

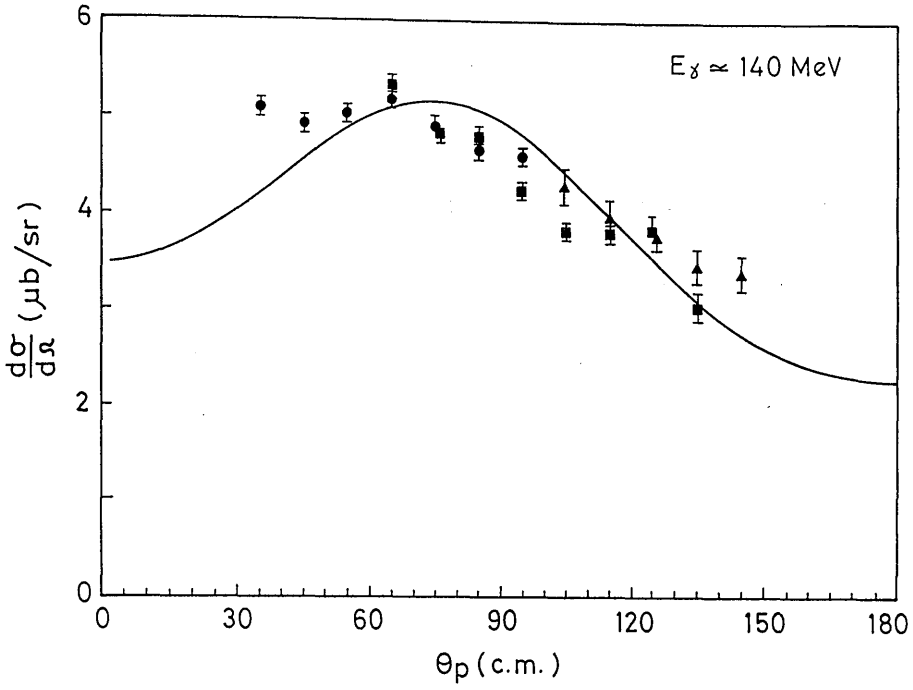

Figure 6.2: *Comparison of the results of the present experiment with a Legendre polynomial parameterisation of the other recent data. (Details given in the text)*

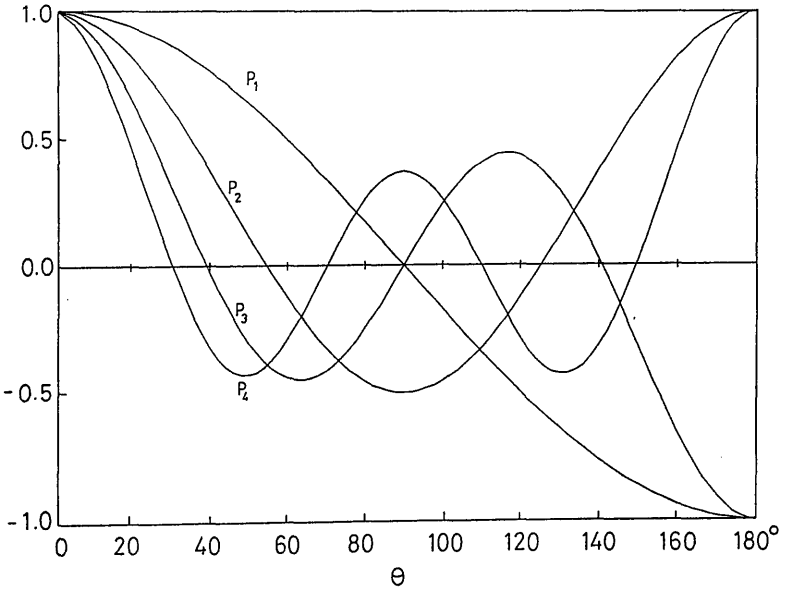

Figure 6.3: *The first 4 Legendre Polynomials* $P_i(\cos\theta)$.

OPE is the dominant interaction.

The shorter range parts of the two potentials are rather different however. The Bonn approach is to approximate the two and three pion exchange interactions in terms of π, ρ, σ and ω mesons. For example, the exchange of two correlated pions in a relative S state or P state is parameterised as the exchange of a $\sigma(0^+, 0)$ meson or $\rho(1^-, 1)$ meson. The Bonn model is not purely a one boson exchange potential however. Uncorrelated 2π exchange is included explicitly and there is a $\pi\rho$ exchange mechanism in addition to the ω exchange.

In contrast, the short range part of the Paris potential is constructed from dispersion relations taking into account explicitly all information on the 2π and part of the 3π exchange contribution. In either approach the medium and short range potential becomes momentum dependent. This nonlocal short range interaction is intimately connected with the excitation of virtual Δs in the nucleus. This may be where a large part of the discrepency between different calculations arises since there is no consensus of theoretical opinion as to the best way to treat the propagation of the Δ in the nucleus.

The most common approach to the photodisintegration problem is to perform the calculation in co-ordinate space using a multipole expansion of the electromagnetic transition operator. At the energies presently under consideration it is sufficient to include only those multipoles up to $l = 4$. The exchange effects in the electric multipoles are dealt with using the Siegert theorem by which the total current operators are expressed in terms of the better known charge density operators. This approach has been refined by several authors, in WLA [70], CMR [19] [20] [69] and JW [21]. It is now standard practice to include relativistic corrections to the one body charge density operators and

to include a non vanishing two body contribution resulting from exchange effects. This last effect was found to improve the agreement with the 0°data when calculated with pseudovector πN coupling and to have the opposite effect in pseudoscalar coupling (CMR). The exchange contributions to the magnetic transitions must be put in explicitly and at the moment the pion and Δ currents are included in the static approximation with varying levels of relativistic correction. Non relativistic wave functions are also used and there are frame dependent corrections to the amplitude which must be considered (JW). The Paris potential has been used by all of the above authors.

An alternative approach has been pioneered by Laget [12] [68] who uses a momentum space expansion of amplitude into S-matrix diagrams representing the direct nucleon, meson exchange and nucleon rescattering processes. The calculation uses a low energy expansion of the nuclear electromagnetic currents which is Lorentz invariant to $O\left(\frac{1}{M_N^2}\right)$. The interaction is explicitly gauge invariant in the latest version of the calculation and consistent wave functions derived from the Paris potential are used. All partial waves are implicitly included in the interaction and the pion nucleon rescattering has been calculated for S, P and D waves in the final state.

A recent calculation by Ying, Henley and Miller (YHM) [71] largely follows the prescription of JW but substitutes the Bonn potential for the Paris potential. The motivation was to determine whether the smaller D-state contribution contained in the Bonn-derived deuteron wave function would lead to a smaller forward angle cross-section in better agreement with experiment. No significant effect was found at 0 °but the angular distribution was greatly changed (figure 6.4). YHM found that by *arbitrarily* increasing the contribu-

tion of M1 transition by a factor 2 the agreement of the angular distribution at 140 MeV was very much improved. This sensitivity to the M1 transition may be a reflection of the importance of the treatment of Δ excitations even at energies well below the resonance. The possibility arises that the photodisintegration reaction will provide a tool for the comparison of the different models of the short range N-N interaction. It is to be regretted, however, that YHM did not repeat the calculation using the Paris potential in order to confirm that the choice of potential is indeed the source of the discrepency. On the other hand, JW suggest that the total short range 2π exchange current contribution to the process will be small since the ρ exchange part (correlated 2π exchange) is small. Nothing certain can be said, however, unless the different interactions are employed in directly comparable calculations utilising the same theoretical techniques. It would be particularly useful if the different treatments could be compared at various stages of completeness in order to identify the sources of the discrepencies. The non relativistic impulse approximation calculation will probably display a sensitivity to the choice of potential because of the different D-state probabilities. This has already been remarked upon in the case of deuteron electrodisintegration near threshold [72]. The available relativistic impulse calculations are known to include varying dynamical and kinematical corrections such as, respectively, charge density terms and frame dependent effects. The next step would be to include meson exchange effects, perhaps subdividing this into the dominant one pion exchange current and then the multi-pion and heavier meson part. Finally the Δ resonance excitation and propagation should be included. This is where the largest theoretical uncertainties appear to lie. Unfortunately, this program of theoretical investigation may be unfeasable because consistent definitions of

the various classes of current cannot be identified in such a way as to permit a direct comparison of the various models. Indeed it may be that different means of implementing the gauge invariance constraint legitimately result in different versions of the one body and MEC currents yielding different results. The most obvious example of this is the use of Siegert operators in the electric multipole transition matrix elements.

6.4 Conclusions

The experiment has successfully achieved its stated aim, in that the angular differential cross section for the two body photodisintegration of the deuteron has been measured to an overall accuracy of ~ 6 %.

The performance of the experimental apparatus has been generally in keeping with its design specification. In particular, the use of the tagging technique has permitted the photon beam intensity to be determined to within ± 1 %. Naturally, in hindsight, there are improvements which could be made to the apparatus. The acceptance of the detector system would have been better defined if the area of the ΔE_1 detectors was sufficiently reduced so as to provide collimation for the E detectors behind. Such a physical restriction on the effective solid angle would provide a valuable check on the software defined detector acceptance.

The design of the target could also be profitably modified. The Max Planck Institute group at Mainz has successfully operated a liquid D_2 target screened by an envelope of cold D_2 gas [73]. The gas provides additional cooling by convection and effectively prevents boiling in the liquid and thus eliminates one of the largest normalisation corrections in the present experiment.

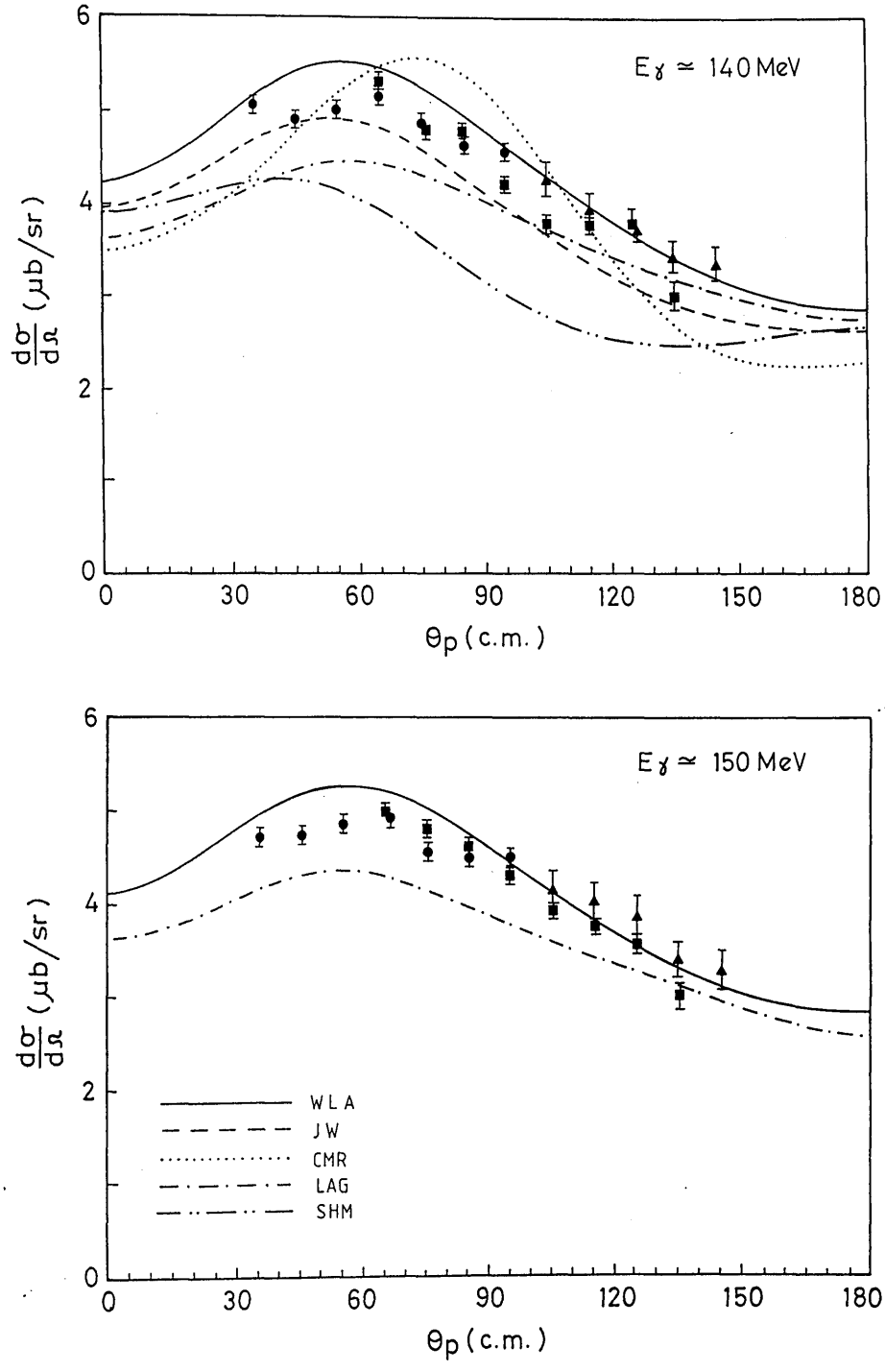

Figure 6.4: *Comparison of the results of the present experiment with theoretical predictions for the process* $D(\gamma,p)n$.
Theory references: WLA [70]; JW [21]; CMR [69]; LAG [68]; SHM [71]

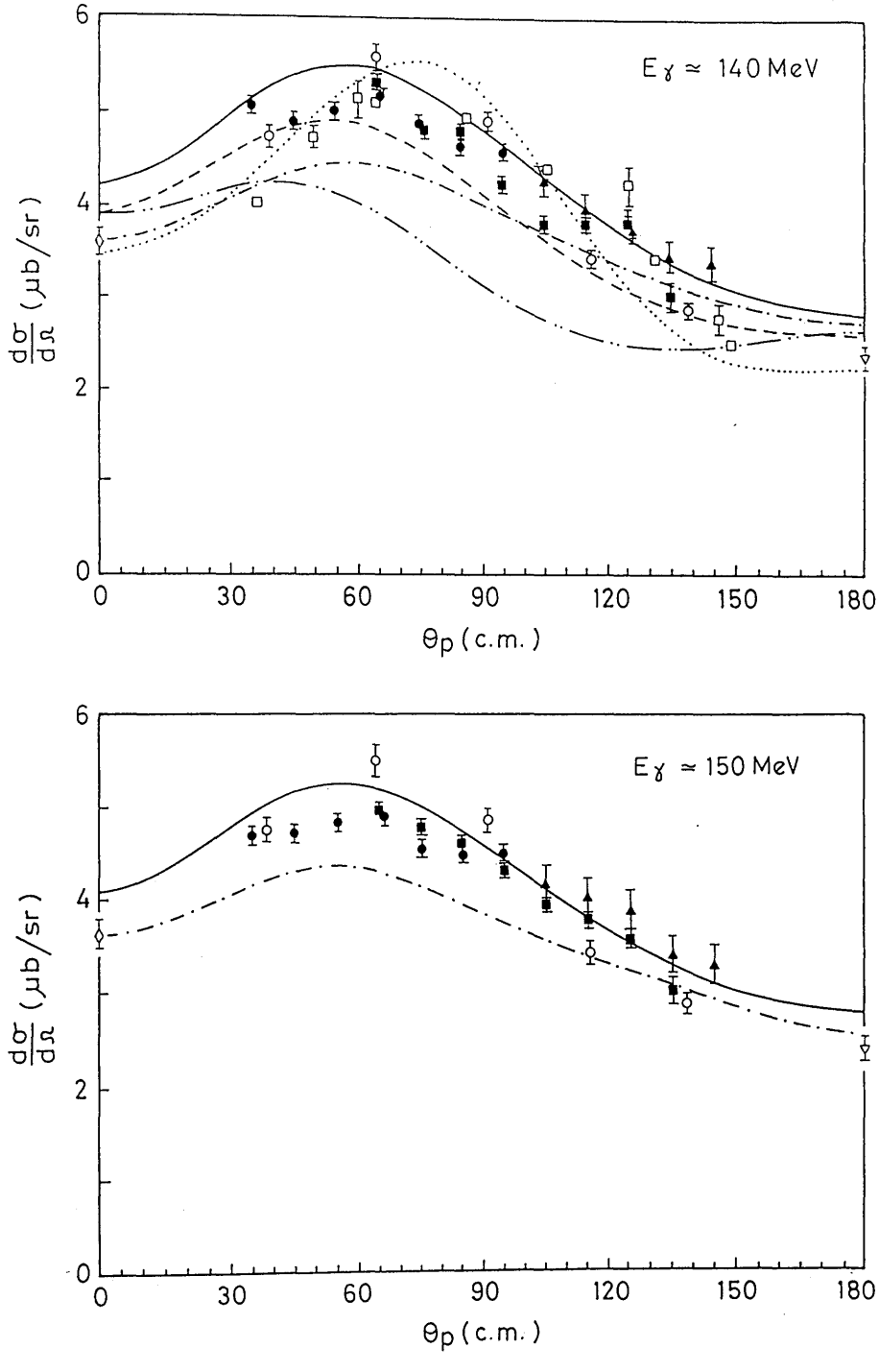

Figure 6.5: *Comparison of all the available recent data with theoretical predictions for the process* $D(\gamma, p)n$.

The largest detector efficiency correction was due to the effects of the inelastic nuclear reactions undergone by the protons in the scintillator material. The Monte Carlo corrections for this effect were based on a rather old survey of $^{12}C(\gamma, x)$ reaction data [62] and it may be that a compilation of more modern cross-section measurements would be useful.

The deuteron photodisintegration process remains an important challenge for both theorists and experimentalists. The present measurement represents a significant improvement in the status of the empirical knowledge of the reaction within one rather narrow energy band. Reliable data remains rather sparse at most other energies, however, and there have been no measurements of the 0 °and 180 °cross-sections performed with monochromatic photon beams. One of the most significant experimental developments to be expected in the near future will be the advent of intense polarised photon beams available at either laser backscattering or photon tagging facilities. This will allow access to a range of polarisation observables which will provide independent constraints which the theories must satisfy in addition to the angular differential cross-section.

The theoretical discrepencies at 140 MeV are rather larger than the experimental inconsistancies. Work is urgently needed to establish the extent to which the differences between the theoretical predictions are due to genuinely different physics input and to what extent they can be blamed on the technical details of the calculations. If these uncertainties can be clarified there is then a real prospect that one may be able to use the deuteron photodisintegration reaction as a reliable benchmark against which to measure the validity of the increasingly sophisticated models of the N-N interaction.

Appendix A

The Dirac Equation

Definitions

The Dirac equation, which is the equation of motion for a spin-$\frac{1}{2}$ particle, can be written

$$i\hbar\frac{\partial\psi(x)}{\partial t} = \left[c\vec{\alpha}\cdot(-i\hbar\nabla) + \beta mc^2\right]\psi(x) \tag{A.1}$$

where $\vec{\alpha} = (\alpha_1, \alpha_2, \alpha_3)$ and β are 4×4 Hermitian matrices satisfying

$$[\alpha_i, \alpha_j]_+ = 2\delta_{ij}, \qquad [\alpha_i, \beta]_+ = 0, \qquad \beta^2 = 1 \tag{A.2}$$

In the Dirac-Pauli representation $\vec{\alpha}$ and β are given by

$$\beta = \begin{pmatrix} 1 & 0 \\ 0 & -1 \end{pmatrix} \qquad \alpha_i = \begin{pmatrix} 0 & \sigma_i \\ \sigma_i & 0 \end{pmatrix} \tag{A.3}$$

Where the σ_i are the Pauli matrices. The Dirac equation possesses plane wave solutions of the form

$$\psi(x) = const.\left\{ \begin{array}{c} u_r(\vec{p}) \\ v_r(\vec{p}) \end{array} \right\} e^{\mp ipx/\hbar} \tag{A.4}$$

where $p = (E_p, \vec{p})$ and $E_p = +\left(m^2c^4 + c^2\left|\vec{p}\right|^2\right)^{1/2}$. $u_r(\vec{p})$ corresponds to a particle of momentum $\vec{p}$ and positive energy E_p and $v_r(\vec{p})$ to a particle of momentum $-\vec{p}$ and negative energy $-E_p$. The index $r = 1, 2$ labels two independent

solutions for each four-momentum p which can be chosen to represent the spin states of the particle. With the following definitions for the two-spinors

$$\chi_1 \equiv \chi_2' \equiv \begin{pmatrix} 1 \\ 0 \end{pmatrix}, \qquad \chi_2 \equiv \chi_1' \equiv \begin{pmatrix} 0 \\ 1 \end{pmatrix} \tag{A.5}$$

the positive and negative energy solutions of the Dirac equation can be written

$$u_r(\vec{p}) = A \begin{pmatrix} \chi_r \\ B\vec{p}\cdot\vec{\sigma}\chi_r \end{pmatrix}, \qquad v_r(\vec{p}) = A \begin{pmatrix} B\vec{p}\cdot\vec{\sigma}\chi_r' \\ \chi_r' \end{pmatrix} \tag{A.6}$$

where

$$A \equiv \left(\frac{E_p + mc^2}{2mc^2}\right)^{1/2}, \qquad B \equiv \frac{c}{E_p + mc^2} \tag{A.7}$$

The behaviour of these solutions for non-relativistic velocities $\left(\frac{|\vec{p}|}{mc} \ll 1\right)$ is readily seen. For the positive energy solutions u_r, the upper two components are very large compared to the lower two, while for the negative energy solutions v_r it is the lower two components which dominate. In particular, the positive and negative energy solutions for a particle at rest are

$$u_r(\vec{0}) = \begin{pmatrix} \chi_r \\ 0 \end{pmatrix}, \qquad v_r(\vec{0}) = \begin{pmatrix} 0 \\ \chi_r' \end{pmatrix} \tag{A.8}$$

Interaction with the EM Field

In the presence of an electromagnetic field the Dirac equation for a charged particle is modified by making the following substitutions

$$i\hbar\frac{\partial}{\partial t} \longrightarrow i\hbar\frac{\partial}{\partial t} - e\Phi(x), \qquad -i\hbar\nabla \longrightarrow -i\hbar\nabla - \frac{e}{c}\vec{A}(x) \tag{A.9}$$

Equation A.1 now takes the form

$$\left(i\hbar\frac{\partial}{\partial t} + c\vec{\alpha}\cdot(i\hbar\nabla) - \beta mc^2\right)\psi(x) = e\left(\Phi - \vec{\alpha}\cdot\vec{A}\right)\psi(x) \tag{A.10}$$

This inhomogeneous form of the Dirac equation corresponds to the existence of an interaction Hamiltonian of the form

$$H_{int} = e\left(\psi^+\psi\Phi - \psi^+\vec{\alpha}\psi\cdot\vec{A}\right) \tag{A.11}$$

in four-vector notation H_{int} can be rewritten as $J_\mu A^\mu$ where

$$J_\mu \equiv (\rho c, \vec{J}) = e\left(\psi^+\psi, \psi^+\vec{\alpha}\psi\right) \tag{A.12}$$

and

$$A_\mu = \left(\Phi, \vec{A}\right) \tag{A.13}$$

The following definitions

$$\gamma^0 \equiv \beta \qquad \gamma^i \equiv \beta\alpha^i \qquad \bar{\psi} \equiv \psi^+\gamma^0 \tag{A.14}$$

allow this result to be written in an explicitly covariant form:

$$J_\mu = e\bar{\psi}\gamma_\mu\psi \tag{A.15}$$

Thus the interaction Hamiltonian couples the charged current J_μ to the electromagnetic field. Using the Dirac equation it can be shown that the current J_μ is conserved, i.e.

$$\frac{\partial\rho}{\partial t} - \nabla\cdot\vec{J} = 0 \tag{A.16}$$

Substituting in the explicit form for ψ defined above the following are obtained

$$\psi^+\psi \equiv \frac{E}{mc}, \qquad \psi^+\vec{\alpha}\psi \equiv \frac{\vec{p}}{m} \tag{A.17}$$

Factors of $\hbar$ and c have been retained for for the sake of clarity in this appendix. Thoroughout the rest of the thesis units such that $\hbar = c = 1$ have been used.

A.1 The Foldy-Wouthuysen Transformation

The Foldy-Wouthuysen transformation is a procedure by which the large and small components of the Dirac spinor representing a particle may be decoupled by means of a unitary transformation. Thus the spinor for a positive energy particle will be a four-spinor whose lower two-spinor is identically zero. This is achieved by finding a representation of the Hamiltonian which is free of operators which couple the large and small components in the four-spinor. These are so-called 'odd' operators. Those which do not couple the large and small components are termed 'even'. For free particles such a transformed Hamiltonian is obtainable in closed form. However, in the case of interacting particles it is not possible to eliminate all the odd operators in a finite series of transformations. Instead, a series of transformations may be performed, the result of which is to remove all odd operators to $O\left(\frac{1}{m}\right)$, then $O\left(\frac{1}{m^2}\right)$ etc. For interactions with fields that are weak compared to mc^2 the result converges rapidly.

Writing the Hamiltonian as

$$H = \beta m + \Omega_e + \Omega_o \tag{A.18}$$

where Ω_e is the even and Ω_o the odd operators. The rest mass term βm is assumed to be dominant. The general prescription is to choose U in

$$H' = e^{iU} H e^{-iU} \tag{A.19}$$

to be

$$U = \frac{-i}{2m}\beta\Omega_o \tag{A.20}$$

thus

$$H' = \sum_{n=0}^{\infty} \frac{1}{n!} T_n \tag{A.21}$$

where $T_o = H$ and $T_n = [iU, T_{n-1}]$ for all $T_n, n \geq 1$. Retaining terms to $O\left(\frac{1}{m^2}\right)$ we have

$$H' = \beta m + \Omega_e + \frac{1}{2m}\beta\Omega_o^2 + \frac{\beta}{2m}[\Omega_o, \Omega_e] - \frac{1}{8m^2}[\Omega_o, [\Omega_o, \Omega_e]] - \frac{1}{3m^2}\Omega_o^3 \quad \text{(A.22)}$$

The Hamiltonian is now even to $O\left(\frac{1}{m}\right)$. The $O\left(\frac{1}{m^2}\right)$ odd operators may be removed by a similar transformation, where U is replaced by U':

$$U' = \frac{-i}{2m}\beta\left[\frac{\beta}{2m}[\Omega_o, \Omega_e] - \frac{1}{3m^2}\Omega_o^3\right] \quad \text{(A.23)}$$

To order $O\left(\frac{1}{m^2}\right)$ the non-relativistic Hamiltonian H_{NR} is given by

$$H_{NR} = \beta m + \Omega_e + \frac{1}{2m}\beta\Omega_o^2 - \frac{1}{8m^2}[\Omega_o, [\Omega_o, \Omega_e]] \quad \text{(A.24)}$$

In the case of the electromagnetic interactions of a particle with an anomalous magnetic moment the following replacements may be made

$$\begin{aligned} \Omega_o &= \vec{\alpha}\cdot(\vec{p} - e\vec{A}) + \frac{i\kappa}{2m}\beta\vec{\alpha}\cdot\vec{E} \\ \Omega_e &= e\Phi - \frac{\kappa}{2m}\beta\vec{\sigma}\cdot\vec{B} \end{aligned} \quad \text{(A.25)}$$

where $\vec{A}$ and Φ are the vector and scalar e.m. potentials, $\vec{E}$ and $\vec{B}$ are the electric and magnetic fields and κ is the anomalous magnetic moment. Making these substitutions H_{NR} becomes

$$H_{NR} = m + e\Phi + \frac{1}{2m}(\vec{p} - e\vec{A})^2 - \frac{\mu}{2m}\vec{\sigma}\cdot\vec{B} - \frac{2\mu - e}{4m^2}\vec{\sigma}\cdot\vec{E}\times(\vec{p} + e\vec{A}) - \frac{2\mu - e}{8m^2}\nabla\cdot\vec{E} \quad \text{(A.26)}$$

where $\mu = e + \kappa$ is the total magnetic moment.

Appendix B

Electromagnetic Current Conservation

B.1 Siegert's Theorem

The conventional approach to photodisintegration calculations uses an expansion in electric and magnetic multipoles of the configuration space matrix element. Siegert's theorem may be used to express the leading order term of each electric multipole transition operator in terms of the one-body charge density operator [23].

The general form of the matrix element for a photonuclear reaction is

$$\sqrt{\frac{2\pi}{\omega_\gamma}}\langle f|\int e^{i\vec{k_\gamma}\cdot\vec{x}}\vec{\varepsilon}_\lambda\cdot\vec{J}(\vec{x})d^3x|i\rangle \equiv \sqrt{\frac{2\pi}{\omega_\gamma}}\langle f|T(\vec{k}_\gamma,\vec{J},\lambda)|i\rangle \qquad \text{(B.1)}$$

Where $T(\vec{k}_\gamma,\vec{J},\lambda)$ is a transition operator which may be expanded into electric and magnetic multipole terms as follows.

$$T(k_\gamma,\vec{J},\lambda) = -\sqrt{2\pi}\sum_L i^L\sqrt{2L+1}\left[T^{[L]}_{el}(k_\gamma,\vec{J},\lambda)+\lambda T^{[L]}_{mag}(k_\gamma,\vec{J},\lambda)\right] \qquad \text{(B.2)}$$

where

$$T^{[L]}_{el}(k_\gamma,\vec{J},\lambda) = \frac{1}{k}\int d^3x\left\{\nabla\times\left[j_L(k_\gamma x)\vec{Y}_{LL\lambda}(\Omega_x)\right]\right\}\cdot\vec{J}(\vec{x}) \qquad \text{(B.3)}$$

$$T^{[L]}_{mag}(k_\gamma, \vec{J}, \lambda) = \int d^3x \left\{ j_L(k_\gamma x) \vec{Y}_{LL\lambda}(\Omega_x) \right\} \cdot \vec{J}(\vec{x}) \tag{B.4}$$

where the incoming photon momentum $\vec{k_\gamma}$ has been assumed to be parallel to the z-axis. $j_L(k_\gamma x)$ are spherical Bessel functions and $\vec{Y}_{LL\lambda}(\Omega_x)$ are vector spherical harmonics.

The electric multipole operator $T^{[L]}_{el}$ may be split into two parts.

$$T^{[L]}_{el}(k_\gamma, \vec{J}, \lambda) = T^{[L]}_{a}(k_\gamma, \vec{J}, \lambda) + T^{[L]}_{b}(k_\gamma, \vec{J}, \lambda) \tag{B.5}$$

where

$$T^{[L]}_{a}(k_\gamma, \vec{J}, \lambda) = \frac{1}{ik_\gamma \sqrt{L(L+1)}} \int d^3x \nabla \left[\left(1 + x \frac{d}{dx} \right) j_L(k_\gamma x) Y_{L\lambda}(\Omega_x) \right] \cdot \vec{J}(\vec{x}) \tag{B.6}$$

$$T^{[L]}_{b}(k_\gamma, \vec{J}, \lambda) = \frac{1}{i\sqrt{L(L+1)}} \int d^3x k_\gamma \vec{x} j_L(k_\gamma x) Y_{L\lambda}(\Omega_x) \cdot \vec{J}(\vec{x}) \tag{B.7}$$

In the long wave approximation ,i.e. $k_\gamma x \ll 1$ over nuclear dimensions, T_a gives the dominant contribution to the electric transitions since T_b is one order higher in $(k_\gamma x)$. The term $T^{[L]}_a$ may be transformed by partial integration and the use of the current conservation equation 1.22 as follows.

$$T^{[L]}_{a}(k_\gamma, \vec{J}, \lambda) \rightarrow T'^{[L]}_{a}(k_\gamma, \rho, \lambda) \tag{B.8}$$

where

$$T'^{[L]}_{a}(k_\gamma, \rho, \lambda) = \frac{1}{k_\gamma \sqrt{L(L+1)}} \left[H, \int d^3x \rho(\vec{x}) \left(1 + x \frac{d}{dx} \right) j_L(k_\gamma x) Y_{L\lambda}(\Omega_x) \right] \tag{B.9}$$

This relation is the exact statement of Siegert's theorem expressing the transverse electric multipole moments in terms of the longitudinal charge moments. In the assumption that interaction effects do not introduce many-body charge density operators $\rho(\vec{x})$ may be set equal to $\rho_{(1)}(\vec{x})$.

B.2 The T-R-K Sum Rule

The Thomas-Reich-Kuhn sum rule for the energy integrated $E1$ photoabsorption cross-section provides an example of the power of the Siegert approach.

The interest in sum rules stems from the fact that in summing over all the final states reached by some excitation operator one can evaluate the sum by using closure in terms of a ground state expectation value of a suitable operator which allows a simple interpretation in terms of the gross properties of the system without detailed knowledge of the excitation spectrum.

The $E1$ interaction of a spatially constant electromagnetic field $\vec{E}$ with a system of nucleons may be written as:

$$\begin{aligned} H_{int}^{E1} &= e\vec{E}\cdot\sum_{\pi=1}^{Z}\vec{x}_\pi \\ &= e\vec{E}\cdot\left[\frac{N}{A}\sum_{\pi=1}^{Z}\vec{x}_\pi - \frac{Z}{A}\sum_{\nu=1}^{N}\vec{x}_\nu + \frac{Z}{A}\sum_{\pi=1}^{Z}\vec{x}_\pi + \frac{Z}{A}\sum_{\nu=1}^{N}\vec{x}_\nu\right] \\ &= e\vec{E}\cdot\left[\frac{N}{A}\sum_{\pi=1}^{Z}\vec{x}_\pi - \frac{Z}{A}\sum_{\nu=1}^{N}\vec{x}_\nu + Z\vec{X}\right] \end{aligned} \qquad \text{(B.10)}$$

where π stands for protons, ν for neutrons and $\vec{X}$ denotes the position of the centre of mass of the nucleus. The term $eZ\vec{E}\cdot\vec{X}$ corresponds to the interaction of the entire nucleus with the electric field and leads to nuclear Thomson scattering. All Z protons and N neutrons contribute to dipole absorption with effective charges e_α:

$$\frac{N}{A}e \qquad \text{for} \qquad 1 \le \alpha \le Z \qquad \text{(protons)}$$

$$-\frac{Z}{A}e \qquad \text{for} \qquad Z+1 \le \alpha \le A \quad \text{(neutrons)}$$

The integrated cross-section may be written in terms of a sum over transition probabilities to all final states:

$$\int_0^\infty \sigma_{E1}(E_\gamma)dE_\gamma = 2\pi \sum_f \left|\langle f|H_{int}^{E1}|i\rangle\right|^2 \tag{B.11}$$

Assuming polarisation with the electric vector in the z direction the matrix element is

$$\langle f|H_{int}^{E1}|i\rangle = \sqrt{\frac{2\pi}{\omega_\gamma}}\langle f|\sum_{\alpha=1}^{A}\frac{e_\alpha}{M}\vec{\varepsilon}_\lambda\cdot\vec{p}|i\rangle \tag{B.12}$$

which can be rewritten in the Siegert form

$$\langle f|H_{int}^{E1}|i\rangle = i\sqrt{\frac{2\pi}{\omega_\gamma}}\langle f|\left[H,\vec{\varepsilon}_\lambda\cdot\vec{D}\right]|i\rangle \tag{B.13}$$

or, evaluating the commutator,

$$\langle f|H_{int}^{E1}|i\rangle = i\sqrt{\frac{2\pi}{\omega_\gamma}}\left(E_f - E_i\right)\langle f|D_z|i\rangle \tag{B.14}$$

Where $\vec{D} = \sum_{\alpha=1}^{A}\vec{D}_\alpha = \sum_{\alpha=1}^{A} e_\alpha\vec{x}_\alpha\delta^3(\vec{x}-\vec{x}_\alpha)$. We require the square of this quantity and can expand it as a double sum over the nucleons α.

$$\frac{1}{2\pi}\sum_f\left|\langle f|H_{int}^{E1}|i\rangle\right|^2 = \sum_f\sum_{\alpha=1}^{A}\sum_{\beta=1}^{A}\langle i|D_{\alpha z}|f\rangle\left(E_f-E_i\right)\langle f|D_{\beta z}|i\rangle \tag{B.15}$$

Using $D_\alpha H|f\rangle = D_\alpha|f\rangle E_f$ and $\langle i|HD_\alpha = E_i\langle i|D_\alpha$ this is transformed to:

$$\frac{1}{2}\sum_f\sum_{\alpha=1}^{A}\sum_{\beta=1}^{A}\left\{\langle i|\left[D_{\alpha z},H\right]|f\rangle\langle f|D_{\beta z}|i\rangle - \langle i|D_{\alpha z}|f\rangle\langle f|\left[D_{\beta z},H\right]|i\rangle\right\} \tag{B.16}$$

Using closure, the sum over final states may be performed.

$$\frac{1}{2}\sum_{\alpha=1}^{A}\sum_{\beta=1}^{A}\left\{\langle i|\left[D_{\alpha z},H\right]D_{\beta z}|i\rangle - \langle i|D_{\alpha z}\left[D_{\beta z},H\right]|i\rangle\right\} \tag{B.17}$$

The commutator $[D_{\alpha z},H]$ may be evaluated as follows,

$$\left[D_{\alpha z},H\right] = e_\alpha\left[z_\alpha,T\right] + \left[D_{\alpha z},V\right] \tag{B.18}$$

Using $[z, p_z] = i$ this becomes,

$$[D_{\alpha z}, H] = ie_\alpha \frac{p_{\alpha z}}{M} + [D_{\alpha z}, V] \tag{B.19}$$

Expression B.17 now becomes,

$$\frac{i}{2M} \sum_f \sum_{\alpha=1}^{A} \sum_{\beta=1}^{A} \{\langle i | e_\alpha p_{\alpha z} D_{\beta z} - e_\beta D_{\alpha z} p_{\beta z} | i \rangle\} + \frac{1}{2} \langle i | \left[[D_z, V], D_z \right] | i \rangle \tag{B.20}$$

The cross terms $\alpha \neq \beta$ vanish and, again using $[z, p_z] = i$ the terms $\alpha = \beta$ yield,

$$\frac{i}{2M} \sum_{\alpha=1}^{A} e_\alpha^2 = \frac{e^2}{2M} \left[Z \frac{N^2}{A^2} + N \frac{Z^2}{A^2} \right] = \frac{e^2}{2M} \frac{ZN}{A} \tag{B.21}$$

The sum rule may now be written in the form:

$$\int_0^\infty \sigma_{E1}(E_\gamma) dE_\gamma = \frac{2\pi^2 e^2}{M} \frac{NZ}{A} (1 + \kappa) = 60 \frac{NZ}{A} (1 + \kappa) \quad \text{[MeV mb]} \tag{B.22}$$

where

$$\kappa = \frac{AM}{NZe^2} \langle i | \left[[D_z, V], D_z \right] | i \rangle \tag{B.23}$$

is an integral measure of the exchange and momentum dependent parts of the nuclear force (which do not commute with D_z). Since the operator is proportional to $r^2 V_{exc}$, the long range pion-exchange terms provide the dominant contribution to κ. Caution is required when comparing this result with experiment since the measured cross-section is integrated over a finite range of energies and contains contributions from other multipoles. However, it is true that σ is dominated at low energies by $E1$ transitions and, in the case of the deuteron, decreases rapidly with energy up to $\sim$ 150 MeV . Therefore it is instructive to compare the measured cross-section integrated up to the pion threshold $\int^{m_\pi} \sigma_{exp,D_2}$ with that calculated using the normal one-body charge density and a realistic N-N potential, $\int^{m_\pi} \sigma_{th,D_2}$. The comparison is shown below in units of the classical sum rule, (30 MeV mb).[13]

$$\Sigma_{TRK} = 1.52 \quad \int_0^{m_\pi} \sigma_{th}(E_\gamma) dE_\gamma = 1.43 \quad \int_0^{m_\pi} \sigma_{exp}(E_\gamma) dE_\gamma = 1.35 \pm 0.1$$

B.3 Gauge Invariance

All observable electromagnetic quantities may be expressed in terms of the electric and magnetic fields $\vec{E}$ and $\vec{B}$. It follows from Maxwell's equations that there exist scalar and vector potentials $\Phi(\vec{x},t)$ and $\vec{A}(\vec{x},t)$ (which are not observables). However fixing $\vec{E}$ and $\vec{B}$ does not determine the potentials uniquely, since for an arbitrary function $f(\vec{x},t)$ the transformation

$$\Phi \longrightarrow \Phi + \frac{1}{c}\frac{\partial f}{\partial t}, \qquad \vec{A} \longrightarrow \vec{A} - \nabla f \tag{B.24}$$

leaves the fields $\vec{E}$ and $\vec{B}$ unaltered. This transformation is known as a gauge transformation. Invariance under such transformations is a fundamental requirement of any observable (e.g. a matrix element) expressed in terms of potentials. In four dimensional notation the gauge transformation can be written as

$$A^\mu(x) \longrightarrow A^\mu(x) + \partial^\mu f(x) \tag{B.25}$$

It can be demonstrated e.g. [25] that the conservation of electric charge follows from this gauge invariance property of the theory.

For any process involving external photons, the matrix element M is of the form

$$\mathcal{M} = \varepsilon^\mu_{\lambda_1} \varepsilon^\nu_{\lambda_2} \ldots \mathcal{M}_{\mu\nu\ldots} \tag{B.26}$$

If the photon is described by

$$A^\mu(x) = \sqrt{\frac{2\pi}{\omega_\gamma}} \varepsilon^\mu_\lambda e^{\pm ikx} \tag{B.27}$$

then the gauge transformation

$$A^\mu(x) \longrightarrow A^\mu(x) + \partial^\mu f(x) \qquad \text{with } f(x) = F(k)e^{\pm ikx} \tag{B.28}$$

implies

$$\varepsilon^\mu_\lambda e^{\pm ikx} \longrightarrow \left[\varepsilon^\mu_\lambda \pm ik^\mu F(k)\right] e^{\pm ikx} \tag{B.29}$$

Invariance of M under this transformation requires

$$k^\mu_1 ... M_{\mu\nu...} = k^\nu_2 ... M_{\mu\nu...} = \cdots = 0 \tag{B.30}$$

i.e. when any external photon polarization vector is replaced by the corresponding four-momentum the amplitude must vanish. For example, in the case of the free nucleon current $J^\mu = (\rho, \vec{J})$, given in momentum space by

$$\vec{J} = \hat{e}\frac{\vec{p}}{M} + \frac{i\hat{\mu}}{2M}\vec{\sigma} \times \vec{k} + O\left(\frac{1}{m^3}\right) \tag{B.31}$$

and

$$\rho = \hat{e} - \frac{\vec{k}^2}{8M^2}\left[2\hat{\mu} - \hat{e}\right] + S.O. + O\left(\frac{1}{m^3}\right) \tag{B.32}$$

Then the gauge invariance condition (to this order of approximation) is

$$\omega\rho - \vec{k} \cdot \vec{J} = 0 + O\left(\frac{1}{m^3}\right) \tag{B.33}$$

this is satisfied since

$$\omega = \frac{\vec{p'^2} - \vec{p^2}}{2M} = \frac{2\vec{p} \cdot \vec{k} + \vec{k}^2}{2M} \tag{B.34}$$

and $\vec{k}^2 = \omega^2$ is already $O\left(\frac{1}{m^2}\right)$. For a one-photon amplitude such as this, the gauge invariance condition $k_\mu J^\mu$ is equivalent to the current conservation condition $\partial_\mu J^\mu$

Appendix C

Monte Carlo Sampling of Non-Uniform Probability Distributions

Let $P(x)$ be a normalised probability distribution describing the occurrence of x over the range $x_1 \rightarrow x_2$. The number of occurrences, n of the value x are given by

$$dn(x) = P(x)dx \tag{C.1}$$

where normalisation implies that

$$\int dn = \int_{x_1}^{x_2} P(x)dx = 1 \tag{C.2}$$

Values of x can be chosen according to the distribution $P(x)$ using a random number sequence if a variable transformation $x \rightarrow \beta(x)$ can be made such that $P(\beta)$ is uniform in β. It is convenient to chose β such that

$$\int_{x_1}^{x_2} d\beta = 1 \tag{C.3}$$

The distributions of points in x and β are related by

$$P(x) = \frac{dn}{dx} = \frac{dn}{d\beta}\frac{d\beta}{dx} \tag{C.4}$$

integrating this expression one has

$$1 = \int_{x_1}^{x_2} \frac{dn}{d\beta}\, d\beta \tag{C.5}$$

However the distribution in β is uniform, (*i.e.* $\dfrac{dn}{d\beta}$ constant) and one may choose $\dfrac{dn}{d\beta} = 1$ which implies

$$\frac{d\beta}{dx} = \frac{dn}{dx} = P(x) \tag{C.6}$$

and the required transformation is

$$\beta(x') = \int_{x_1}^{x'} P(x)dx \tag{C.7}$$

For this method to be of use it is necessary to be able both to perform this integral and to invert the function $F(x) = P'(x)$.

Appendix D

Liquid Deuterium Target Density Measurements

The normal operating condition of the target is one of dynamic equilibrium. The deuterium cell absorbs heat radiation, causing it to boil, while at the same time deuterium gas continually condenses on the refrigerator cold head and falls into the cell. The effect of the continuous boiling of the liquid is to reduce the effective target density.

A series of measurements were undertaken to determine the effective density of the liquid by measuring the pressure drop in a closed gas system of known mass as a function of the volume of the condensate in the cell. for this purpose the system shown in figure 3.17 was modified to include a low pressure D_2 reservoir of large and known volume in place of the high pressure tank and separate small buffer.

The mass of liquid in the cell can be expressed as the product of the volume in the cell v and its effective density ρ'. At a given point in the filling process the mass of liquid condensed is equal to the total mass of deuterium in the

system less the mass of gas remaining. This can be expressed as follows

$$\rho' v = M_{mol}\left(n - \frac{PV}{RT_R} - \frac{P}{R}\int_P \frac{dv_P}{T} - \frac{P(v).(v_C - v)}{RT_C}\right) \qquad \text{(D.1)}$$

or equivalently

$$\frac{R\rho' v}{M_{mol}} = nR - P(v)\left\{\frac{V}{T_R} + \int_P \frac{dv_P}{T} + \frac{v_C}{T_C}\right\} + \frac{P(v)v}{T_C} \qquad \text{(D.2)}$$

where n is the number of moles of deuterium in the system, V is the total volume of the system, v_C is the volume of the cell, T_R is temperature of the reservoir , T_C is temperature of the cell, R is the universal gas constant, M_{mol} is the molar mass of deuterium and $P(v)$ is the gas pressure in the system. The integral over the variable v_P takes into account the small amount of pipe P where the gas temperature lies between the T_R and T_C.

writing the contents of the bracket in D.2 as

$$\Sigma \equiv \left\{\frac{V}{T_R} + \int_P \frac{dv_P}{T} + \frac{v_C}{T_C}\right\}$$

one may express the total contents n in terms of the empty target conditions

$$nR = P(0)\Sigma \qquad \text{(D.3)}$$

assuming that the temperature distribution in the pipework does not change as the cell fills. Differentiating D.2 one obtains

$$\frac{R\rho'}{M_{mol}} = -\frac{dP}{dv}\left[\Sigma - \frac{v}{T_C}\right] + \frac{P(v)}{T_C} \qquad \text{(D.4)}$$

equation D.3 can be used to eliminate $P(v)$

$$\frac{R\rho'}{M_{mol}} = -\frac{dP}{dv}\left[\Sigma - \frac{v}{T_C}\right] + \frac{1}{T_C}\left[P(0)\Sigma - \frac{R\rho' v}{M_{mol}}\right]\left[\Sigma - \frac{v}{T_C}\right]^{-1} \qquad \text{(D.5)}$$

Taking the value of the gradient at the half full position as the average, S

$$S = -\left(\frac{dP}{dv}\right)_{v=v_C/2} \qquad \text{(D.6)}$$

one obtains

$$\frac{R\rho'}{M_{mol}} = S\left[\Sigma - \frac{v_C}{2T_C}\right] + \frac{1}{T_C}\left[P(0)\Sigma - \frac{R\rho' v_C}{2M_{mol}}\right]\left[\Sigma - \frac{v_C}{2T_C}\right]^{-1} \tag{D.7}$$

which simplifies to

$$\frac{R\rho'}{M_{mol}}\Sigma = S\left[\Sigma - \frac{v_C}{2T_C}\right]^2 + \frac{P(0)\Sigma}{T_C} \tag{D.8}$$

and simplifies further using D.2 with $v = \frac{v_C}{2}$.

$$\frac{R\rho'}{M_{mol}} = S\left[\Sigma - \frac{v_C}{2T_C}\right] + \frac{P(v_C/2)}{T_C} \tag{D.9}$$

The refrigerator and target cell were prepared in the same fashion as for the $D(\gamma, p)$ experiment. Particular care was taken to ensure that the superinsulating foil was wrapped around the cell in the same manner. The filled target was stabilised at the same pressure and temperature as used in normal operation and then emptied and filled repeatedly by adjusting the cold head heater current slightly. The quantity $\frac{dP}{dv}$ was found to be essentially constant (figure D.1). The filling and emptying cycles produced similar slopes but the filling data was more scattered and was displaced to lower pressures for the same apparent cell volume. This is consistent with a situation where liquid continually condenses in droplets on the cold head during filling. In this case the total volume of liquid in the system will fluctuate and will generally be greater than the volume seen in the cell. During the emptying phase no recondensation will occur.The vaporisation will take place smoothly and there will be no liquid in the system other than that remaining in the cell. Two 'target emptying' cycles are shown in figure D.1 .

The quantities observed in the measurement were the gas pressure in the system P and the level x of the deuterium liquid in the cell. The liquid level was measured using a travelling microscope on a vertical movement.

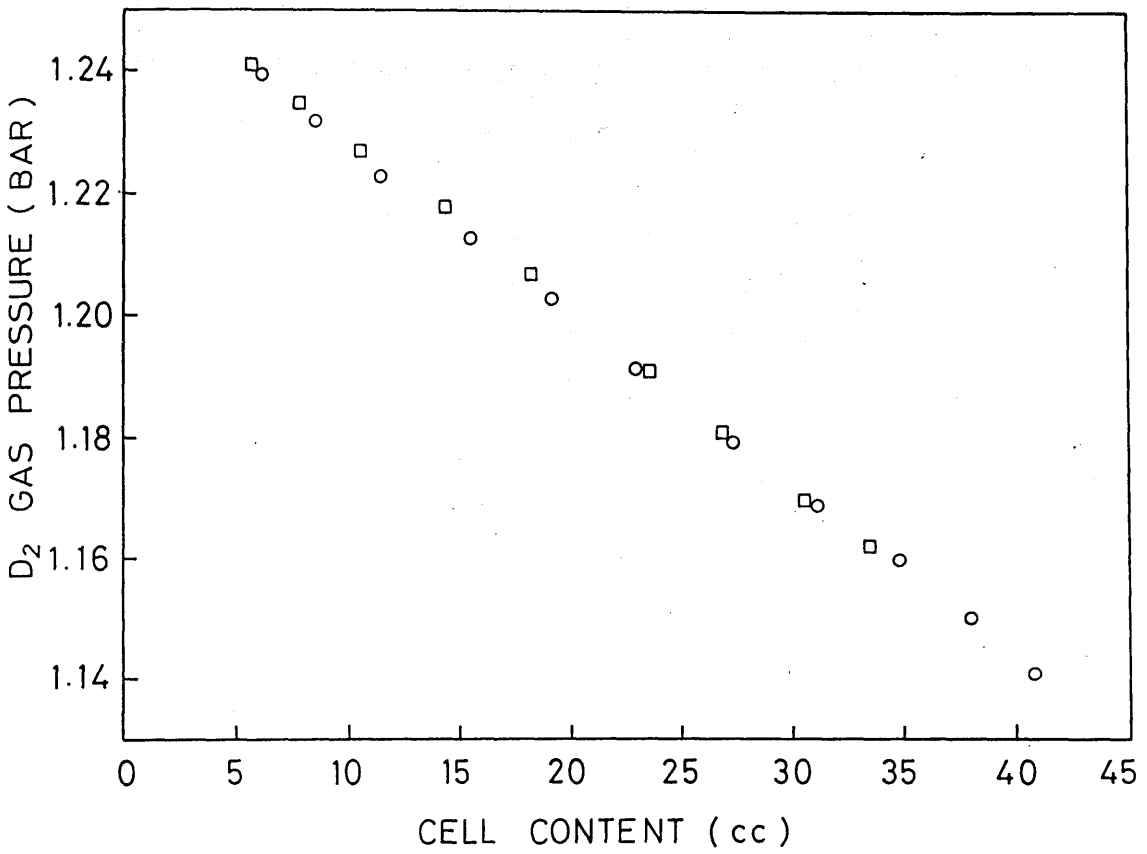

Figure D.1: *Buffer gas pressure vs. cell content. (The circle and square symbols correspond to separate measurements.)*

The cell content v had previously been calibrated in terms of x by observing the level of a series of known amounts of water over a range of cell pressures bracketing the normal operating pressure of the system. It was assumed that the cell windows became rigid at liquid deuterium temperatures and so the shape of the cell remained constant as the cell filled and buffer pressure dropped. However, even in the extreme assumption of normal elasticity the correction was calculated to be be $\sim 2\%$.

The volume of the total system relative to that of the buffer tank alone was determined by observing the pressure drop when the gate valve between the buffer and the gas rig was opened. The ratio of total volume to buffer volume was found to be 1.02. the volume of the buffer tank was measured after the deuterium measurements were taken by filling it with water.

Fitting a straight line to the data of figure D.1 results in a gradient of $(-2.82 \pm 0.03) \times 10^{-3}$ bar.cm^{-3} which is equivalent to $(-2.87 \pm 0.03) \times 10^{-3}$ atmos.cm^{-3}. From equation D.9 the effective density is determined to be

$$\rho' = (0.153 \pm 0.005)\text{g.cm}^{-3}$$

where the following values have been used, $V = (314\ l)$, $R = (8.314$ J mol^{-1} K$^{-1})$, $T_R = 291$ K,$T_C = 22.5$ K and $M_{mol} = 4.02$ g. Given that the nominal density of liquid deuterium is 0.162 g.cm^{-3} then the correction factor ρ'/ρ is 0.942 .

Appendix E

Multiplicity Corrections in the Focal Plane Detector

The six TDCs in which the coincidences between the proton detector and the focal plane detector (FPD) are registered are started by the X-trigger and stopped by the .OR. of a group of 16 focal plane detector channels. At the normally used beam rates there exists a non-negligible probability that more than one electron will register in the group of channels covered by a single TDC. This gives rise to a number of problems in the subsequent data analysis as described in chapter 5. The situation is simplified if the data set is reduced to those events where only one FPD channel has fired in any given TDC group. This removes events where the photon energy and coincidence timing information are ambiguous. Such a selection has the further advantage of producing a random coincidence background in the TDC spectrum which is flat. The disadvantage is that some of the genuine tagged events will have been rejected and a correction must be made when the experimental yield is calculated.

Time Structure of the Random Background in a TDC

Consider a TDC gated for a period $0 \rightarrow \tau$ sec with stop-pulses incoming randomly at a mean rate N $\sec_{-1}$. It is assumed that the random pulse stream is described by a Poisson distribution $\mathcal{P}(n, N\tau)$ where

$$\mathcal{P}(n,m) = \frac{e^{-m}m^n}{n!}$$

is the probability of n pulses arriving in a time period in which the mean number expected is m. The probability $P(t')\delta t$ for a TDC to be stopped in the region $t = t' \rightarrow t' + \delta t$ is the product of the probability that 1 pulse occurs in time δt and the probability that no pulse has arrived in the preceding period $0 \rightarrow t'$.

$$P(t)\delta t = \mathcal{P}(0, Nt).\mathcal{P}(1, N\delta t) \tag{E.1}$$

$$P(t)\delta t = e^{-Nt}e^{-N\delta t}N\delta t \tag{E.2}$$

and in the limit $\delta t \longrightarrow 0$,

$$P(t) = Ne^{-Nt} \tag{E.3}$$

From the above it is seen that the random spectrum in the TDC slopes exponentially and that as the rate N increases the slope becomes steeper. Furthermore, as N increases, the probability for any one pulse to register in the TDC is reduced.

The probability $P(t)$ may be expressed as follows

$$P(t) = \sum_{n=1}^{\infty} P_n(t) \tag{E.4}$$

where $P_n(t)$ is the probability that the TDC stop is caused by the first of n pulses to arrive within the gate period τ. $P_1(t)$ has the simple form,

$$P_1(t)\delta t = \mathcal{P}(0, Nt).\mathcal{P}(1, N\delta t).\mathcal{P}(0, N(\tau - t - \delta t)) \tag{E.5}$$

$$P_1(t)\delta t = e^{-Nt}e^{-N\delta t}N\delta t e^{-N(\tau-t-\delta t)} \tag{E.6}$$

$$P_1(t) = Ne^{-N\tau} \tag{E.7}$$

Therefore P_1 for a fixed $N\tau$ is constant throughout the gate period and, again, as $N\tau$ is increased the probability that a given pulse registers in the TDC decreases.

Correction for Multiple FPD Hit Rejection

One may identify two causes of multiple FPD firings.

The first is due to the geometry of the FPD. A FPD channel consists of two overlapping scintillators whose outputs are fed into a coincidence unit, however the three neighbouring scintillators which correspond to two adjacent channels have an area of common overlap and so it is possible for one electron to pass through three strips and thus trigger two neighbouring channels. In addition to this, δ electrons may be produced and these can cause 3-fold or even 4-fold hits in adjacent channels.

The other source of double, triple...n-tuple hits lie in the probability of several separate electrons arriving in the gate period. This effect is rate dependent as opposed to the geometric effects which are independent of the beam rate. This disappears at very low rates such as are used in taking tagging efficiency data.

At the beam rates used the probabilities of neighbouring n-tuples occurring as a result of several random hits is negligible. The fraction of events which include a random double hit anywhere in the FPD is typically of the order of 20%. Half of these are neighbouring doubles, whereas the fraction of

random doubles which occur in neighbouring channels is $\frac{2}{91}$ (there are 92 FPD channels). In order to analyse the effects of genuine multiple electron hits it is first necessary to correct the multiplicity spectrum for geometric effects. This is done by reassigning all neighbouring multiple hits as singles. Since the sections of the FPD recorded in separate TDCs are analysed separately as independent experiments a genuine tagging electron which fired two channels straddling a TDC boundary would be counted twice. This double counting of neighbouring multiples is avoided by the use of the reassignment algorithm which consistently assigns the event to one channel and therefore one TDC.

The electrons arriving at the FPD may be divided into two classes with different time structures. The random electrons are described by a Poisson distribution, whereas the 'true' tagging electrons come (in principle) at the same time in the coincidence gate. The probability of an n-tuple event consisting of 1 true electron and $(n-1)$ randoms is different from that for an event involving n random electrons. Furthermore the relative probablity of the two processes is rate dependent. The overall count rate of n-tuples is derived below.

Let the electron rate be N and the width of the coincidence gate be τ. The multiplicity of the event is n ($n \geq 1$ since at least one electron is required to trigger the system.)

C_t is the true coincidence rate due to a true X-trigger rate X_t

C_r is the true coincidence rate due to a random X-trigger rate X_r

Each may be expressed as a sum of n-tuple rates.

$$C_t = \sum_{n=1}^{\infty} C_t(n) \qquad C_r = \sum_{n=1}^{\infty} C_r(n) \tag{E.8}$$

The C and X rates are related as follows,

$$C_t = X_t \tag{E.9}$$

$$C_r = X_r \left[\sum_{n=1}^{\infty} P(n, N\tau) \right] = X_r(1 - e^{-N\tau}) \tag{E.10}$$

where $P(n, N\tau)$ is the Poisson distribution defined previously.

The normalised probability of an n-tuple involving a real coincidence electron is

$$P_t(n) = P(n-1, N\tau) \qquad (n \geq 1) \tag{E.11}$$

and that for a purely random n-tuple is given by

$$P_r(n) = \frac{P(n, N\tau)}{\sum_{n=1}^{\infty} P(n, N\tau)} = \frac{P(n, N\tau)}{(1 - e^{-N\tau})} \qquad (n \geq 1) \tag{E.12}$$

The n-tuple rates are expressed in terms of the n-tuple probabilities as follows,

$$C_t(n) = C_t P_t(n) \qquad C_r(n) = C_r P_r(n) \tag{E.13}$$

whence:

$$C(n) = C_t(n) + C_r(n) \tag{E.14}$$

$$C(n) = \frac{e^{-N\tau}(N\tau)^{n-1}}{(n-1)!} \left(X_t + X_r \frac{N\tau}{n} \right) \tag{E.15}$$

It is now possible to calculate the correction factor for data selected on single FPD hits. The count rate corresponding to the final data sample after background subtraction is proportional to $C_t(1)$ whereas the true count rate is proportional to $C_t \equiv \sum_{n=1}^{\infty} C_t(n)$. The correction factor is therefore

$$\frac{C_t(1)}{\sum_{n=1}^{\infty} C_t(n)} = \frac{C_t P(0, N\tau)}{C_t \sum_{n=1}^{\infty} P(n-1, N\tau)} = P(0, N\tau) \tag{E.16}$$

This is intiutively reasonable since $P(0, N\tau) \equiv e^{-N\tau}$ which is the probability that a time gate triggered by a true tagging electron contains 0 random electrons.

There is, in principle, one further correction which must be made before the above result can be compared to experiment. The experimental multiplicity spectrum is determined from the bit pattern stored in a set of pattern units. However the pattern unit channels can only be set once each per event. If two electrons pass through the same FPD channel then the second one is not recorded in the bit pattern. Therefore the correction calculated above is a slight overestimate, since a second electron triggering the channel which has already fired will not cause the event to be rejected as a double hit. If 16 channels are fed into the TDC and if the prompt peak in the time spectrum is situated at time T_0 then the correction becomes

$$e^{-\frac{1}{16}Nt_0}.e^{-\frac{15}{16}N\tau} \tag{E.17}$$

which is equivalent to

$$e^{\left(N\tau-\frac{N}{16}(\tau-t_0)\right)} \tag{E.18}$$

In the present case this effect is very small, being of similar magnitude to the random neighbouring doubles correction which was neglected in the reassignment algorithm. It should be included in the general analysis however since it would be more important in a more fully instrumented system with fewer channels sharing a TDC.

The quantity $N\tau$ may be determined from the data by analysing the multiplicity spectrum obtained from randomly triggered events . Such a sample should be distributed according to the Poisson formula. The random trigger is provided by the LED gain stabilisation system fitted to the proton detector. This requires that an artificial coincidence be made with the FPD in order that the LED pulses are recorded in the ADCs. To this end a synchronised pulse is fed into FPD channel 92, which has no scintillator. This provides the

random trigger with which to gate the TDCs for the present measurement. The Poisson distribution has the following property,

$$\frac{\mathcal{P}(n+1, N\tau)}{\mathcal{P}(n, N\tau)} = \frac{N\tau}{n+1} \tag{E.19}$$

from which the quantity $N\tau$ may be calculated. In practice, only the ratio $\mathcal{P}(1, N\tau)/\mathcal{P}(0, N\tau)$ can be determined from the data with sufficient statistical precision for the determination of the effective gate width. A series of data files with electron beam intensities of $\sim 4 \times 10^6 s^{-1}$ and $\sim 1 \times 10^7 s^{-1}$ were analysed and the result, determined independently from both sets of files, was $\tau = (58 \pm 2)$ns.

Bibliography

[1] J.CHADWICK *and* M.GOLDHABER: Nature **134** (1934) 237

[2] A.BETHE *and* R.PEIERLS: *Proc.Roy.Soc. A* **148** (1935) 146

[3] J.S.LEVINGER *and* H.A.BETHE: *Phys.Rev* **78** (1950) 115

[4] M.GELL-MANN *et.al.* : *Phys.Rev* **96** (1954) 1612

[5] J.V.NOBLE: *Ann.Phys.* **67** (1971) 98

[6] N.F.MOTT: *Proc.Roy.Soc. A* **124** (1929) 425

[7] H.ARENHÖVEL: *Nucl.Phys.* **A374** (1982) 521c

[8] H.ARENHÖVEL: *Nucl.Phys.* **A384** (1982) 287

[9] R.W.BERARD *et.al.* : *Phys.Lett.* **47B** (1973) 355

[10] R.C.BARRETT *and* D.F.JACKSON: 'Nuclear Sizes and Structure', (Clarendon Press, Oxford, 1977)

[11] T.E.O.ERICSON: 'Proc. 5th International School of Intermediate Energy Nuclear Physics',(Verona,1985). (World Scientific Publishing, Singapore) *Ed.* R.Bergere *et.al.*

[12] J.M.LAGET: *Nucl.Phys.* **A312** (1978) 265

[13] H.ARENHÖVEL: 'Nuclear Physics with Electromagnetic Interactions', (Mainz,1979). *Lecture notes in Physics* **108** (Springer-Verlag,Berlin)

[14] R.DE TOURREIL *and* D.W.L.SPRUNG: *Nucl.Phys.* **A201** (1973) 193

[15] M.LACOMBE *et.al.* : *Phys.Rev. C* **21** (1980) 861

[16] T.HAMADA *and* I.D.JOHNSTONE: *Nucl.Phys.* **34** (1962) 382

[17] J.W.HUMBERTSON *and* J.B.G.WALLACE: *Nucl.Phys.* **A141** (1970) 362

[18] J.L.FRIAR *et.al.* : *Phys.Rev. C* **30** (1984) 441

[19] A.CAMBI *et.al.* : *Phys.Rev.Lett.* **48** (1982) 462

[20] A.CAMBI *et.al.* : *J.Phys. G* **10** (1984) L11

[21] W.JAUS *and* W.S.WOOLCOCK: *Nucl.Phys.* **A431** (1987) 669

[22] L.N.PANDEY *et.al.* : *Phys.Rev. C* **32** (1985) 1842

[23] H.ARENHÖVEL: *Z.Phys. A* **302** (1981) 25

[24] R.MACHLEIDT *et.al.* : *Phys.Rep.* **149** (1987) 1

[25] F.MANDL *and* G.SHAW: Quantum field Theory (Wiley 1984)

[26] J.D.BJORKEN *and* S.D. DRELL: Relativistic Quantum Mechanics (McGraw-Hill, New York, 1964)

[27] L.I.SCHIFF: *Phys.Rev* **83** (1951) 252

[28] W.HEITLER: Quantum Theory of Radiation (OUP,London 1944) p.252

[29] A.S.PENFOLD *and* J.E.LEISS: *Phys.Rev* **114** (1959) 1332

[30] J.L.MATHEWS *and* R.O.OWENS: *Nucl.Inst.Meth.* **91** (1971) 37

[31] A.VEYSSIÈRE *et.al.* : *Nucl.Inst.Meth.* **165** (1979) 417

[32] L.CASANO *et.al.* : *Frascati Report* LNF 74/60 (P)

[33] M.BASSETI: *Frascati Report* LNF (Adone)E-12/1974

[34] J.WEIL *and* B.MCDANIEL: *Phys.Rev* **92** (1953) 391

[35] J.O'CONNELL *et.al.* : *Phys.Rev* **126** (1962) 228

[36] T.ARMSTRONG *et.al.* : *Phys.Rev. D* **5** (1972) 1640

[37] J.ARENDS *et.al.* : Bonn Univ. Report (HE-78/19) (1979)

[38] E.A.WHALIN *et.al.* : *Phys.Rev* **101** (1956) 377

[39] J.C.KECK *and* A.V.TOLLESTRUP: *Phys.Rev* **101** (1956) 360

[40] V.A.ALEKSANDROV *et.al.* : *Soviet Physics JETP* **6** (1958) 472

[41] R.KOSE *et.al.* : *Z.Phys* **202** (1967) 365

[42] J.BUON *et.al.* : *Phys.Lett.* **26B** (1968) 595

[43] R.J.HUGHES *et.al.* : *Nucl.Phys.* **A267** (1976) 329

[44] K.H.ALTHOFF *et.al.* : *Z.Phys.C* **21** (1983) 149

[45] P.DOUGAN *et.al.* : *Z.Phys. A* **280** (1977) 341

[46] E.DESANCTIS *et.al.* : *Phys.Rev. C* **34** (1986) 413

[47] J.M.CAMERON *et.al.* : *Nucl.Phys.* **A458** (1986) 637

[48] J.KELLIE *et.al.* : *Nucl.Inst.Meth.* **A241** (1985) 153

[49] H.HERMINGHAUS *et.al.* : *Nucl.Inst.Meth.* **138** (1976) 1

[50] H.HERMINGHAUS *et.al.* : *Nucl.Inst.Meth.* **187** (1981) 103

[51] M.P.DEPASCALE *et.al.* : *Phys.Lett.* **119B** (1982) 30

[52] S.CIERJACKS *et.al.* : *Nucl.Inst.Meth.* **A238** (1985) 354

[53] D.EVERS *et.al.* : *Nucl.Inst.Meth.* **124** (1975) 23

[54] E.HOURANI *et.al.* : *Nucl.Inst.Meth.* **134** (1976) 513

[55] P.NETTER *et.al.* : *Nucl.Inst.Meth.* **185** (1981) 165

[56] J.S.PRUITT *and* S.R.DOMEN: NBS Monograph 48 (1962)

[57] E.R.KINNEY *et.al.* : *Nucl.Inst.Meth.* **185** (1981) 189

[58] J.L.HUBBELL: *J.App.Phys.* **7** (1959) 981

[59] V.L.HIGHLAND: *Nucl.Inst.Meth.* **161** (1979) 171

[60] Y.S.TSAI: *Rev.Mod.Phys* **46** (1974) 815

[61] W.H.BARKAS *and* M.J.BERGER: 'Tables of Energy Losses and Ranges of Heavy Charged Particles', NASA SP-3013 (1964)

[62] D.F.MEASDAY *and* C.RICHARD-SERRE: Cern Internal Report CERN 69-17 (1969)

[63] J.B.BIRKS *and* F.A.BLACK: *Proc.Roy.Soc.* **A64** (1951) 511

[64] T.J.GOODING *and* H.G.PUGH: *Nucl.Inst.Meth.* **7** (1960) 189

[65] J.R.M.ANNAND: private communication

[66] S.N.DANCER: private communication

[67] I.ANTHONY: private communication

[68] J.M.LAGET: *Can.J.Phys.* **62** (1984) 1046 and private communication

[69] B.MOSCONI : private communication

[70] H.ARENHÖVEL: private communication

[71] S.YING *et.al.* : *Phys.Rev. C* **38** (1988) 1584

[72] W.LEIDEMANN *and* H.ARENHÖVEL : *Z.Phys. A* **326** (1987) 333

[73] J.AHRENS: private communication